

The Pennsylvania State University  
The Graduate School

**COMPUTATIONAL INVESTIGATION OF SONGBIRD HVC  
MICROCIRCUIT FOR PRECISE TIMING**

A Dissertation in  
Physics  
by  
Yevhen Tupikov

© 2019 Yevhen Tupikov

Submitted in Partial Fulfillment  
of the Requirements  
for the Degree of

Doctor of Philosophy

December 2019

The dissertation of Yevhen Tupikov was reviewed and approved\* by the following:

Dezhe Z. Jin  
Associate Professor of Physics  
Dissertation Advisor  
Chair of Committee

Réka Albert  
Distinguished Professor of Physics and Biology

Vincent H. Crespi  
Distinguished Professor of Physics, Materials Science and Engineering, and Chemistry

Carina Curto  
Professor of Mathematics

Nitin Samarth  
Professor of Physics  
George A. and Margaret M. Downsborough Department Head

\*Signatures are on file in the Graduate School.

# Abstract

Learned sequential behaviors are fascinating brain phenomena, but their underlying neural mechanisms are not well understood. Birdsong is a great model to investigate such behavior, since it is stereotyped and is learned gradually by juvenile songbirds from their tutors. Songbird premotor nucleus HVC (proper name) produces precise bursts of projection neurons during singing and is thought to encode timing in the song. We develop a detailed computational model of zebra finch HVC neural microcircuit, which incorporates all experimentally known features of HVC, including realistic number of neurons, connectivity patterns and axonal conduction delays. We show that a popular model for songbird HVC, a synfire chain, produces strong oscillations in neural dynamics, which is inconsistent with experimental observations. We propose an alternative model, a polychronous network, in which all inputs arrive synchronously to postsynaptic neurons. The proposed network naturally exploits distributed axonal conduction delays and produces neural activity with no significant oscillations and silent gaps, i.e., smooth dynamics. We further explore the role of axonal conduction delays in polychronous network and demonstrate that width of the axonal delay distribution controls the oscillations in network dynamics. Narrow distributions produce networks with prominent oscillations, while wide distributions result in networks with smooth dynamics. The results suggest that distributed axonal delays alone can explain the smoothness of HVC dynamics. Next we develop a biologically realistic model that explains the formation of microcircuit for precise timing in HVC. The model is built on the idea that immature neurons, provided by neurogenesis in HVC during development, are more spontaneously active and become prime targets of self-organizing process via synaptic plasticity. The model predicts that birth order of neurons positively correlates with their burst timing in the formed network. We show that with incorporation of realistic axonal conduction delays, our model produces long polychronous sequences. In contrast, ignoring delays leads to the emergence of synfire chains. The model also reproduces the experimentally observed spatial connectivity profile between projection neurons in HVC. Finally, the model predicts that inhibition plays an important role during formation of HVC microcircuit. Neurons that receive less inhibition are more likely to get incorporated into the network.

# Table of Contents

List of Figures	vii
List of Tables	xi
Acknowledgments	xii
<b>Chapter 1</b>	
<b>Introduction</b>	<b>1</b>
1.1 Songbird as a model for song production, learning and neurogenesis . . .	2
1.1.1 Songbird brain . . . . .	3
1.1.2 Song development in zebra finches . . . . .	4
1.1.3 Neurogenesis in HVC . . . . .	5
1.1.4 Song related neuron activity of premotor nuclei . . . . .	6
1.2 Neural networks for encoding time sequences . . . . .	8
1.2.1 Synfire chain . . . . .	9
1.2.2 Polychronous network . . . . .	11
1.3 Outline . . . . .	12
<b>Chapter 2</b>	
<b>Computational models</b>	<b>13</b>
2.1 HVC-RA neuron model . . . . .	14
2.2 HVC-I neuron model . . . . .	17
2.3 Synaptic model . . . . .	19
2.4 Noise model . . . . .	20
2.5 Simulation of neuron dynamics . . . . .	21
2.5.1 Simulation of HVC-RA neuron model . . . . .	21
2.5.2 Simulation of HVC-I neuron model . . . . .	24
2.6 Simulation of network dynamics . . . . .	24
2.7 Conclusions . . . . .	26
<b>Chapter 3</b>	
<b>Modeling HVC microcircuit</b>	<b>27</b>
3.1 Neuronal spatial arrangement . . . . .	28
3.2 Neuronal connectivity . . . . .	29

3.3	Axonal conduction delays . . . . .	31
3.4	Neuron model and simulations . . . . .	33
3.5	Pruned synfire chain . . . . .	33
3.5.1	Pruned chain construction . . . . .	33
3.5.2	Burst onset density oscillations in pruned chain . . . . .	37
3.5.3	Late inputs in pruned chain . . . . .	40
3.5.4	Membrane potential rise time . . . . .	42
3.6	Parallel pruned synfire chains . . . . .	43
3.7	Polychronous network . . . . .	46
3.7.1	Mechanistic wiring algorithm . . . . .	46
3.7.2	Polychronous network with satisfied HVC constrains . . . . .	49
3.7.3	Investigation of polychronous networks . . . . .	52
3.7.4	Polychronous network with uniform delay distribution . . . . .	56
3.7.5	Randomly rewired polychronous network . . . . .	57
3.8	Alternative ways to achieve smooth neural activity . . . . .	58
3.8.1	Random network . . . . .	58
3.8.2	Synfire chain with strong noise . . . . .	61
3.8.3	Synfire chain with distributed neuronal integration times . . . . .	62
3.8.4	Polychronous network with distributed neuronal integration times . . . . .	64
3.9	Conclusions . . . . .	67

## Chapter 4

	<b>Sequence development in HVC</b>	<b>68</b>
4.1	Re-analysis of spike patterns of HVC projection neurons in juvenile zebra finches . . . . .	69
4.1.1	Data set exploration . . . . .	71
4.1.2	Interspike intervals . . . . .	72
4.1.3	Burst tightness . . . . .	72
4.1.4	Syllable locking . . . . .	73
4.1.5	Spike width . . . . .	75
4.1.6	HVC-X neurons . . . . .	76
4.1.7	Spike patterns during and outside song bouts . . . . .	78
4.1.8	Conclusions . . . . .	79
4.2	Computational model for sequence formation . . . . .	79
4.2.1	Neuronal spatial arrangement . . . . .	80
4.2.2	Neuronal connectivity . . . . .	81
4.2.3	Neuron model . . . . .	82
4.2.4	Maturation dynamics . . . . .	85
4.2.5	Neuronal turnover . . . . .	87
4.2.6	Synaptic plasticity rules . . . . .	88
4.2.7	Network growth . . . . .	90
4.2.8	Axonal conduction velocity and network topology . . . . .	91
4.2.9	The role of inhibition in network growth . . . . .	94
4.2.10	Role of immature neurons . . . . .	98

4.2.11 Resilience to changes in model parameters . . . . .	99
4.2.12 Spatio-temporal activity pattern . . . . .	100
4.2.13 Sequence splitting . . . . .	100
4.2.14 Depolarizing GABA during development . . . . .	102
4.2.15 Conclusions . . . . .	106

<b>Bibliography</b>	<b>107</b>
---------------------	------------

# List of Figures

1.1	Song structure . . . . .	2
1.2	Avian brain nuclei associated with song production and learning . . . . .	3
1.3	Neurogenesis rate correlates with learning . . . . .	6
1.4	Neuron activity in pre-motor nucleus HVC of adult zebra finch . . . . .	7
1.5	Single synfire chain and branching chain network . . . . .	10
1.6	Significance of axonal conduction delays . . . . .	11
2.1	Computational model of HVC-RA neuron . . . . .	15
2.2	Computational model of HVC-I neuron . . . . .	17
2.3	Membrane potential fluctuations of HVC-I and HVC-RA neurons . . . . .	20
2.4	Comparison of numerical methods for simulating neuron dynamics . . . . .	22
2.5	Scaling of network dynamics simulation time with number of MPI processes . . . . .	25
3.1	Neuronal spatial arrangement and dendritic tree . . . . .	28
3.2	Connections between HVC-RA and HVC-I neurons . . . . .	29
3.3	Axonal conduction delays between HVC-RA and HVC-I neurons . . . . .	32
3.4	Comparison of synfire chain before and after pruning . . . . .	35
3.5	Comparison of edge and center neurons. . . . .	36

3.6	Dynamics of pruned synfire chain . . . . .	38
3.7	Precision in pruned synfire chain . . . . .	40
3.8	Late inputs in pruned synfire chain . . . . .	41
3.9	Membrane potential rise time . . . . .	42
3.10	Parallel pruned synfire chains . . . . .	44
3.11	Mechanistic algorithm for wiring a polychronous network . . . . .	47
3.12	Behavior of the wiring algorithm . . . . .	49
3.13	Polychronous network embedded in space . . . . .	51
3.14	Polychronous networks with different axonal conduction velocity . . . . .	54
3.15	Two parallel chains with spread starter neurons . . . . .	55
3.16	Polychronous network with different parameters of log-normal axonal conduction delay distribution . . . . .	56
3.17	Polychronous network with uniform axonal delay distribution . . . . .	57
3.18	Randomly rewired polychronous network . . . . .	58
3.19	Random network . . . . .	59
3.20	Synfire chain with large noise . . . . .	60
3.21	Integration time and noise with distributed membrane time constant . . .	62
3.22	Synfire chain with distributed membrane time constants. . . . .	63
3.23	Polychronous network with distributed integration times . . . . .	65
4.1	Two spike shapes of projection neurons . . . . .	70
4.2	Missed spikes . . . . .	70
4.3	Distributions of interspike intervals . . . . .	71

4.4	First interspike interval . . . . .	72
4.5	Maturation of spike properties of HVC-RA neurons . . . . .	73
4.6	Syllable locking . . . . .	74
4.7	Burst tightness and latency of HVC-RA neurons at different stages of vocal development . . . . .	75
4.8	Spike width of HVC-RA neurons . . . . .	76
4.9	Maturation of spike properties of HVC-X neurons . . . . .	77
4.10	Burst tightness and latency of HVC-X neurons at different stages of vocal development . . . . .	77
4.11	Spike width of HVC-X neurons . . . . .	78
4.12	Burst tightness comparison for HVC-X neurons . . . . .	79
4.13	Subsong HVC-RA neuron with tight burst . . . . .	80
4.14	Spatial arrangement and connectivity . . . . .	81
4.15	Maturation model with and without low-threshold potassium current . . . . .	83
4.16	Maturation model with adjusted leak membrane conductance . . . . .	85
4.17	Maturation model with different strength of low-threshold potassium current . . . . .	86
4.18	Spontaneous firing rate . . . . .	87
4.19	Maturation model . . . . .	87
4.20	Mechanism of network growth. . . . .	89
4.21	Example of two grown networks with different axonal conduction velocity. . . . .	92
4.22	Conduction velocity shapes network topology. . . . .	93
4.23	Mechanism of pruning long delay connections . . . . .	94
4.24	The role of inhibition in network growth . . . . .	95

4.25	The role of inhibition in network growth (Continued) . . . . .	96
4.26	Analysis of inhibitory conductance traces in grown network . . . . .	98
4.27	Loop formation in the network with noisy mature HVC-RA neurons . . .	98
4.28	Network with weak synaptic connections . . . . .	99
4.29	Spatio-temporal activity pattern of HVC-RA neurons . . . . .	101
4.30	Network growth with large training set . . . . .	102
4.31	GABA response of immature and mature HVC-RA neurons . . . . .	102
4.32	Recruitment is guided by inhibition . . . . .	103
4.33	Large inhibition destroys the sequence . . . . .	104
4.34	Moderate inhibition results in emergence of a loop. . . . .	104
4.35	Spatio-temporal activity pattern of HVC-RA neurons with depolarizing GABA . . . . .	105

# List of Tables

2.1	Parameters of HVC-RA neuron model . . . . .	16
2.2	Parameters of HVC-I neuron model . . . . .	18
2.3	Synaptic parameters of neuron models . . . . .	19

# Acknowledgments

I would like to thank all people that made my graduate school experience productive and enjoyable. First, I would like to thank my supervisor, Dezhe Jin, for his immense support, encouragement and creativity without which this dissertation would not have been possible. My deep gratitude to our experimental collaborators, Robert Egger, Michael Long and other members of the Long Group, for sharing data, ideas and providing constructive feedback. I would also like to thank Professor Jia Li and Professor Lynn Lin from Statistics department for the invaluable opportunity to work with them during Summer 2018. Many thanks to my friends and colleagues, Leo Tavares, Jiali Lu, Sumithra Surendralal, Autumn Zender, Alex Kunin, Fatemeh Bahari, Anirban Das, Bugra Ayan, Sudip Ghosh and many many more, for fun, discussions and support. Finally, special thanks to my wife Olga, for her patience and understanding throughout these years.

# Chapter 1 | Introduction

Complex and precise sequential behavior patterns are ubiquitously observed in animals. Activities such as playing a musical instrument, performing dance moves and making a tennis serve are some examples of sequential human behaviors that require an impressive accurate muscle coordination and memory. While these behaviors are driven by the activity of neuronal circuits in the brain, the exact organization of these circuits remains largely unknown. In particular, the connectivity patterns between neurons (i.e., network topology) responsible for the observed behaviors are not well understood and are an active area of research in neuroscience.

In addition, an ability to produce the above mentioned activities is not innate. It is gained through a rather complex trial-and-error learning process. At the start of learning, there is a highly variable repertoire of movements with a poor outcome. Gradually, the produced behavior becomes more accurate, which is accompanied by more stereotyped movements. How the process of learning happens remains poorly understood [1–3]. Better understanding of neuronal mechanisms behind learning may help us to improve the learning experience and may potentially lead to the creation of self-learning artificial intelligence agents.

Unfortunately, neuronal mechanisms are hard to investigate in humans, since the most accurate recording techniques are invasive and dangerous for subjects. Animals also demonstrate a rich repertoire of learned sequential behaviors and are easier to study. Therefore, animal models of sequential behavior can provide highly relevant insights into the corresponding mechanisms used by human brain.

One prominent example of the precise temporal activity observed in animals is singing. Singing is a complex vocalization usually used for mating and territory protection. Only a small number of animal species produce songs including humpback whales [4, 5], mice [6], bats [7] and songbirds [8].

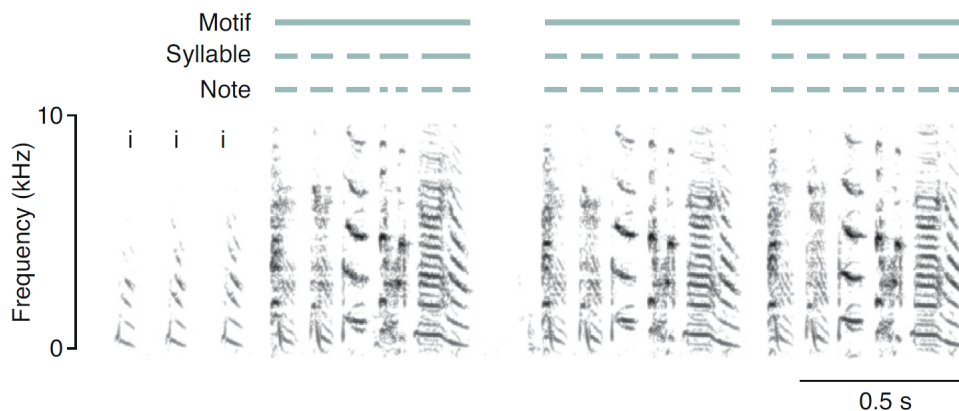


**Figure 1.1.** Song structure. An example of a sound spectrogram of a zebra finch song. Typically, a song is preceded by one or several introductory notes (i). Sequences of syllables, that are continuous sounds separated by brief intervals of silence, form motifs. One or several motifs are usually produced per song rendition. Reprinted from [9] with permission from Elsevier

In this dissertation, we use computational modeling to explore the neural circuit responsible for song production in songbirds. We also investigate how this circuit emerges during learning and development, when there is an intensive addition of new neurons (i.e., neurogenesis) to the song related nuclei. The remainder of this introductory chapter provides an overview of songbirds as a model for song production, learning and neurogenesis; and introduces synfire chain and polychronous models of feedforward neural networks producing precise temporal sequences.

## 1.1 Songbird as a model for song production, learning and neurogenesis

Songbirds are similar to humans in many aspects of their behavior and brain organization. Some avian species, like canary and zebra finch, have been domesticated and are easy to handle and breed in captivity. Therefore, songbirds became one of the most well-studied systems in neuroscience. One of the intriguing and relatively easy to study behaviors of songbirds is vocalization. The vocalization of songbirds can be readily recorded, analyzed and quantified.

Songs are acoustically complex vocalizations that emerge in juvenile birds trying to mimic the song of their tutors. They are usually used by males for proclaiming vigor and dominance, and advertisement of sexual availability. Below we will introduce some

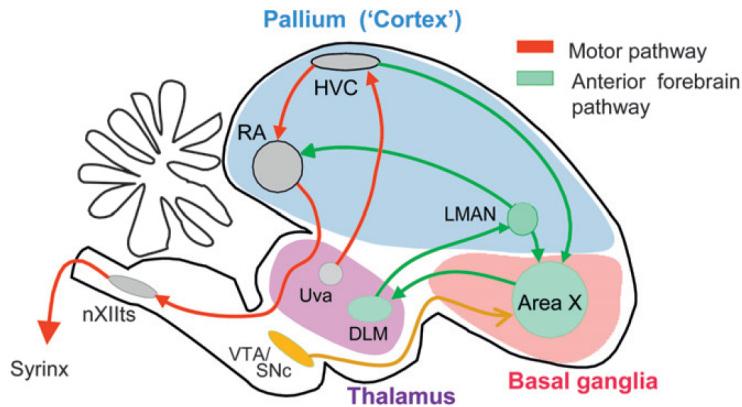


**Figure 1.2.** Avian brain nuclei associated with song production and learning. Nucleus uvaeformis (Uva), HVC (proper name), robust nucleus of arcopallium (RA) and nucleus of the twelfth nerve (nXIIIts) form a motor pathway, which is responsible for the song production. Medial portion of the dorsolateral thalamus (DLM), lateral magnocellular nucleus of the anterior nidopallium (LMAN) and Area X are parts of the anterior forebrain pathway, needed for song learning. Reprinted from [11] with permission from Oxford University Press

terminology commonly used among songbird researchers. The simplest individual sounds produced by songbirds are called *notes*. A series of one or more notes, which is separated by brief silent intervals, is referred to as a *syllable*. A sequence of one or more syllables is called a *motif*. In many songbirds, the order of the syllables in the motifs corresponding to the same song does not change from one song rendition to another. The ordering of syllables in a given song is referred to as a song *syntax*. The syntax of many songbird species is complex allowing transitions between multiple syllable types. Fig. 1.1 illustrates the song structure terminology using an example of a zebra finch song.

Juvenile songbirds typically do not sing. They acquire an ability to sing through listening to their tutors and attempting to repeat the sounds heard. In the next section, we will describe the songbird brain circuitry responsible for song production and learning.

### 1.1.1 Songbird brain

Songbirds have developed sophisticated brain structure to allow for a song production and learning (see Fig. 1.2). Brain nuclei and major neural pathways related to song control have been identified in the past [10].

Song related neural circuitry can be roughly divided into two parts. The first part, called the motor pathway, is responsible for the song production. The output of the motor pathway feeds directly into the muscles controlling the songbird vocal

organ syrinx through the tracheosyringeal portion of the nucleus of the twelfth nerve, nXIIIts [12,13]. Motor neurons in nXIIIts receive their main input from the robust nucleus of the arcopallium (RA), structure analogous to the mammalian layer V motor cortex [14]. Nucleus RA also projects to brainstem motor centers regulating respiration, therefore providing coordination between vocalization and breathing. RA receives the input from the caudal nidopallium nucleus HVC (proper name), which in turn is innervated by the thalamic nucleus uvaeformis (Uva) [15] and the nucleus interfascialis (Nif, not shown). HVC is also considered analogous to the mammalian motor cortex and is the main focus of this dissertation. Lesions in the motor pathway disrupt singing or strongly decrease its quality [16], showing that motor pathway is essential for the successful song production.

The second part of song related neural circuitry is called anterior forebrain pathway (AFP). AFP forms a loop of interconnected nuclei, that feeds back to RA, thus affecting the song production. Area X, which is homologous to basal ganglia [17], receives the input from HVC and projects to the medial nucleus of the dorsolateral thalamus (DLM). DLM in turn is connected to the lateral magnocellular nucleus of the anterior nidopallium (LMAN). LMAN completes the loop by sending connections to Area X and at the same time projects to motor nucleus RA. The importance of AFP for song learning was thoroughly investigated in lesion studies [18–20]. Almost no effect on the song is produced by lesions in any AFP nucleus in adult birds. In other words, AFP is not needed for song production after the song learning stage is over. However, lesions of AFP in juvenile birds lead to a drastic decrease in their ability to mimic the tutor’s song. Lesions of LMAN in young birds decrease the observed song variability. Both the syllable structure and the song syntax stabilize and are often more simplified compared to the pre-lesion songs. Lesions of Area X prevent the song from crystallization. The song remains highly variable and fails to develop the stereotypy of the songs of normally raised birds.

### **1.1.2 Song development in zebra finches**

In this dissertation, we will mostly focus on investigating one particular bird species - zebra finches. Zebra finches are closed-ended learners, which means that they have a limited period of sensitivity to vocal experience, called a *critical period*. They typically learn to sing a single song during their life. Zebra finches are opportunistic breeders and do not experience seasonal changes in song control brain circuitry. Therefore, zebra finch is one of the simplest available models to study song learning.

Song learning starts with juvenile zebra finches listening to and memorizing the

song of their adult tutors, typically their fathers. By the age between 28 and 35 days, juveniles begin to produce soft sounds, trying to mimic the memorized song template [21]. Gradually, soft sounds become louder and at the age of about 40 days, juveniles enter the subsong stage of their vocal development [21]. In the subsong stage, the produced song has a highly variable structure and is akin to human babbling [22]. Syllable durations are random and follow an exponential distribution [23, 24]. Between 50 to 60 days, referred to as a protosyllable stage, the birds start to incorporate syllables of a characteristic duration  $\sim 100$  ms [25, 26]. It is then followed by a multi-syllable stage, with multiple syllables showing distinctive acoustic features [27]. Finally, by the age of  $\sim 70$  days, juveniles enter the "motif" stage with syllables produced in a reliable sequence [28]. By 90 days of age, the song acquires stereotyped structure and remains almost unchanged afterwards [28].

If juvenile zebra finches are raised in isolation from tutors, they develop a distinct, *isolate* song, which can easily be distinguished from the songs of normally raised birds. Surprisingly, the song of the colonies founded by isolates gradually converges to a wild-type song in 3-4 generations [29]. Therefore, the zebra finch song develops as a combination of social interactions and genetic innate factors.

### 1.1.3 Neurogenesis in HVC

While HVC is not needed for subsong production, which is driven by neurons in LMAN [30], it is required at all later stages of song development. HVC contains three main types of neurons: excitatory RA-projecting neurons (HVC-RA), excitatory Area X projecting neurons (HVC-X), and inhibitory interneurons that do not project outside HVC (HVC-I). Majority of HVC-RA neurons are added to HVC after hatch [31–34]. The number of HVC-RA neurons of zebra finches almost doubles between 20 and 50 days post-hatch [35]. Thus, vocal development is accompanied by an intensive addition of new RA-projecting neurons to HVC (see Fig. 1.3). When zebra finches develop a stable, crystallized song, neurogenesis rate sharply decreases.

New neurons are constantly added to HVC of zebra finches throughout the bird's life [37]. The adult-born neurons in canaries develop similar morphology to the existing HVC-RA neurons and get fully incorporated into song control circuits [38, 39]. The functions of adult-born HVC-RA neurons might be different from the post-hatch-born HVC-RA and are not well understood. One popular idea is that adult born neurons participate in song maintenance and replace mature neurons that die due to over-excitation and/or DNA-damage [40–42].

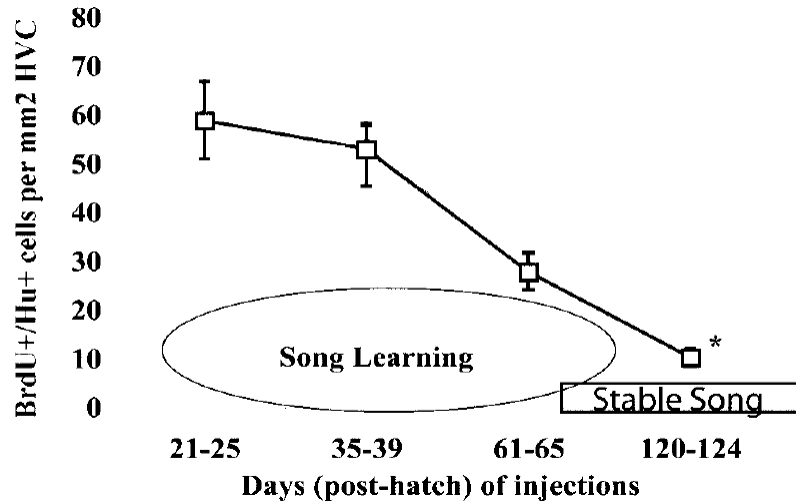


**Figure 1.3.** Neurogenesis rate correlates with learning. Number of newly generated neurons versus bird's age for zebra finch. Neurogenesis rate sharply decreases after song crystallization. Adapted from [36] with permission from JNeurosci. Copyright 2002 Society for Neuroscience.

Proliferative cells that produce new neurons are located in "hotspots" in the walls of the lateral ventricle of the songbird brain [39, 43, 44]. Neurogenesis timeline was revealed through studies of adult-born neurons in canaries. After 1 to 4 days, newly formed neuroblasts start to migrate from the place of birth [45, 46]. Migration of new HVC neurons takes about 1-2 weeks and is either guided by radial glia or shows more random wandering pattern [45, 47]. At the end of the migration, new neurons form cell clusters by making somatal contact with mature HVC interneurons and HVC-X projection neurons [47, 48]. It was hypothesized that the contact with mature HVC-X neurons provides "training" for newly added cells and facilitates their functional incorporation into existing circuits. Most of the new HVC neurons start to make synapses on RA neurons by 2 weeks of age and by the age of 8 months have traceable targets in RA [48].

### 1.1.4 Song related neuron activity of premotor nuclei

We start by describing neurons in the pre-motor nucleus HVC. Inside HVC, HVC-RA neurons send sparse and distal connections to other HVC-RA and HVC-X neurons, and make local connections to interneurons [50, 51]. HVC-X neurons also connect to interneurons, but connections to other HVC-X or HVC-RA are not common. Interneurons project to both HVC-RA and HVC-X neurons, but little is known about the spatial profile of these connections. The study performing systematic ablation of HVC-X neurons in adult zebra finches [52] showed no decrease in song quality even for near complete

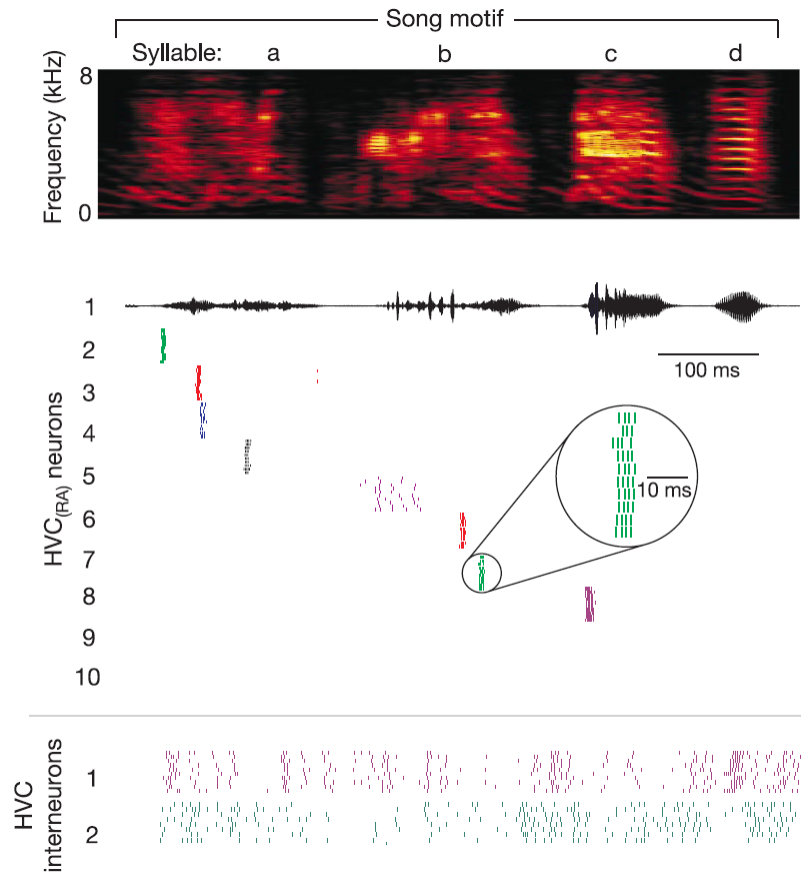


**Figure 1.4.** Neuron activity in pre-motor nucleus HVC of adult zebra finch. Top: spectrogram of a song motif. Middle: song-aligned activity of RA projecting neurons in HVC. Bottom: song-aligned activity of inhibitory interneurons in HVC. Reprinted from [49] with permission from Springer Nature.

death of HVC-X neurons. Taken together with the lack of HVC-X projections to other excitatory neuron populations in HVC, it suggests that activity of HVC-X neurons is not important for the song production.

In the influential study [49], the authors have recorded a single unit activity of neurons in pre-motor nucleus HVC of singing zebra finches (see Fig. 1.4). HVC-RA neurons demonstrated a very sparse activity, usually producing a single burst of 4-5 spikes per song motif. When aligned to different renditions of the song-bouts, activity of HVC-RA neurons was extremely precise, showing a sub-millisecond jitter in burst onset times. Such precision was unprecedented in neuroscience at that time, since researchers were familiar with irregular, almost chaotic activity of cortical neurons. Contrary to the sparse activity of HVC-RA neurons, inhibitory interneurons spiked frequently during the song. Their activity was less stereotypical, but still showed significant correlations of firing rate

across song renditions.

Recordings in the pre-motor nucleus RA show that individual RA neurons produce a series of high frequency bursts [53]. On average, RA neurons produce around 12 bursts per song motif with an average duration of 10 ms [54]. The burst shapes and location in the song are highly repeatable across the song renditions, resembling the accuracy of projection neurons in HVC [54, 55].

Due to the high precision and sparse activity, HVC-RA neurons were hypothesized to encode the timing in a bird song. According to this idea, bursts of synchronously spiking neurons serve as a biological clock tick, which transmits the information of *what* to do and *when* to a downstream nucleus RA [54]. In this case, neurons in RA serve as individual "piano keys", "pressed" by the neurons in HVC. Since RA neurons can receive connections from different neurons in HVC, they can be "pressed" at multiple time instances during the song. High precision of HVC neurons ensures that RA neurons also produce repeatable burst shapes.

## 1.2 Neural networks for encoding time sequences

Many competing theories exist that describe possible networks producing the observed activity of HVC-RA neurons. In fact, any network that is able to generate time sequences should be considered as a possible candidate. In this section, we will briefly review the popular networks used for modeling time sequences and point out the networks compatible with observed activity of HVC-RA neurons.

Sequence encoding networks can be roughly split into two categories. Generic networks start with connectivity not tuned for sequence generation. It is then adapted through learning algorithms to achieve a task-specific goal. Usually, generic network approach starts with a random interconnected network with both excitatory and inhibitory connections. Connection strengths are chosen to keep the network in so called *balanced* state, in which inhibition and excitation balance each other. The balanced network state produces irregular chaotic activity of the neurons, which is thought to be present in cortical neurons [56–58].

Several learning algorithms exist that are able to modify the synaptic weights in balanced recurrent networks to achieve the desired output and/or network activity [59–61]. Sequences as long as 5s were successfully produced by recurrent networks with tuned connections [60, 62]. However, tunable recurrent network approaches use limited firing rate neuron models, and to our knowledge there is no successful implementation of a

recurrent network based on spiking neurons. Moreover, no model was previously reported to generate sequences with sub-millisecond temporal precision of individual neurons, which is the precision observed in the real songbird HVC. Taken together, approaches based on generic recurrent network have not been able to produce the precise and sparse neuronal activity of HVC-RA neurons.

In contrast, highly structured networks rely on the pre-built connectivity to produce sequences [63]. Recurrent networks with global dominant inhibition are capable of producing precise spike sequences [64]. However, before converging to the spike sequence attractor, the network generates transient spikes, which depend on the initial network state. Such transient state is not observed in real songbird HVC.

So far, different approaches to construct recurrent neural networks that produce precise and sparse sequence of spikes did not succeed. In fact, there is another reason why recurrent neural network is not likely to exist in HVC. Most recurrent network models assume dense connectivity between the neurons, with some models connecting neurons in all-to-all manner. The recurrent networks are called sparsely connected when probability of connecting another neuron is  $\sim 0.1$ . While such connectivity is reasonable for cortical circuits, HVC-RA neurons are much more sparsely connected with connection probability  $\sim 0.008$  [50]. Such extremely sparse connectivity requires very strong synapses or highly convergent inputs to allow robust sequence propagation. Since exceptionally strong synapses are not observed in HVC [65], it is likely that the HVC-RA neurons receive convergent inputs, pointing out to feedforward network topology. Indeed, a simple feedforward network with sparse connectivity - synfire chain, is able to produce precise and sparse temporal activity and remains the most popular model for songbird HVC [66].

### 1.2.1 Synfire chain

The idea of synfire chain dates back to the work of Abeles [67,68]. Synfire chain is a feedforward network that consists of groups (or layers) of neurons connected sequentially in all-to-all manner to the neurons in the subsequent group in the chain (see Fig. 1.5A). When neurons in the first group, i.e., starter neurons, are excited, they transmit the excitation to the neurons in the second group. They, in turn, excite the neurons in the third group and the process repeats, resembling the falling chain of dominos. During signal propagation along the chain, activity of the neurons in the same group is highly synchronous. It was shown that synfire chains are able to self-correct a perturbation in spike times of the starter neurons, converging to a synchronous group activity [69]. Such robustness of the synfire chain makes it an attractive biological

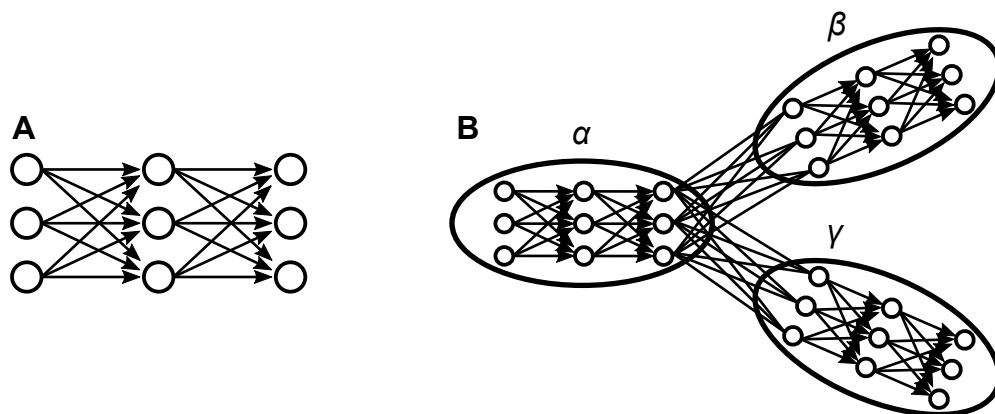


**Figure 1.5.** Single synfire chain and branching chain network. (A) Single synfire chain that consists of 3 groups of neurons with 3 neurons per each group. Lines show excitatory connections between the neurons. Neurons in the first group of the synfire chain are called starter neurons. If starter neurons are excited, activity propagates robustly along the chain. (B) Branching chain network that is made of 3 synfire chains connected at the branching point. Each synfire chain represents a distinct syllable in the song marked by a greek letter. Branching points represent transitions between different syllables in the song. With this approach, the entire songbird syntax can be modeled as a collection of synfire chains and branching points.

model for sequential behaviors. Computational HVC models based on synfire chains demonstrate sub-millisecond precision in neuronal spike times, which is consistent with experimental observations [66].

Typically, one synfire chain represents a single syllable in the songbird song. To model a complex songbird syntax with many transitions between syllables, such as the syntax of Bengalese finch, synfire chains can be connected together to form branching chain network [70] (see Fig. 1.5B). When neural activity reaches the branching point, one syllable is selected through a winner-take-all probabilistic mechanism.

Synfire chain is an idealistic network topology which maps a synchronous presynaptic activity to a synchronous postsynaptic activity. However, real neural circuits possess inhomogeneities, which can make synfire chain not optimal network for signal propagation. Common source of inhomogeneity is a distribution of axonal conduction delays. If axonal conduction delays are not the same, synchronous presynaptic activity will no longer result in the synchronous input to postsynaptic neurons. Another type of feedforward network, called a polychronous network, uses distributed axonal conduction delays to convert non-synchronous presynaptic activity into synchronous input.

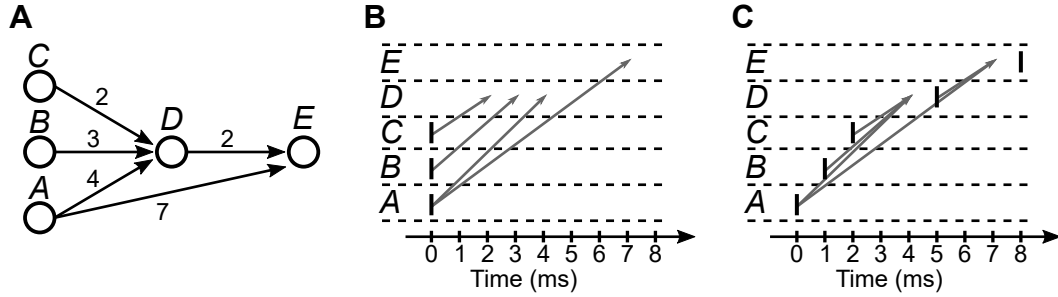


**Figure 1.6.** Significance of axonal conduction delays. (A) A small network of 5 excitatory neurons wired with different axonal conduction delays. Delay values in milliseconds are indicated near the arrows that represent excitatory connections. (B-C) Raster plots with spikes of the network neurons under different spike times of starter neurons A, B and C. (B) Starter neurons fire synchronously. Due to different axonal conduction delays, inputs to neuron D do not arrive synchronously, do not sum up efficiently and produce weak depolarization not enough to elicit a spike. Neuron E receives a single input from neuron D and also remains silent. (C) Starter neurons spike at different times to compensate inhomogeneous axonal conduction delays. Inputs to neuron D arrive synchronously and make it fire. As a result, neuron E receives synchronous inputs from neurons A and D and also fires.

### 1.2.2 Polychronous network

The idea of a feedforward network with axonal conduction delays such that inputs arrive synchronously to postsynaptic neurons goes back to the work of Bienenstock [71]. In the paper, Bienenstock calls such network a synfire braid and provides some theoretical estimations of synfire braid memory capacity without a computational implementation. The same idea was re-discovered later in the studies of Izhikevich, where short time-locked neuronal sequences with synchronous inputs emerged spontaneously through spike-timing dependent plasticity (STDP) rules [72,73]. Izhikevich named the sequences polychronous, where *poly* means many and *chronous* means time or clock in Greek. Such choice of terminology reflects that neural activity in the polychronous sequence is time-locked, repeatable, but not synchronous.

Let's consider a simple example of a small network with axonal conduction delays for illustration purposes (see Fig. 1.6). Five neurons A, B, C, D, and E, are wired with different axonal conduction delays. If neurons A, B and C spike synchronously at time  $t = 0$  ms, neuron D receives three non-synchronous inputs at times 4 ms, 3 ms and 2 ms correspondingly. Since the inputs are not synchronous, they may not sum up efficiently and neuron D may fail to spike. In this case, neuron E will receive a single input from neuron A at 7 ms and again may not spike due to the input being too weak. If instead neuron C fires at 2 ms, neuron B at 1 ms, and neuron A at 0 ms, all inputs

will arrive synchronously at neuron D at time  $t = 4$  ms, and it should spike reliably. If the integration time of neuron D is 1 ms, it will spike at time  $t = 5$  ms and neuron E will receive synchronous inputs from neurons C and D at time  $t = 7$  ms. Again, such synchronous input should be enough to produce robust spiking of neuron E.

Therefore, distributed axonal conduction delays provide additional degrees of freedom for the neural system. Moreover, infinite resolution of axonal conduction delays effectively converts neural network into infinite dimensional dynamic system [73]. Built with distributed axonal conduction delays, polychronous networks can provide synchronous inputs to all network neurons, and therefore use synapses in the most efficient way. Up to date, only short and non-stable polychronous sequences emerging through STDP rules were explored. In this dissertation, we develop two models to produce large polychronous networks and explore the properties of temporal sequences generated by these networks.

## 1.3 Outline

A brief outline of the remaining chapters of the dissertation is the following:

- Chapter 2: This chapter presents original computational neuron models used in subsequent simulations, and discusses approaches to minimize the associated computational cost.
- Chapter 3: This chapter constructs a detailed computational model of the microcircuit of songbird nucleus HVC for zebra finch. The model contains realistic number of neurons and incorporates all experimentally known features of HVC, including spatial distributions of neurons and distributed axonal conduction delays. It compares the neural dynamics produced by networks with different connectivity patterns between HVC-RA neurons.
- Chapter 4: This chapter presents a model for temporal sequence formation in HVC during songbird vocal development. The model is built on the hypothesis that immature neurons, provided by neurogenesis, are more spontaneously active and become prime targets of self-organizing process via synaptic plasticity.

# Chapter 2 |

## Computational models

Our goal is get a complete understanding of neural circuits and therefore we follow a bottom-up approach for simulating dynamics of neural networks. We start with modeling dynamics of individual neurons. The neurons are subsequently connected with each other via synapses to form neural networks, whose dynamics is our main focus of interest.

Over the years, many computational neuron models have been developed to gain insights into neural systems. Neurons have been treated as simple binary state systems [74], more complex integrate-and-fire capacitor-like elements [75], non-linear oscillators [76], two dimensional dynamic systems with attractors (e.g., Izhikevich model [77]), and biologically driven electrical circuit representations [78]. Simple models are usually fast to simulate on computers, which gives an opportunity to investigate the behavior of large neural networks. However, simple models provide poor approximation to dynamics of individual neurons. In contrast, complex models generate more realistic neural responses, but are more computationally demanding. We chose Hodgkin-Huxley type neuron models, since they are biologically-motivated and produce realistic-looking action potentials.

In this chapter, we describe the original computational neuron models for interneurons and RA-projection neurons in songbird HVC [66, 70]. To better suit the needs of our simulations, the neuron models are modified in the subsequent chapters of this dissertation. We also describe models for synaptic connections between neurons and noise fluctuations in membrane potentials. Finally, we compare different numerical methods for simulating dynamics of single neurons and discuss the advantage of parallel computing for large scale network simulations.

## 2.1 HVC-RA neuron model

As described in Introduction, HVC-RA neurons typically produce a single high frequency burst of spikes per song motif. Electrophysiological experiments show no bursting behavior of HVC-RA neurons when current is injected into the soma [79–81]. Recent study provides a strong evidence that the burst is generated intrinsically by L-type calcium current (where "L" stands for long-lasting, referring to the length of activation) and resembles a dendritic calcium spike observed in many neurons [66].

To account for the experimental observations, HVC-RA neurons are modeled as two-compartmental Hodgkin-Huxley neurons with soma and dendrite (see Fig. 2.1A). When external current is injected to the dendritic compartment, it generates a strong calcium spike that drives robust and stereotyped burst in somatic compartment (see Fig. 2.1B). In contrast, when current is injected to the soma, there is no calcium spike in the dendrite. Instead, the soma fires a sequence of spikes that depends on the current magnitude, which is consistent with electrophysiological studies (see Fig. 2.1C).

Stereotyped dendritic calcium spike is produced by the interplay of two currents in the dendrite: the high-voltage activated calcium current (with voltage-dependent conductance  $G_{Ca}$  and reversal potential  $E_{Ca}$ ) and calcium-dependent potassium current (with voltage and calcium concentration dependent conductance  $G_{Ca,K}$  and reversal potential  $E_K$ ) (see Fig. 2.1D). When dendritic membrane potential is sufficiently high, calcium current gets activated and leads to a rapid and prolonged depolarization of the dendritic compartment - the dendritic spike. During dendritic spike, there is a build up of calcium concentration inside the dendrite, which results in the activation of calcium-dependent potassium current. This current hyperpolarizes the dendrite and serves as a stopping mechanism for dendritic spike.

Somatic compartment is equipped with almost classical sodium (with voltage-dependent conductance  $G_{Na}$  and reversal potential  $E_{Na}$ ) and potassium (with voltage-dependent conductance  $G_K$  and reversal potential  $E_K$ ) channels for spike generation. During stereotyped dendritic spike, the soma receives a steady influx of current from the dendrite. It depolarizes the somatic membrane potential high enough to activate the voltage-dependent sodium current. Sodium current provides a rapid depolarization of the soma, which in turn activates a delay-rectified potassium current responsible for bringing the membrane potential down and stopping the spike. Dendritic spike duration of  $\sim 10$  ms allows soma to produce 4-5 spikes, which is consistent with experimental observations. Fig. 2.1E illustrates the interplay between spike-generating currents in the somatic

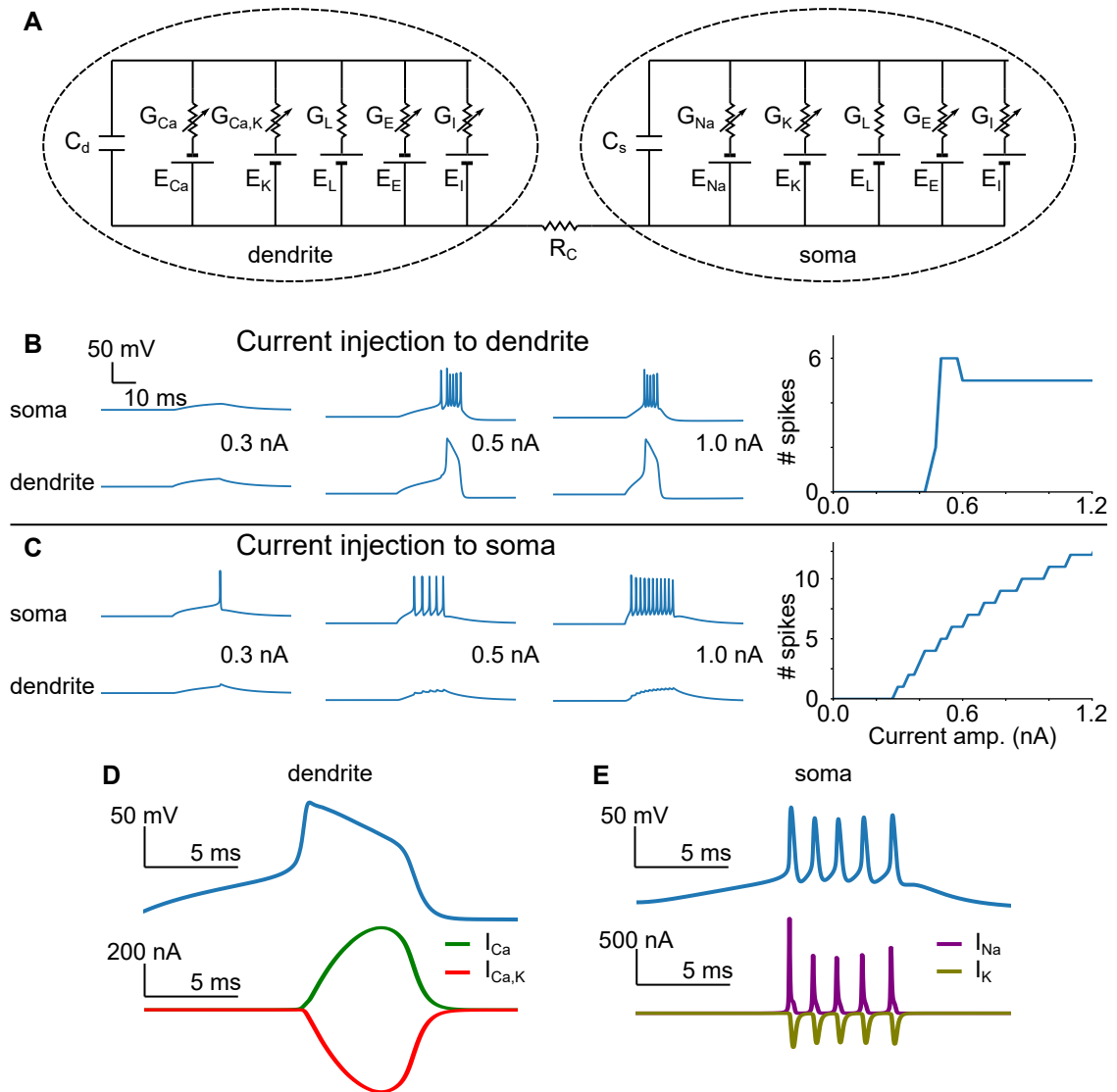


**Figure 2.1.** Computational model of HVC-RA neuron. (A) Equivalent electrical circuit representation of HVC-RA neuron, showing both dendritic and somatic compartments, and ionic membrane channels. (B) Response of the model to the pulsed current of 20 ms duration injected to dendrite. Left: 3 examples of neuronal responses to different current amplitudes. Right: Cumulative graph showing number of somatic spikes versus current amplitude. (C) Response of the model to the pulsed current of 20 ms duration injected to soma. Left: 3 examples of neuronal responses to different current amplitudes. Right: Cumulative graph showing number of somatic spikes versus current amplitude. (D) Top: Dendritic membrane potential during dendritic spike. Bottom: Calcium and calcium-dependent currents during dendritic spike. (E) Top: Somatic membrane potential during dendritic spike. Bottom: Sodium and potassium currents during dendritic spike.

Reversal potentials (mV)	Conductances (mS/cm <sup>2</sup> )	Gating time constants (ms)	Gating limit values
E <sub>L</sub> = -80	G <sub>L</sub> = 0.1	$\tau_n = 0.1 + \frac{0.5}{1+\exp((V+27)/15)}$	$n_\infty = \frac{1}{1+\exp(-(V+35)/10)}$
E <sub>Na</sub> = 55	G <sub>Na</sub> = 60	$\tau_h = 0.1 + \frac{0.75}{1+\exp((V+40.5)/6)}$	$h_\infty = \frac{1}{1+\exp((V+45)/7)}$
E <sub>K</sub> = -90	G <sub>K</sub> = 8	$\tau_r = 1.0$	$m_\infty = \frac{1}{1+\exp(-(V+30)/9.5)}$
E <sub>Ca</sub> = 120	G <sub>Ca</sub> = 55	$\tau_c = 10$	$r_\infty = \frac{1}{1+\exp(-(V+5)/10)}$
E <sub>I</sub> = -80	G <sub>CaK</sub> = 150		$c_\infty = \frac{1}{1+\exp(-(V-10)/7)}$
E <sub>E</sub> = 0			
Miscellaneous:		A <sub>d</sub> = 10000 μm <sup>2</sup> A <sub>s</sub> = 5000 μm <sup>2</sup>	R <sub>c</sub> = 55 MΩ C <sub>m</sub> = 1 μF/cm <sup>2</sup>

**Table 2.1.** Parameters of HVC-RA neuron model

compartment during the dendritic spike.

The membrane potentials of somatic ( $V_s$ ) and dendritic compartments ( $V_d$ ) evolve according to the following equations:

$$C_m A_s \frac{dV_s}{dt} = A_s (I_{s,L} + I_{s,K} + I_{s,Na}) + I_{s,ext} + \frac{V_d - V_s}{R_c}$$

$$C_m A_d \frac{dV_d}{dt} = A_d (I_{d,L} + I_{d,Ca} + I_{d,CaK} + I_{d,exc} + I_{d,inh}) + I_{d,ext} + \frac{V_s - V_d}{R_c}$$

where  $C_m$  - membrane capacitance per unit area,  $R_c$  - resistance of the coupling link connecting soma and dendrite;  $A_s$  and  $A_d$  - somatic and dendritic compartment surface areas;  $I_{s,L} = -G_{s,L}(V_s - E_L)$  and  $I_{d,L} = -G_{d,L}(V_d - E_L)$  - somatic and dendritic leak currents;  $I_{s,ext}$  and  $I_{d,ext}$  - somatic and dendritic external currents;  $I_{s,K} = -G_K n^4 (V_s - E_K)$  - somatic potassium current;  $I_{s,Na} = -G_{Na} m_\infty^3 h (V_s - E_{Na})$  - somatic sodium current;  $I_{d,Ca} = -G_{Ca} r^2 (V_d - E_{Ca})$  - dendritic calcium current;  $I_{d,CaK} = -G_{CaK} c / (1 + 6/[Ca]) (V_d - E_K)$  - dendritic calcium-dependent potassium current;  $I_{d,exc} = -G_E (V_d - E_E)$  - dendritic synaptic excitatory current;  $I_{d,inh} = -G_I (V_d - E_I)$  - dendritic synaptic inhibitory current. Leak conductance in somatic and dendritic compartments have the same value  $G_{s,L} = G_{d,L} = G_L$ .

Gating variables  $n, h, r, c$  obey the following differential equation:  $\tau_x dx/dt = x_\infty(V) - x$ , where  $x = n, h, r, c$ .

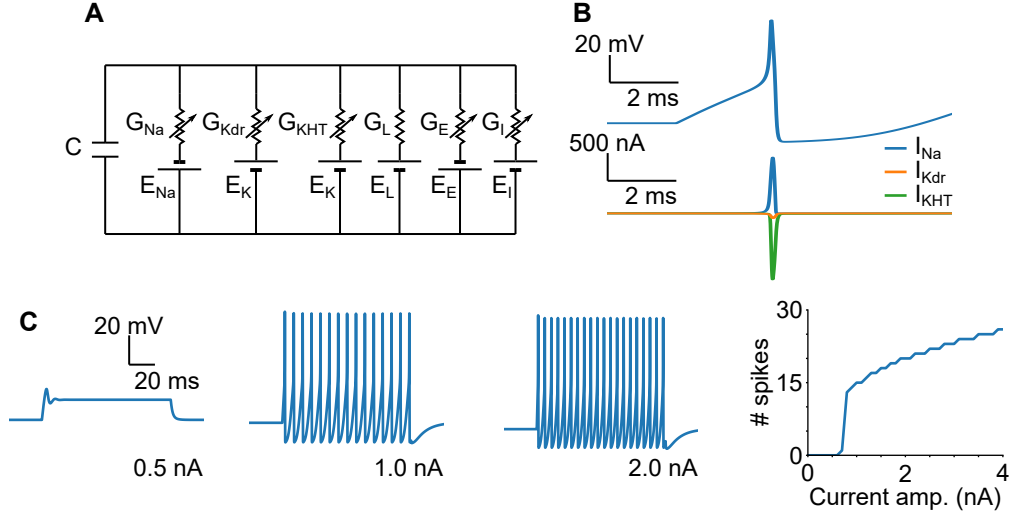


**Figure 2.2.** Computational model of HVC-I neuron. (A) Equivalent electrical circuit representation of HVC-I neuron, showing ionic membrane channels. (B) Top: Membrane potential during spike. Bottom: Sodium, potassium delay-rectified and high threshold potassium currents during spike. (C) Response of the model to the external pulsed current injection of 150 ms duration. Left: 3 examples of neuronal responses to different current amplitudes. Right: Cumulative graph showing number of spikes versus current amplitude.

Concentration of calcium ions inside dendritic compartment increases with the influx of calcium current and is buffered away by the internal ionic pumps responsible for maintaining the homeostatic calcium concentration:

$$\frac{d[Ca]}{dt} = 0.1I_{d,Ca} - 0.02[Ca]$$

Numerical values for all parameters of HVC-RA computational neuron model are given in Table 2.1.

## 2.2 HVC-I neuron model

HVC-I neurons spike frequently during the song motif. Therefore, we use a fast-spiking Hodgkin-Huxley type neuron model with a single compartment (see Fig. 2.2A). To generate a spike, the membrane is equipped with sodium (with voltage-dependent conductance  $G_{Na}$  and reversal potential  $E_{Na}$ ), delay-rectified potassium (with voltage-dependent conductance  $G_{Kdr}$  and reversal potential  $E_K$ ) and high threshold potassium channels (with voltage-dependent conductance  $G_{KHT}$  and reversal potential  $E_K$ ). As in

Reversal potentials (mV)	Conductances (mS/cm <sup>2</sup> )	Gating voltage dependence	
$E_L = -65$	$G_L = 0.1$	$a_n = \frac{0.15(V+15)}{1-\exp(-(V+15)/10)}$	$b_n = 0.2 \exp(-(V+25)/80)$
$E_{Na} = 55$	$G_{Na} = 100$	$a_m = \frac{V+22}{1-\exp(-(V+22)/10)}$	$b_m = 40 \exp(-(V+47)/18)$
$E_K = -80$	$G_{Kdr} = 20$	$a_h = 0.7 \exp(-(V+34)/20)$	$b_h = \frac{10}{1+\exp(-(V+4)/10)}$
$E_I = -75$	$G_{KHT} = 500$	$w_\infty = \frac{1}{1+\exp(-V/5)}$	
$E_E = 0$		$\tau_w = 1.0 \text{ ms}$	
Miscellaneous:		$A = 6000 \mu\text{m}^2$	$C_m = 1 \mu\text{F/cm}^2$

**Table 2.2.** Parameters of HVC-I neuron model

the classical Hodgkin-Huxley model, the spike is initiated by the activation of sodium current. High-threshold potassium current only activates at high voltage and is responsible for a quick membrane potential reset. It decreases the refractory period of the neuron model, so that the neuron can sustain high frequency firing. Fig. 2.2B shows the interplay between spike-generating currents during the spike. Neuron model responses to a pulsed current injections of 150 ms duration are shown in Fig. 2.2C. Frequency of generated spike train increases almost linearly with the increase in current amplitude, confirming that the model is able to maintain a high frequency firing regime.

The membrane potentials  $V$  evolves according to the following equation:

$$C_m A \frac{dV}{dt} = A(I_L + I_{Kdr} + I_{KHT} + I_{Na} + I_{exc} + I_{inh}) + I_{ext}$$

where  $C_m$  - membrane capacitance per unit area,  $A$  - membrane surface area;  $I_L = -G_L(V - E_L)$  - leak current;  $I_{ext}$  - external current;  $I_{Kdr} = -G_K n^4(V - E_K)$  - delay-rectified potassium current;  $I_{KHT} = -G_K w(V - E_K)$  - high threshold potassium current;  $I_{Na} = -G_{Na} m^3 h(V - E_{Na})$  - sodium current;  $I_{exc} = -G_E(V - E_E)$  - synaptic excitatory current;  $I_{inh} = -G_I(V - E_I)$  - synaptic inhibitory current.

Gating variables  $n, m, h$  obey the following differential equation:  $\tau_x dx/dt = \alpha_x(V)(1 - x) - \beta_x(V)x$ , where  $x = n, m, h$ , and  $\alpha_x(V), \beta_x(V)$  - corresponding opening and closing voltage dependent rates.

Gating variable  $w$  follows the following equation:  $\tau_w dw/dt = w_\infty(V) - w$ .

Numerical values for all parameters of HVC-I computational neuron model are given

in Table 2.2.

## 2.3 Synaptic model

We model connections to HVC-RA and HVC-I neurons as conductance-based "kick-and-decay" synapses. When a presynaptic neuron fires an action potential, the excitation travels along its axon to reach the presynaptic terminal. After receiving a depolarization, the vesicles in the presynaptic terminal fuse with the membrane and release the trapped neurotransmitter into the synaptic cleft. The neurotransmitter binds to the receptors on the postsynaptic terminal and leads to their opening. Depending on the type of open receptor, positive or negative ions enter the postsynaptic cell and affect its membrane potential. Gradually, the concentration of neurotransmitter in synaptic cleft is buffered away by the enzymes in the subsynaptic membrane and/or reuptake pumps in presynaptic terminal. During that time, permeability of the receptors on the postsynaptic terminal decreases. Eventually the receptors close completely, ending the synaptic transmission. "Kick-and-decay" synapses assume instantaneous neurotransmitter release and binding to the receptors in the postsynaptic terminal. It is modeled as an instantaneous increase in the synaptic conductance:  $g_{exc,inh} \rightarrow g_{exc,inh} + \Delta g$ , where  $\Delta g$  is the strength of the synapse. Then, the gradual closing of the receptors is modeled as an exponential decay with time constant representing the neurotransmitter decay dynamics:

$$\tau_{exc,inh} \frac{dg_{exc,inh}}{dt} = -g_{exc,inh}$$

For HVC-RA neuron, we make synapses only on the dendritic compartment. Numerical values of conductance decay times for HVC-RA and HVC-I computational neuron models are given in Table 2.3.

HVC-RA	HVC-I
$\tau_{exc} = 5 \text{ ms}$	$\tau_{exc} = 2 \text{ ms}$
$\tau_{inh} = 5 \text{ ms}$	$\tau_{inh} = 5 \text{ ms}$

**Table 2.3.** Synaptic parameters of neuron models

## 2.4 Noise model

When recorded, membrane potential of all neurons demonstrates random fluctuations - noise. There are multiple sources of neuronal noise: thermal noise, ionic channel noise and synaptic noise. Thermal noise, also known as Johnson-Nyquist noise, is caused by the thermal agitation of the charge carriers - ions. It represents a fundamental lower limit of the membrane potential fluctuations and can only be reduced by decreasing the temperature. Ionic channel noise originates from the stochastic nature of ionic channel. Random openings and closings of ionic channels produce fluctuations in the number of active channels and lead to the membrane potential fluctuations. Finally, synaptic noise is caused by the external inputs from randomly spiking neurons. Typical cortical neuron receives  $\sim 30000$  inputs from other neurons [82], and experiences a constant bombardment of synaptic activity. Thermal noise is much smaller than other noise types [83] and can safely be ignored for our purposes. Membrane potential fluctuations are usually dominated by the synaptic noise.

We hypothesize that random dynamics of HVC-I neurons is dominated by the synaptic noise. Thus, we model noise in HVC-I neurons as random external excitatory and inhibitory spike trains. Both spike trains are generated by Poisson processes with an average firing rate of  $250 \text{ Hz}$ . When excitatory (inhibitory) random external spike arrives, excitatory (inhibitory) conductance of the neuron is increased by a random value sampled from a uniform distribution between 0 and  $0.45 \text{ mS/cm}^2$ . With this level of noise, HVC-I neuron spikes spontaneously with firing rate  $\sim 10 \text{ Hz}$ , which is consistent

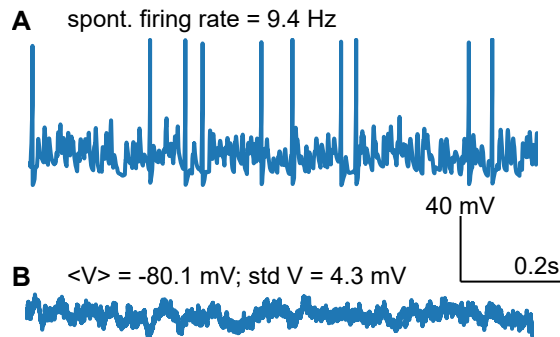


**Figure 2.3.** Membrane potential fluctuations of HVC-I and HVC-RA neurons. (A) Spontaneous activity of HVC-I neuron. HVC-I neuron receives external random excitatory and inhibitory spike trains generated by Poisson process with frequency  $250 \text{ Hz}$ . The input causes HVC-I neuron to spike with an average frequency  $\sim 10 \text{ Hz}$ . (B) Membrane potential fluctuations of HVC-RA neuron under white noise current injections with amplitude  $0.14 \text{ nA}$  to somatic and  $0.2 \text{ nA}$  to dendritic compartments. HVC-RA neuron does not spontaneously spike.

with experimental observations in HVC [66]. An example of HVC-I membrane potential fluctuations is shown in Fig. 2.3A.

Since in Chapter 4 we are going to model the neurogenesis process, according to which new HVC-RA neurons are added to songbird HVC, we need a different approach to simulate noise in HVC-RA neurons. New neurons take some time to incorporate into existing networks and typically do not receive many synaptic inputs. Thus, synaptic noise is unlikely to dominate membrane potential fluctuations in new neurons. We model noise in both new and mature HVC-RA neurons as white noise current injections to both somatic and dendritic compartments. White noise amplitude of 0.14 nA and 0.2 nA in somatic and dendritic compartments correspondingly, generates membrane potential fluctuations with standard deviation  $\sim 4.3\text{mV}$ , which is similar to noise in real HVC-RA neurons (see Fig. 2.3B).

## 2.5 Simulation of neuron dynamics

Hodgkin-Huxley type neuron models are more computationally expensive than alternative simpler models, for example, integrate-and-fire or Izhikevich neuron model. This is due to the existence of a small time scale in the neuron dynamics - the spike. Neuronal spikes typically last less than a millisecond, so the models that explicitly simulate spike shapes have to resolve to fine sub-millisecond scale time grid. Popular integrate-and-fire and Izhikevich neuron models do not fully simulate the spike shape. According to integrate-and-fire neuron model, the spike is drawn artificially at the time point when neuron membrane potential crosses a threshold. Then the membrane potential is reset to some hyperpolarized value, representing the end of the spike. In addition to the membrane potential, Izhikevich neuron model uses recovery variable and is able to model an action potential upstroke. However, similarly to the integrate-and-fire model, the downstroke of the action potential is created artificially by the membrane potential reset. Hodgkin-Huxley neuron model does not have a threshold nor the reset of the voltage. Instead, it produces the spikes explicitly and therefore suffers from the increased computational costs.

### 2.5.1 Simulation of HVC-RA neuron model

Two-compartment Hodgkin-Huxley model that we use to model HVC-RA neurons, contains 10 variables: 5 gating variables  $n, h, r, c, m$  with non-linear voltage-dependence;

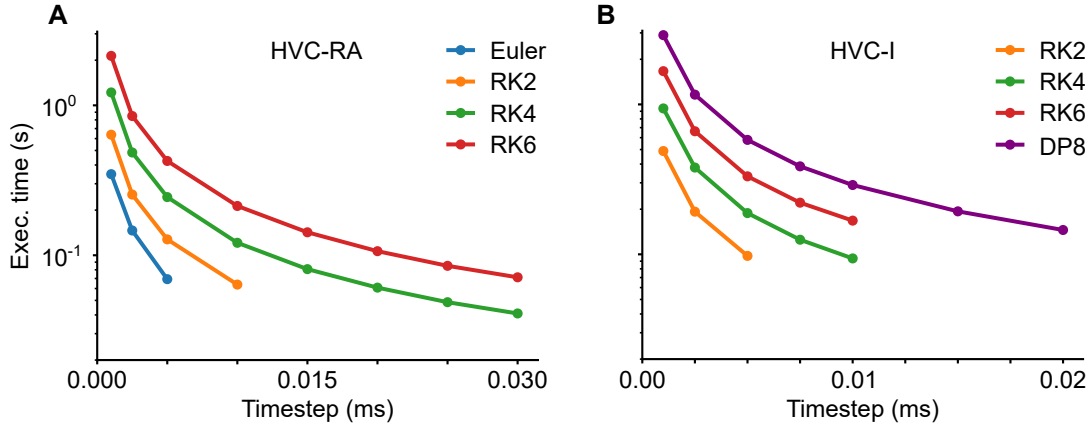


**Figure 2.4.** Comparison of numerical methods for simulating neuron dynamics. Execution time of 1 second of neural dynamics (model time) on a single Intel(R) Xeon(R) Gold 6148 CPU @ 2.40GHz using different numerical methods for (A) HVC-RA neuron and (B) HVC-I neuron. The following explicit numerical methods are compared: Euler - 1st order; RK2 - midpoint Runge-Kutta method of order 2; RK4 - 3/8 Runge-Kutta method of order 4; RK6 - seven stage Runge-Kutta method of order 6; DP8 - Dormand–Prince method of order 8

concentration of calcium ions inside dendritic compartment  $[Ca]$ ; somatic and dendritic membrane potentials  $V_s$  and  $V_d$ ; and dendritic excitatory and inhibitory conductance. Somatic spike width is  $\sim 0.3$  ms, which requires a high-resolution time grid to simulate the dynamics. Together, it makes HVC-RA neurons computationally expensive and motivates us to find an optimal approach to simulate their dynamics. Below we compare different numerical methods for simulating HVC-RA neurons.

First, we focus on simulating dynamics of HVC-RA neuron receiving no noise. In this case, the problem reduces to solving a system of ordinary differential equations (ODEs). Two broad categories of methods for solving ODEs are implicit and explicit. Both types of methods create a time grid and update variable values step-by-step, starting from the leftmost time point where initial conditions are defined (Cauchy’s problem). Implicit methods do not provide a direct formula for the variable update. Instead, they define the update implicitly through a system of non-linear equations, which needs to be solved. In contrast, explicit methods provide a direct update expression. While implicit methods are typically more stable, the cost associated with solving a system of non-linear equations is too big in our case. Therefore, in our comparisons we will only work with explicit methods for solving ODEs.

To compare different numerical methods, we simulate 100 seconds of HVC-RA neural dynamics. Then, we estimate an execution time as a real CPU time needed to simulate 1 second of neural dynamics. Since CPU load is constantly changing due to operating

system tasks, we repeat simulations 5 times and compute an average. To verify that numerical method produces correct results, we compare frequency-current tuning curves with the etalon curves obtained with high accuracy Runge Kutta order 4 method with small time step 0.001 ms (see Fig. 2.1B-C). The simulations are performed on a single Intel(R) Xeon(R) Gold 6148 CPU @ 2.40GHz using custom C++ code compiled with gcc 7.4.0 on Ubuntu 18.04 LTS. The following numerical methods are compared: Euler’s 1st order method; midpoint Runge-Kutta method of order 2; 3/8-rule Runge-Kutta method of order 4; seven stage Runge-Kutta method of order 6 [84].

Fig. 2.4A shows the CPU execution time of 1 second of HVC-RA neural dynamics for explicit Runge-Kutta methods of different order. Low-order methods, such as Euler’s method, need small number of function evaluations and are faster to simulate at small time steps of dynamics. However, these methods are not accurate enough at large time steps, which leads to their divergence. High-order methods, such Runge Kutta order 4, are more computationally expensive, but they can work at larger time steps. In our case, cheap Euler’s method can only be used for time steps  $\leq 0.005$  ms, while expensive Runge Kutta order 4 provides accurate results for time steps up to 0.03 ms. At time step 0.03 ms, the execution time for Runge Kutta order 4 ( $\sim 0.041$  s) is actually smaller than the execution time of low-order methods at the largest valid time steps. For Euler’s method, the smallest execution time is  $\sim 0.069$  s for time step 0.005 ms. For Runge Kutta order 2, the smallest execution time is  $\sim 0.064$  s for time step 0.01 ms. More accurate Runge Kutta order 6 method has the same upper bound of 0.03 ms for the largest valid time step, and is almost two times slower ( $\sim 0.071$  s). We attribute the saturation of the largest valid time step size to the existence of short time scales in the system of ODEs. No matter how accurate the numerical method is, it is not possible to simulate fast spike dynamics on a grid with large time steps. We conclude that Runge Kutta order 4 method with time step 0.03 ms is the optimal approach to simulate dynamics of HVC-RA neuron model in the absence of noise.

To simulate dynamics of HVC-RA neuron receiving white noise current stimulus, we use the *Itô* interpretation of stochastic differential equations (SDEs). To solve a system of SDEs, we apply 3rd order weak AN3D1 method [85], which shows the same upper bound on time steps as Runge Kutta order 4. Its execution time of 0.047 s at time step 0.03 ms is similar to the execution time of Runge Kutta order 4 method.

## 2.5.2 Simulation of HVC-I neuron model

The model of HVC-I neuron is one compartment model containing 7 variables: 4 gating variables  $n, m, h, w$ ; membrane potential  $V$ ; and excitatory and inhibitory conductances. Thus, it is less computationally expensive than HVC-RA model. However, due to high-frequency fast spiking and short spike width, HVC-I neurons require smaller time steps for dynamics simulations. Using similar procedure as for HVC-RA neurons, we estimate a CPU execution time needed to simulate 1 second time of HVC-I neuron dynamics (see Fig. 2.4B). Euler’s method fails to converge for time steps  $\geq 0.0005$  ms, so we don’t report it here. Runge Kutta order 4 and order 6 methods work for time steps up to 0.01 ms, with order 4 method being the optimal for this range of time steps, with execution time 0.093 ms. More accurate order 8 Dormand-Prince method [84] extends the valid time step to 0.02 ms, but has larger execution time of 0.145 ms. We conclude that Runge Kutta order 4 method with time step 0.01 ms is the optimal approach to simulate dynamics of HVC-I neuron model.

## 2.6 Simulation of network dynamics

Songbird HVC of adult zebra finch contains roughly 20,000 song-related HVC-RA and 5,500 HVC-I neurons (see Chapter 3). Therefore, full scale simulations of HVC are computationally expensive and require a careful choice of the time step size. With this ratio of excitatory to inhibitory neurons, it is advantageous to optimize the simulation costs for HVC-RA neurons even if it leads to non-optimal costs for HVC-I neurons. Since simulation costs decrease with the time step size, we set the largest time step valid for both HVC-RA and HVC-I neurons. It corresponds to the time step of 0.02 ms. Thus, for network simulations, dynamics of HVC-RA neurons with noise is simulated with AN3D1 method and dynamics of HVC-I neurons is simulated with order 8 Dormand-Prince method. Simulation of 1 second of neural network dynamics with 20,000 HVC-RA and 5,500 HVC-I non-connected neurons takes  $20000 * 0.071 + 5500 * 0.145 \sim 2218$  CPU seconds.

Serial simulations of non-connected neural network already take a significant amount of time. However, simulations of connected neural networks differ qualitatively from non-connected networks and pose additional challenges. Outside of spiking events, neurons do not interact with each other and can be simulated in completely independent way. When spikes occur, they need to be transmitted to the corresponding postsynaptic neurons.

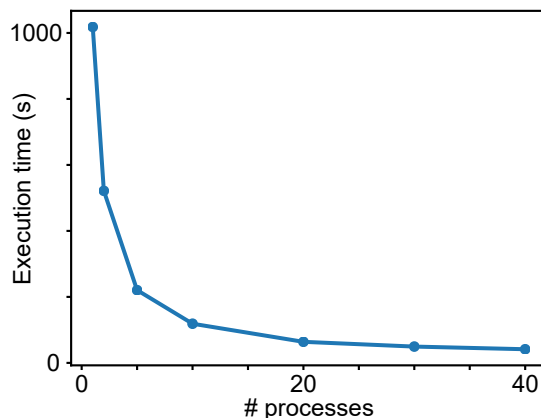


**Figure 2.5.** Scaling of network dynamics simulation time with number of MPI processes. Simulated network is a synfire chain with 100 groups (200 neurons per group) of HVC-RA neurons and 5,500 HVC-I neurons. See text for the details on the connection probabilities between neurons and synaptic weight strength.

Therefore, the neurons have to synchronize and the frequency of synchronization depends on the network activity. If neurons spike frequently, many synchronizations are needed which can significantly slow down the execution time.

To reduce the simulation time, we apply parallelization. Two major parallelization methods are threads and processes. Thread parallelization is supported by hardware CPU architecture by duplicating transistor elements for arithmetic operations. Threads are run on the same machine and use the same memory. Thus, this type of parallelization is called shared memory. Shared memory parallelization is limited by the the number of threads that are supported by a single CPU. Unless CPU supports hypethreading, the number of threads matches the number of CPU cores.

Another type of parallelization, called distributed memory, uses processes to speed up the execution time. Each process has its own memory and runs independently, except for the need of data exchange with other processes. The data exchange is managed by sending messages between processes and is supported by an operating system. The usage of processes allows to run a program on a computational cluster with different machines, potentially providing unlimited computational power.

For our purposes, we need a scalable solution that could be run on Penn State computational clusters and therefore we choose parallelization with distributed memory. To implement the parallelization, we use a popular C++ library openMPI. To illustrate how network simulation time scales with the number of processes used, we create a synfire chain network with 100 groups (200 neurons per group) of HVC-RA neurons and 5,500 HVC-I neurons. Excitatory synaptic weight strength for HVC-RA to HVC-RA

connections is sampled randomly between 0 and  $0.05 \text{ mS/cm}^2$ . There is 0.05 probability for an HVC-RA neuron to contact an interneuron and an excitatory synaptic weight strength is sampled randomly between 0 and  $0.075 \text{ mS/cm}^2$ . Similarly, there is 0.1 probability for an HVC-I neuron to contact an HVC-RA neuron and an inhibitory synaptic weight strength is sampled randomly between 0 and  $0.03 \text{ mS/cm}^2$ . Simulations are run on a machine with two Intel(R) Xeon(R) Gold 6148 CPU @ 2.40GHz CPUs (2x20 cores) and 128 GB RAM. We use a custom C++ code compiled with gcc 7.4.0 on Ubuntu 18.04 LTS. Fig. 2.5 shows how network simulation time depends on the number of MPI processes used. There is  $\sim 25$  times speed up when using 40 MPI processes compared to a single MPI process. The speed up doesn't reach the ideal value of 40 because of the required non-parallelizable serial work and synchronization between the processes to transmit spiking events. We conclude that the usage of openMPI to parallelize simulations of neural networks significantly decreases the simulation time.

## 2.7 Conclusions

In this section, we used a bottom-up approach to construct a neural network model. We started by describing neuron computational models, then added noise to produce membrane potential fluctuations and spontaneous activity, and finally connected neurons by synapses to create neural networks. Described Hodgkin-Huxley models for HVC-RA and HVC-I neurons produce responses similar to the neurons in real HVC. HVC-I neuron is capable to operate in a fast-spiking regime and produces spontaneous activity at frequency  $\sim 10 \text{ Hz}$ . Due to a strong calcium spike in dendritic compartment, HVC-RA neuron operates in a binary mode: it is silent when the synaptic input is weak, or elicits a stereotypical tight burst of somatic spikes otherwise. Such all-or-none behavior of HVC-RA neuron makes it more robust to perturbations. Comparison of different numerical methods of solving differential equations showed that a careful choice of the time resolution and an appropriate numerical method significantly improves the network simulation speed. Parallelization technique which uses MPI processes further reduces the execution time of simulations.

# Chapter 3 |

## Modeling HVC microcircuit

Until recently, songbird HVC was characterized by recorded activity of a handful of neurons and not much was known about the spatial organization of connections between the neurons. Using state-of-the art calcium-imaging [86], neural morphology reconstructions [50], and axonal delay measurements [87], new studies shed more light on the HVC circuitry and allow testing the existing microcircuit models.

In this chapter, we develop a biological computational model for sequence generation in songbird zebra finch HVC, which includes all experimentally known facts about HVC organization. In particular, we model HVC as an ellipsoid with the spatial dimensions corresponding to the real HVC; use realistic number of HVC-RA and HVC-I neurons; make connections between HVC-RA and HVC-I neurons probabilistically, based on the distances between the neurons; and incorporate experimentally measured axonal conduction delays. We discover that if a synfire chain connectivity between HVC-RA neurons is assumed, it leads to a highly synchronous activity of HVC-RA neurons, which is not consistent with experimental observations. Incorporated axonal conduction delays between neurons do not make the activity smoother and introduce an additional problem of late inputs.

Based on that, we propose a different network topology, a polychronous network, which uses distributed axonal conduction delays to produce synchronous inputs to the network neurons. We develop a mechanistic algorithm that wires a polychronous network given a distribution of axonal conduction delays and spatial synaptic distribution. We find that polychronous networks created with experimental axonal delay distribution shows a continuous neuron activity, which agrees with experimental observations. We further simplify the model by getting rid of space and interneurons, and explore how the width of axonal delay distribution affects the continuity of polychronous network activity. Wide axonal delay distributions result in polychronous networks with continuous activity,

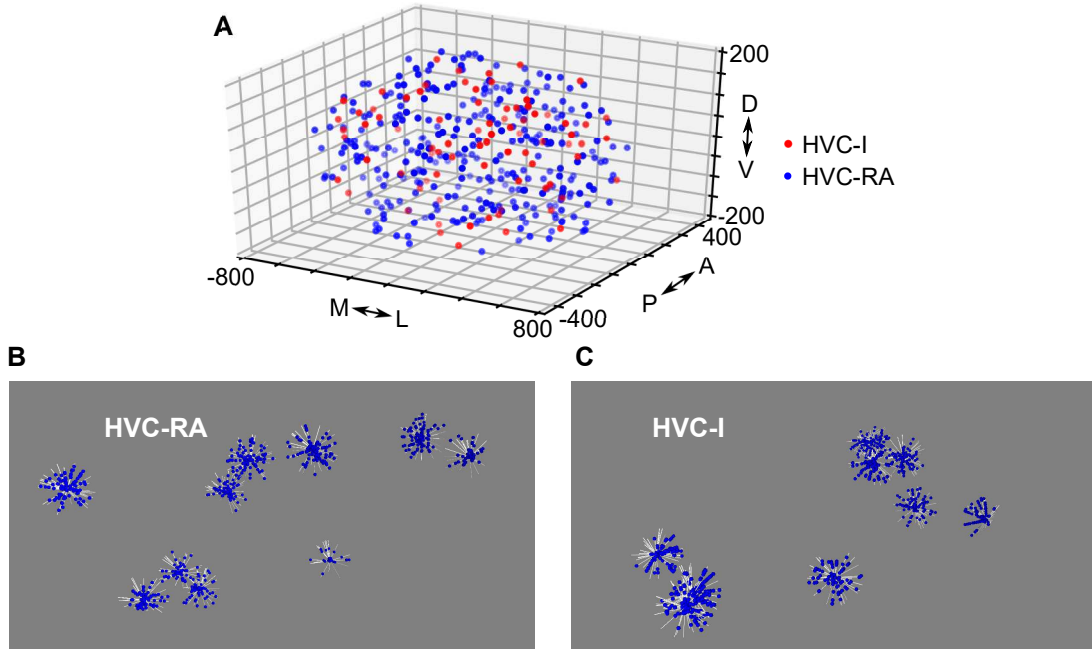


**Figure 3.1.** Neuronal spatial arrangement and dendritic tree. (A) 20,000 HVC-RA (red balls) and 5,500 HVC-I (blue balls) neurons are distributed randomly in ellipsoid with dimensions  $1607 \mu\text{m} \times 816 \mu\text{m} \times 454 \mu\text{m}$  without overlap (only 1.5% of neurons are shown). Dendritic trees of (B) HVC-RA and (C) HVC-I neurons are modeled as 45 branches with extent  $80 \mu\text{m}$  emanating from the somatas' center. Each figure (B) and (C) shows 10 examples of dendritic trees (white tubes) with blue balls representing synapses on the dendrites.

which covers the song almost uniformly. In contrast, narrow distributions produce synfire chains with synchronous activity.

### 3.1 Neuronal spatial arrangement

We start by setting up spatial distributions of neurons. HVC of an adult zebra finch on average contains 40,000 HVC-RA neurons and 10,000 HVC-X neurons [37]. However, only half of HVC-RA neurons are song-related. Since interneurons make up around 10% of the entire neuronal population in HVC [88], we estimate an average population of interneurons as 5,500 neurons. Ablation studies show that HVC-X neurons are unlikely to participate in the sequence generation of HVC-RA neurons, and we exclude them from the model (see Introduction for more details).

Neuronal somatas vary in diameter from  $7$  to  $10 \mu\text{m}$  for HVC-RA neurons [89], and from  $10 \mu\text{m}$  to  $20 \mu\text{m}$  for HVC-I neurons [51]. Based on that, we model somatas of HVC-RA and HVC-I neurons as solid spheres with diameter  $10 \mu\text{m}$ . Nucleus HVC has a

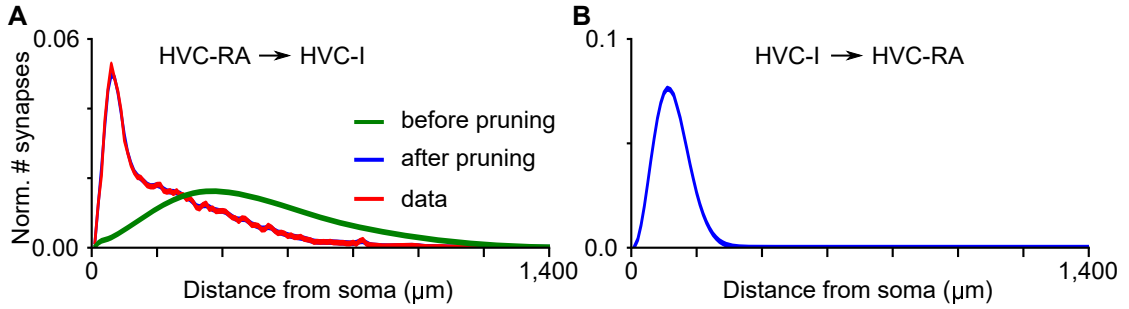


**Figure 3.2.** Connections between HVC-RA and HVC-I neurons. (A) Connections from HVC-RA to HVC-I neurons are created using a pruning procedure. First, each HVC-RA neuron is connected to all HVC-I neurons with the synapse placed on the nearest dendrite of postsynaptic HVC-I neuron relative to the soma of the presynaptic HVC-RA. Resulting spatial synaptic distribution (green) is biased toward long-distance connections. Next, connections are pruned in the synaptic distance-dependent manner (see text for details) and spatial synaptic distribution after pruning (blue) matches the experimental (red). (B) Connections from HVC-I to HVC-RA neurons are local and created probabilistically based on the distances between neuronal somatas (see text).

roughly ellipsoidal shape with average axial dimensions  $1600 \mu\text{m}$  (medial-lateral direction, or M-L)  $\times 800 \mu\text{m}$  (anterior-posterior or A-P)  $\times 450 \mu\text{m}$  (dorsal-ventral or D-V), based on the estimates for 30 adult zebra finches (by Robert Egger, private communication). Thus, we randomly distribute 20,000 HVC-RA and 5,500 HVC-I neurons inside a three-dimensional ellipsoid of axial dimensions  $1607 \mu\text{m} \times 816 \mu\text{m} \times 454 \mu\text{m}$  (see Fig. 3.1A). We do not allow overlap between somatas of the neurons. In other words, distance between the centers of neuronal cell bodies is larger or equal to  $10 \mu\text{m}$ .

## 3.2 Neuronal connectivity

Next, we set up connections between the neurons. To better approximate the experimental data, we place synapses on the dendrites of HVC-RA and HVC-I neurons. Recent studies have reconstructed the detailed morphology of the dendrite of HVC-RA neurons [50, 89]. Dendrite of an HVC-RA neuron has roughly spherical shape with diameter  $161 \mu\text{m}$  [89]. On average it has 5 primary branches with 9 nodes per primary branch (branching points). Based on that, we model a dendrite of an HVC-RA neuron as 45 branches with extent  $80 \mu\text{m}$  emanating in random directions from the soma (see Fig. 3.1B). The branches are cut at the ellipsoid boundaries to prevent them from going beyond the HVC structure. Dendrite of HVC-I neuron was not thoroughly characterized so far. Therefore, we model it in the same way as the dendrite of HVC-RA neuron (see Fig. 3.1C).

Average HVC-RA neuron makes 170 connections to other HVC-RA neurons [89], and 688 connections to HVC-I neurons [50]. In the same study, Kornfeld et al. have determined a spatial distribution of synapse locations along the axon and the axonal morphology of HVC-RA neurons [50]. With this information, our collaborators at NYU have evaluated the average spatial distribution of synapses from HVC-RA neurons onto other HVC-RA and HVC-I neurons relative to the soma of the presynaptic neuron. This allows us to create a similar spatial synaptic distributions in the model.

To make connections from HVC-RA to HVC-I neurons with the spatial synaptic distribution matching the experimental, we use a pruning approach. First, we oversample synapses by connecting each HVC-RA neuron randomly to the nearest dendrites of all HVC-I neurons. The connection strength is sampled randomly between 0 and  $G_{ei}$ , with  $G_{ei} = 0.15 \text{ mS/cm}^2$ . Next, we estimate a spatial distribution of HVC-RA  $\rightarrow$  HVC-I synapses relative to the soma of the presynaptic HVC-RA neuron with  $10 \mu\text{m}$  resolution. The distribution shows a strong bias toward distal connections and does not agree well with the experimental data (see Fig. 3.2A). Then, we prune connections in the network (i.e., the model distribution) to match the soma-synapse distance (later referred to as synapse distance) distribution derived from experimental observations (i.e., the target distribution). For pruning, we determine the mode bin of the target distribution  $i_{max}$ . To prevent HVC-RA neurons from making more connections than in the target distribution, we define a common downscale factor  $s$ , which is set to 1 if the  $model(i_{max}) < target(i_{max})$ , and to  $model(i_{max})/target(i_{max})$  otherwise (where  $model(i_{max})$  and  $target(i_{max})$  denote model and target distributions at bin  $i_{max}$ ). Then, for each bin  $i$  in the model and target distributions, we compute a down-scaling factor  $d(i)$ :

$$d(i) = s \frac{target(i) model(i_{max})}{target(i_{max}) model(i)}$$

Next, we normalize the scaling factors so that they do not exceed 1:  $d(i) = d(i) / \max_i d(i)$  and re-scale the target distribution:  $target(i) = d(i) target(i)$ . Finally, we randomly remove connections in proportion to the remaining difference between the model and target distributions. After pruning procedure, remaining synapses have the spatial distribution which agrees well with the experimental data (see Fig. 3.2A).

Much less is known about the connections of HVC-I neurons. Limited data is available only for local output connections of HVC-I neurons [90]. According to Koshe et al., HVC-I neurons on average contact 67% of HVC-RA neurons within  $100 \mu\text{m}$  distance from their soma.

Based on that, connections from HVC-I to HVC-RA neurons in the model are made randomly according to a radial probability distribution:  $p = \exp[-(d - 10.0)^2/\sigma^2]$ , where  $d$  is the distance between HVC-I and HVC-RA neuron somata in  $\mu\text{m}$ , and  $\sigma = 105 \mu\text{m}$  is determined such that the cumulative probability of finding a connection within  $100 \mu\text{m}$  is 0.67 as in [90]. If a connection from an HVC-I to an HVC-RA neuron is made, the corresponding synapse is placed randomly on one of the dendritic branches of HVC-RA neuron. The connection strength is sampled randomly between 0 and  $G_{ie}$ , with  $G_{ie} = 0.050 \text{ mS/cm}^2$ , unless stated otherwise. Established HVC-I  $\rightarrow$  HVC-RA connections (see Fig. 3.2B) are more local compared to connections from HVC-RA to HVC-I neurons.

### 3.3 Axonal conduction delays

In addition to the spatial synaptic distributions for efferent HVC-RA connections, our collaborators have also estimated the corresponding axonal conduction time delays. The delay distributions are long-tail with the shape similar to log-normal distribution (see Fig. 3.3C and Fig. 3.4F). The delays for local connections in HVC were not measured directly, but calculated used the procedure described below. Briefly, time propagation of signal between HVC and RA was recorded as the difference between the start of antidromic stimulation in RA and the action potential onset in HVC. Using the path length of the unmyelinated axons connecting HVC and RA, the axonal conduction velocity was estimated as the ratio between the path length and the signal propagation time. For local efferent connections of HVC-RA neurons, axonal conduction velocity was adjusted by taking into account the difference between cross-sectional areas of local and downstream axons. Finally, the axonal conduction delays were calculated by taking a product of axonal conduction velocity and the path length along the axon. Even though the delays were not measured directly, the resulting distributions provide a reasonable estimate, which we use in the modeling.

To assign the values of axonal conduction time delays for efferent HVC-RA connections in the model, we need to know how the delays change with the distance from the soma of presynaptic HVC-RA neurons. Because an axon of HVC-RA neurons is very irregular making many twists and turns on its way, it may travel different path length to reach the same distance relative to the soma. To account for that, we split the distances from soma into non-overlapping  $50 \mu\text{m}$  bin intervals and estimate axonal conduction delay distributions for each such interval (see Fig. 3.3A-B). As expected, synapses located

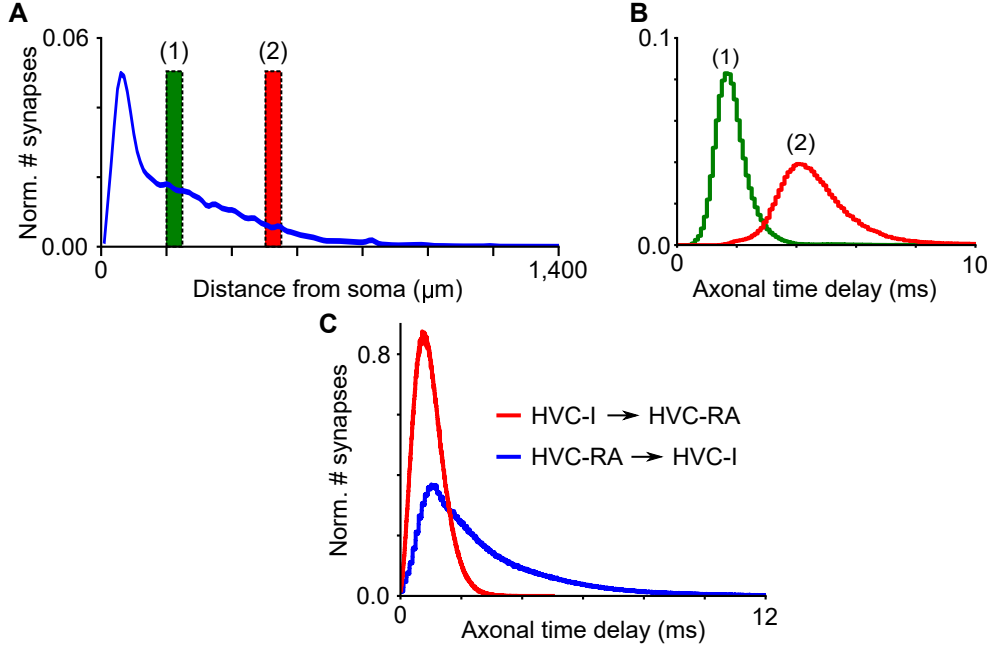


**Figure 3.3.** Axonal conduction delays between HVC-RA and HVC-I neurons. (A) Axonal conduction delays for HVC-RA to HVC-I connections are sampled based on the synaptic distances from the soma of the presynaptic HVC-RA. The distances are binned using  $50 \mu\text{m}$  resolution and a separate axonal conduction delay distribution is assigned for each bin, based on experimental data. (B) Two examples of axonal conduction delay distributions for bin  $200\text{--}250 \mu\text{m}$  (1) and bin  $500\text{--}550 \mu\text{m}$  (2). Synapses located at larger distances from the soma of presynaptic neuron tend to have longer axonal conduction delays. Delays for HVC-I to HVC-RA connections are sampled from Gaussian distribution with synaptic distance-dependent mean and variance, estimated by fitting delays for HVC-RA to HVC-I connections. (C) Overall axonal conduction delay distributions for HVC-I to HVC-RA connections (red) and for HVC-RA to HVC-I connections (blue).

further away from the presynaptic soma on average have longer axonal delays. However, the delay distributions have a large spread, which is created by the irregularities of the axons. To assign delay for each connection from HVC-RA to HVC-I neuron, we find the bin interval that corresponds to its synapse distance, and sample delay from the distribution for that bin. Resulting axonal delays (see Fig. 3.3C) have a long-tail distribution and range from 0 ms up to  $\sim 12$  ms.

Since there is currently not much data available on the axonal conduction time delays for HVC-I  $\rightarrow$  HVC-RA connections, we set them up using the data on delays for HVC-RA  $\rightarrow$  HVC-I connections. For a synapse from HVC-I onto HVC-RA neuron located at distance  $r \mu\text{m}$  from the soma of HVC-I neuron, we sample axonal conduction delay from a Gaussian distribution with distance-dependent mean  $\mu(r)$  and standard deviation  $\sigma(r)$ :  $\mu(r) = 0.0083 * r - 0.0463$  ms and  $\sigma(r) = 0.0017 * r + 0.0152$  ms. The coefficients in

these equations are constrained in two ways. First, the slopes of the two relationships are determined by fitting the axonal conduction time distributions for synapses from HVC-RA neurons onto HVC-I in  $50 \mu\text{m}$  intervals with Gaussian distributions. We then fit a linear relationship to the mean and standard deviation of these Gaussian distributions. Second, to determine the intercept of the two functions, we require that at a distance of  $50 \mu\text{m}$ , the delays should be  $0.37 \pm 0.10 \text{ ms}$ , consistent with [90]. Resulting axonal delays (see Fig. 3.3C, red) are much smaller than the delays for HVC-RA to HVC-I connections, emphasizing a local range of inhibitory connections.

## 3.4 Neuron model and simulations

For HVC-I neurons, we use the model identical to the one described in Chapter 2. For HVC-RA neurons, we use a model similar to the one described in Chapter 2 with the following differences:  $R_C = 130 \text{ M}\Omega$ ,  $G_{s,L} = 0.05 \text{ mS/cm}^2$ ,  $\tau_c = 15 \text{ ms}$ . The changes are introduced to better match the observed  $\sim 5 \text{ ms}$  integration time of HVC-RA neurons during singing [66]. Dynamics of HVC-I neurons is simulated with Dormand-Prince 8th order numerical method and dynamics of HVC-RA neurons with AN3D1 3rd weak order method with time resolution  $0.02 \text{ ms}$  (see Chapter 2 for more details). HVC-RA neurons receive white noise injections with amplitude  $0.1 \text{ nA}$  to soma compartment and amplitude  $0.2 \text{ nA}$  to dendrite (which produces somatic membrane potential fluctuations  $\sim 4 \text{ mV}$ ), unless otherwise stated. HVC-I neurons receive noise via Poisson spike trains with parameters identical to Chapter 2 and spike spontaneously with frequency  $\sim 10 \text{ Hz}$ .

## 3.5 Pruned synfire chain

### 3.5.1 Pruned chain construction

We start the analysis of HVC microcircuit dynamics by testing one of the most popular models for precise temporal sequences - a synfire chain. We assemble a synfire chain by randomly assigning neurons to 117 groups with 170 neurons per group. The assignment is performed without replacement, so that each neuron is assigned to a single unique group. Random assignment of neurons to groups is motivated by the observations that activity in HVC does not have any obvious spatio-temporal pattern. Thus, our synfire chain produces random spatio-temporal activity by the network construction. Next, we connect the groups sequentially by making all-to-all connections from the neurons in

one group to the neurons in the next group (see Fig. 3.4A). The connections are placed randomly on the nearest dendrite of the postsynaptic neuron relative to the soma of the presynaptic neuron. The connection strength is sampled randomly between 0 and  $G_{ee}$ , with  $G_{ee} = 0.050 \text{ mS/cm}^2$ , unless otherwise stated. Last synfire chain group does not send output connections. Overall, the synfire chain contains  $117 \times 170 = 19890$  neurons, and the remaining 110 neurons are left unconnected.

Since during the synfire chain construction we assign neurons randomly to the groups, spatial distribution for HVC-RA  $\rightarrow$  HVC-RA connections does not agree with the experimental distribution (see Fig. 3.4C). It is biased towards distal connections, similarly to the HVC-RA  $\rightarrow$  HVC-I connections before pruning. Corresponding axonal conduction delay distribution is also shifted right, resulting in longer delays than observed in the experiment (see Fig. 3.4E). To obtain spatial and axonal conduction delays as in the experiment, we use a pruning procedure similar to the one described above for HVC-RA  $\rightarrow$  HVC-I connections. After pruning, the spatial distribution is in a good agreement with the experimental one (see Fig. 3.4D). Pruning procedure automatically guarantees that axonal delay distribution matches the data (see Fig. 3.4F), since delays are sampled based on synapse distances.

Since pruning procedure removes some of the connections, neurons in synfire chain no longer make all-to-all connections to the neurons in the next group, i.e., synfire chain is not perfect (see Fig. 3.4B). We refer to such synfire chain as a *pruned chain*. On average, each neuron in the pruned chain makes 45 connections. The estimated probability for a neuron in one group to connect a neuron in the next group is  $\sim 0.26$ . The difference between the number of connections in the pruned chain and the number of connections in the experiment can be explained by synaptic multiplicity. Morphological reconstructions show that in the cortex, often several synaptic connections are found between presynaptic axons and postsynaptic dendrites of connected neurons [91–93]. For instance, in the barrel cortex, the average number of synapses per connection, i.e., synaptic multiplicity, is estimated to be around 10 [94]. Synaptic multiplicity in the pruned chain is  $1/0.26 \approx 3.8$ . Up to date, synaptic multiplicity for neurons in HVC has not been estimated.

In addition to the decreased number of output connections, HVC-RA neurons in the pruned chain have inhomogeneous number of input and output synapses. While all neurons in the perfect synfire chain (excluding first and last layers) send and receive 170 connections (see Fig. 3.4G), neurons in the pruned chain have smaller and distributed number of inputs and outputs (see Fig. 3.4H). But what is the source of this variability in the number of connections?

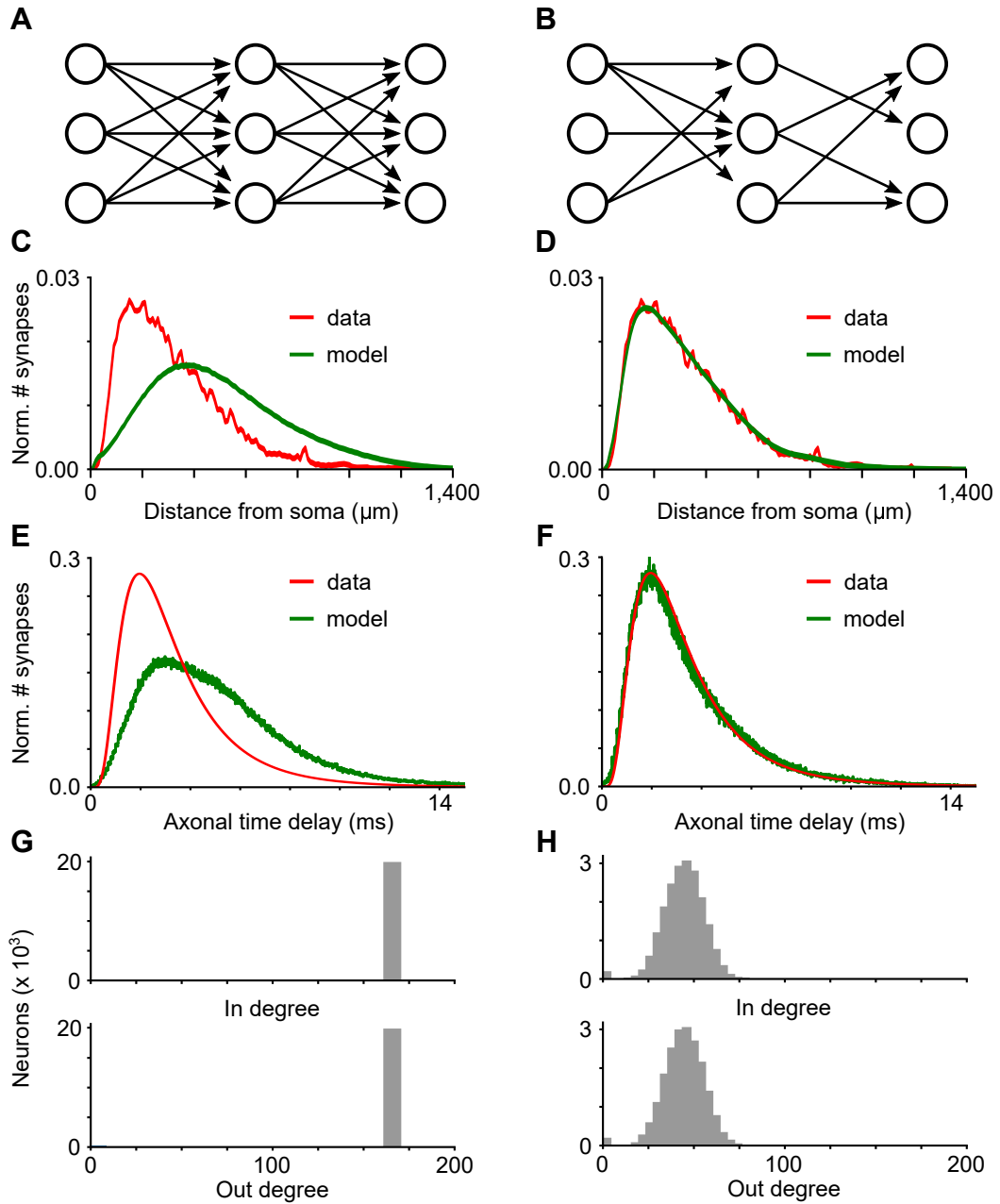


**Figure 3.4.** Comparison of synfire chain before and after pruning. Schematic of network connectivity for perfect synfire chain (A) and pruned synfire chain (B). Synaptic spatial distribution for perfect synfire chain (C, green) shows a bias toward long distance connections, while the distribution for pruned synfire chain (D, green) matches the experimental one (red). Corresponding axonal conduction delay distributions for perfect synfire chain (E) and pruned synfire chain (F). In and out degree distributions for pruned chain (H) show variance and are shifted left to smaller values compared to the distributions for perfect synfire chain.

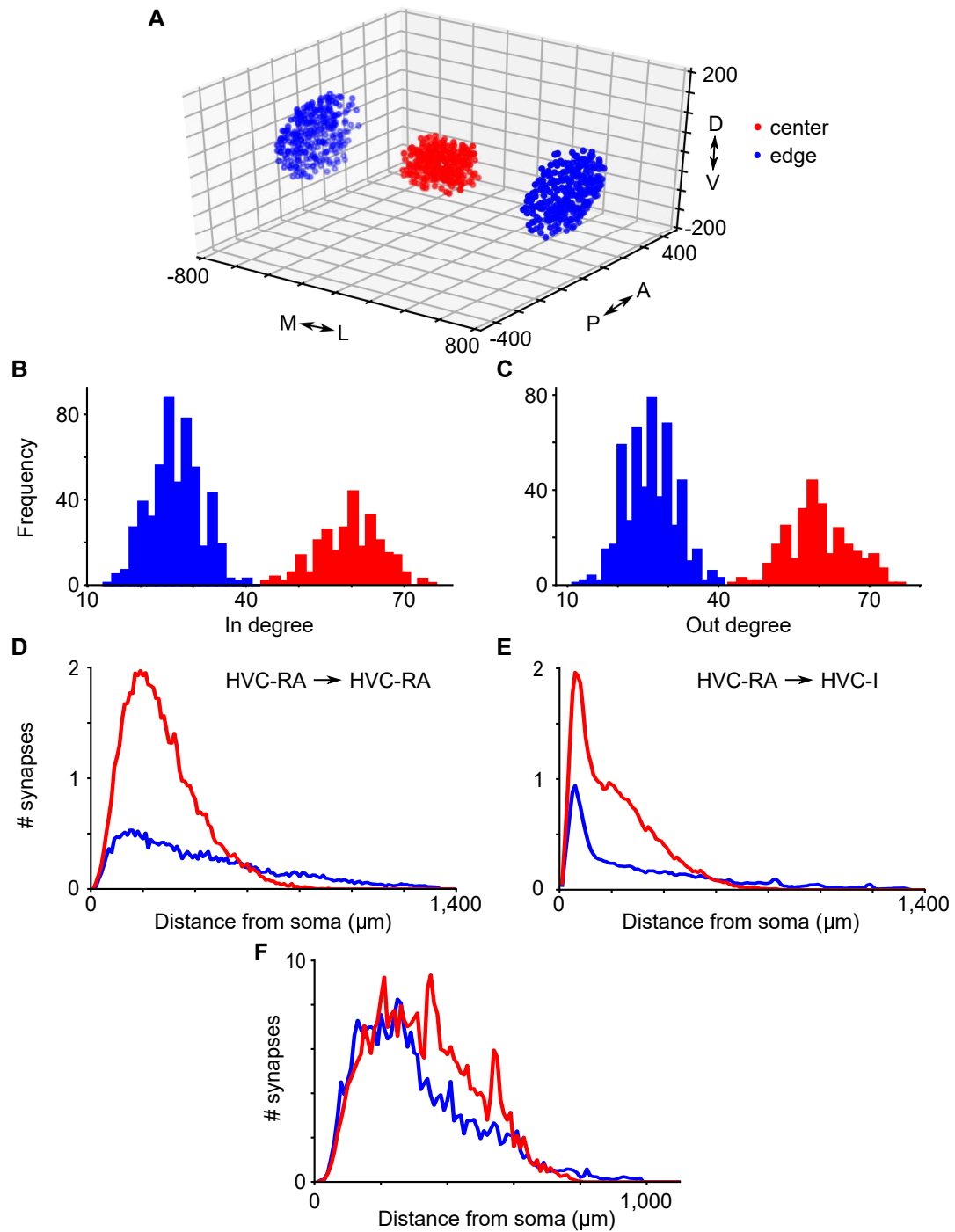


**Figure 3.5.** Comparison of edge and center neurons. (A) 3-D picture showing location of edge (with absolute value of M-L coordinate  $> 700 \mu\text{m}$ , blue balls) and center neurons (with absolute values of coordinates M-L  $< 150 \mu\text{m}$ , A-P coordinates  $< 75 \mu\text{m}$  and D-V coordinates  $< 50 \mu\text{m}$ , red balls). Edge neurons have smaller in degree (B) and out degree (C) compared to center neurons. Center neurons send more outputs to other HVC-RA neurons (D) and to HVC-I neurons, and the outputs are more local. In the experimental data (F), there is some evidence that edge neurons make less outputs and they are more distal.

Interestingly, the pruning procedure introduces bias for the edge HVC-RA neurons, i.e. the neurons near the boundaries of HVC (defined as the neurons with absolute value of M-L coordinate  $> 700 \mu\text{m}$ , see Fig. 3.5A). Compared to the HVC-RA neurons near the center of HVC (defined as the neurons with absolute values of M-L coordinate  $< 150 \mu\text{m}$ , A-P  $< 75 \mu\text{m}$ , and D-V  $< 50 \mu\text{m}$ ), edge neurons receive smaller number of inputs (see Fig. 3.5B), send less number of outputs (see Fig. 3.5C), and make contacts with more distal HVC-RA neurons (see Fig. 3.5D). Similar trend is also observed for connections from HVC-RA neurons to HVC-I neurons (see Fig. 3.5E). Such connectivity bias of edge neurons is caused by the geometry of HVC. Indeed, the edge neurons are located far from the majority of other HVC-RA and HVC-I neurons. Therefore, if they contact other neurons, the corresponding connections tend to be long. In contrast, HVC-RA neurons at the center of HVC are located relatively close to other HVC-RA and HVC-I neurons. They are not able to send long connections. Instead, they establish numerous local connections. Thus, the pruning procedure, which is applied to the average spatial distribution of synapses, targets edge neurons more aggressively and removes more of their inputs and outputs. Moreover, the pruning is not able to match the individual distributions for single neurons. We observe similar trends in spatial synaptic distributions for edge and center neurons in the data provided by our collaborators (see Fig. 3.5F). Edge neurons have less number of connections and they are more distal, while center neurons send more connections, but they are more local. Thus, the bias created by our pruning procedure agrees with the experimental data.

### 3.5.2 Burst onset density oscillations in pruned chain

To generate activity in the pruned chain, we excite the first synfire chain group by a strong synchronous conductance pulse of 300 nS. Dynamics of HVC-RA neurons in the pruned chain contains synchronously spiking synfire groups as revealed by the spike raster plot (see Fig. 3.6A). Interneurons produce dense spike patterns with occasional gaps in activity (see Fig. 3.6B), similar to observations in [90]. We define a burst of HVC-RA neurons as a continuous groups of spikes with interspike intervals less than 30 ms. Burst onset time is then defined as the first spike in the burst. Analysis of the HVC-RA burst onset times reveals prominent oscillations and silent gaps in activity between synchronous bursts of adjacent synfire groups (see Fig. 3.6C). Spectral power analysis of burst onset density confirms the presence of a strong oscillation at around 150 Hz. (see Fig. 3.6D).

HVC-RA neurons control timing in the song. Thus, the presence of silent intervals in

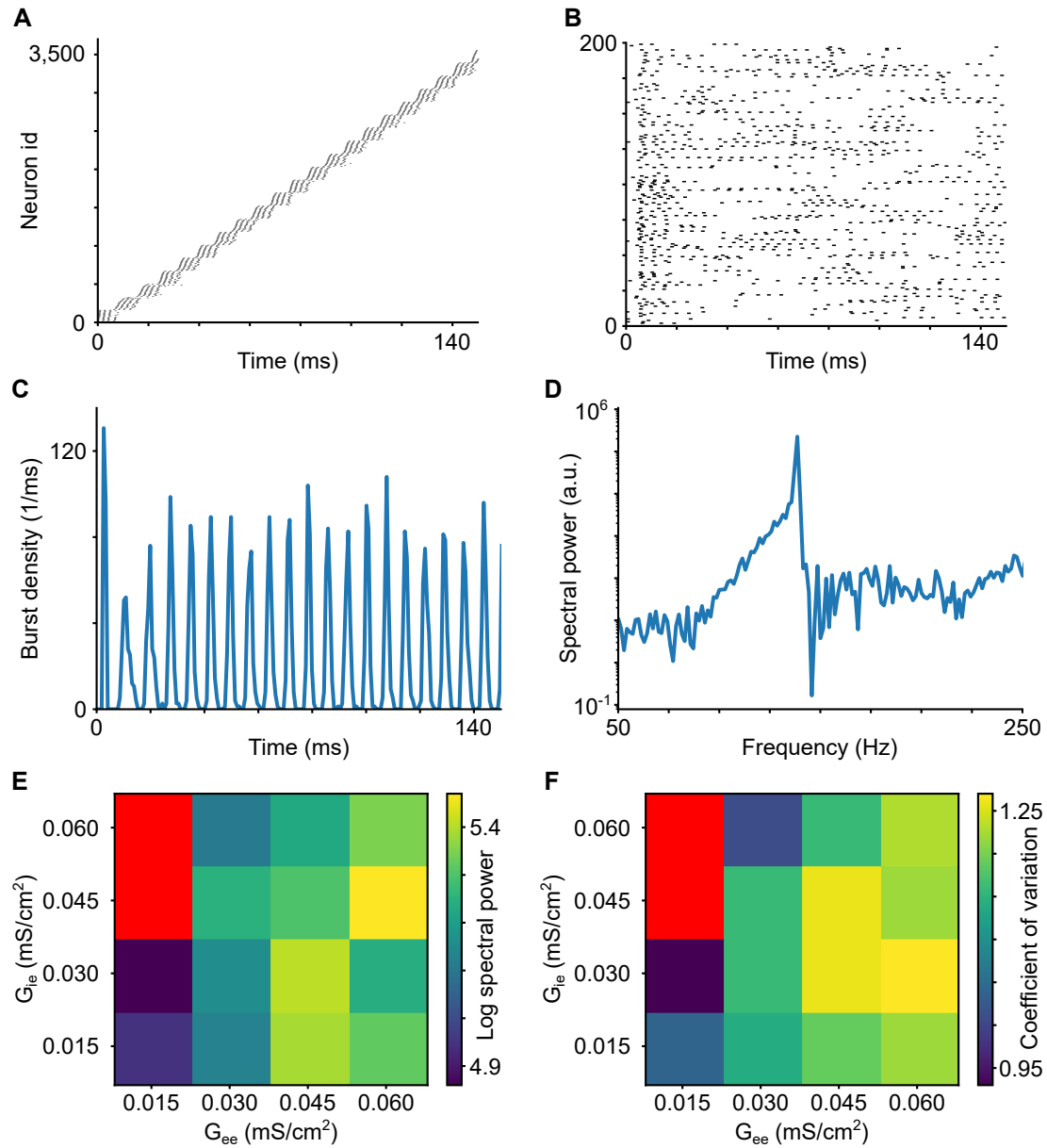


**Figure 3.6.** Pruned synfire chain shows prominent oscillations. (A-D) Pruned synfire chain with  $G_{ie} = G_{ee} = 0.050 mS/cm^2$ . (A) Spike raster plots of the first 150 ms of HVC-RA (A, only 10% of neurons shown) and HVC-I (B, 200 interneuron shown) neuronal dynamics. HVC-I activity demonstrates occasional gaps in interneuron spiking, similar to [90]. (C) Burst onset density reveals synchronous activity in synfire groups. (D) Spectral power analysis shows a prominent oscillation at  $\sim 150$  Hz. Dynamics of pruned synfire chain contains significant oscillations revealed by spectral power (E) and coefficient of variation of burst density (F) for different strengths of inhibitory (vertical axes) and excitatory connections (horizontal axes). Red squares represent regions where no signal propagation is observed.

the burst activity of HVC-RA neurons limits the flexibility of the song control system, since no motor command can be encoded during the silence. This makes a pruned synfire chain less advantageous model as a sequence generator in HVC. Moreover, recent experimental study shows that the burst activity of HVC-RA neurons in adult zebra finch during singing does not contain significant oscillations [87]. This makes the pruned synfire chain model, which generates prominent oscillations in burst density, inconsistent with experimental observations.

We next wonder if oscillations in the burst activity of HVC-RA neurons can be smoothed by adjusting the excitatory weights between HVC-RA, or inhibitory weights from HVC-I to HVC-RA neurons. Intuitively, since neurons in the pruned chain differ in the number of input and output connections, they receive different excitation and inhibition, which spreads out burst onset times in synfire groups. This may cause burst onset times in adjacent synfire groups to overlap and create a continuous smooth sequence. To address the question, we systematically vary the strength of excitation and inhibition in pruned synfire chain. We find that oscillations in neural activity of pruned chain could not be significantly smoothed by adjusting the strength of excitatory and/or inhibitory connections. Both the spectral power analysis (see Fig. 3.6E) and the analysis of the coefficient of variation of burst onset density (defined as standard deviation of burst onset density divided by the mean, see Fig. 3.6F) do not reveal big changes in oscillation prominence. The oscillations are most suppressed in the limit of weak excitation and strong inhibition, since it results in the largest spread of burst onset times in synfire groups.

According to experimental recordings, HVC-RA neurons produce precise bursts of activity. Typical precision of an HVC-RA neuron is in a sub-millisecond range. In the model, we characterize neuronal precision as a standard deviation in burst onset times (i.e., jitter) computed over 20 runs of the network dynamics. For sufficiently strong excitation, the pruned chain generates precise bursting times of HVC-RA neurons with jitter similar to the one observed experimentally (see Fig. 3.7A). Pruned chains with weak excitation and strong inhibition demonstrate large jitter (see Fig. 3.7B), which is not consistent with the data. Therefore, pruned synfire chains with weights adjusted to produce smoother activity are not precise. These observations again suggest that the burst activity of the pruned synfire chain cannot be smoothed by adjusting the strength of synaptic weights.

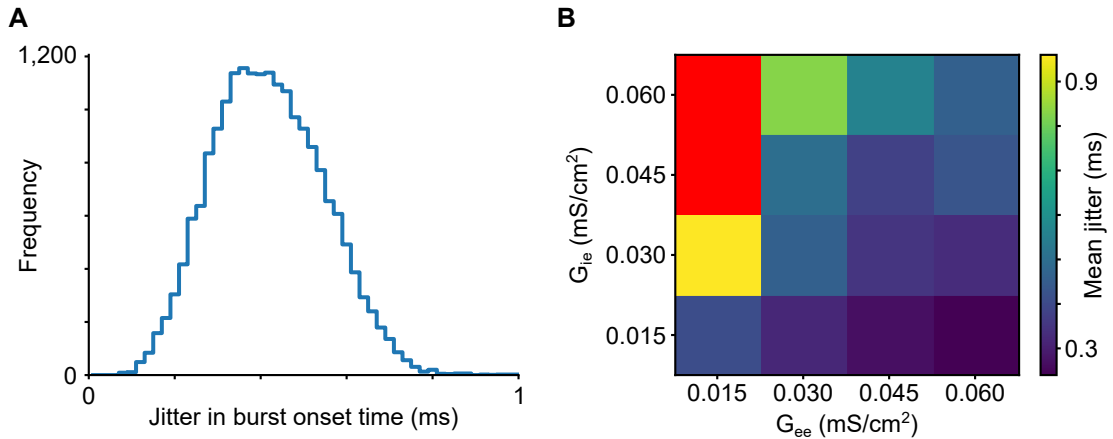


**Figure 3.7.** Precision in pruned synfire chain. (A) Histogram of jitter in burst onset times of HVC-RA neurons in pruned chain with  $G_{ie} = G_{ee} = 0.050 \text{ mS/cm}^2$  based on dynamics of 20 test runs. All neurons demonstrate sub-millisecond precision. (B) Phase diagram of mean jitter for different strengths of inhibitory and excitatory connections. Red squares represent regions where no signal propagation is observed. Jitter is low for strong excitation and weak inhibition.

### 3.5.3 Late inputs in pruned chain

We first thought that distributed axonal conduction delays would help to spread out the burst times of neurons in synfire groups. However, it is not the case, as illustrated by our analysis above. Indeed, since neurons receive multiple convergent connections with different axonal delay values from the neurons in the previous synfire group, it effectively acts as a single excitatory input with the average axonal delay. When this input is transferred from one synfire group to another, neuronal response is additionally delayed by the average axonal delay time. Therefore, the presence of axonal delays does not produce a smoother neural activity, and instead enhances the silent intervals in neural activity.

But what if excitatory connection strength is so large that neurons integrate almost instantaneously and connections with the smallest delays are driving the activity? Would it be possible to bring burst times of adjacent synfire groups so close together that they almost overlap and create a continuous sequence? We argue that this is unlikely. First, the integration time of HVC-RA neurons during singing was estimated experimentally to be  $\sim 5 \text{ ms}$  [66]. Second, fast integration time produces another problem of some inputs arriving after the burst onset time of postsynaptic neurons, i.e., late inputs. Here we define an *input time* as a presynaptic burst onset arrival time relative to a postsynaptic burst onset time (see Fig. 3.8A). We observe significant amount of late inputs in our simulations of pruned chain even at the moderate level of excitation (see

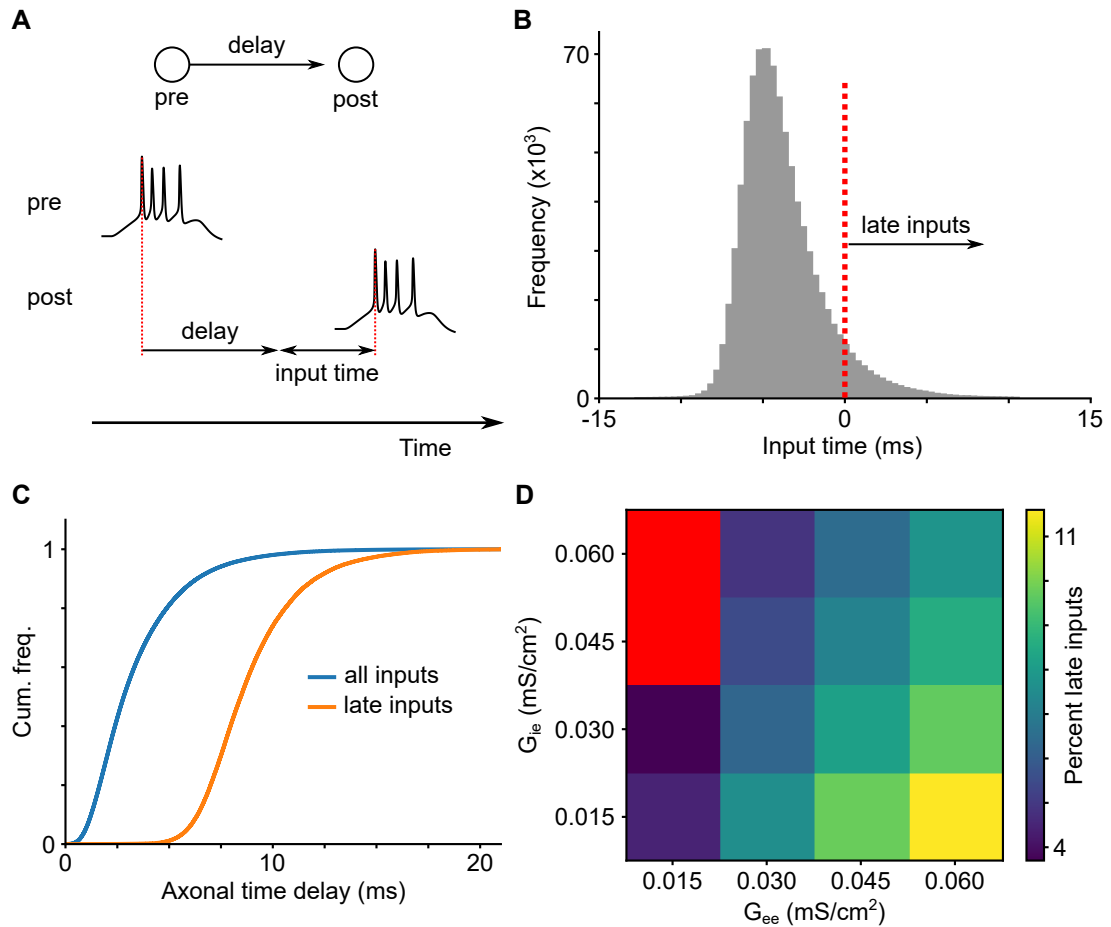


**Figure 3.8.** Late inputs in pruned synfire chain. (A) Input time for an HVC-RA neuron is defined as a presynaptic burst onset arrival time relative to a postsynaptic burst onset time. (B-C) Analysis of input times in pruned chain with  $G_{ie} = G_{ee} = 0.050 \text{ mS/cm}^2$ . (B) Input time histogram for a single test run. Inputs that arrive after the postsynaptic burst onset time are defined as late inputs, since they do not influence spiking of a postsynaptic neuron. (C) Axonal time delays for connections corresponding to all inputs (blue) and late inputs (orange). Late inputs show significantly longer axonal delays. (D) Phase diagram of percent of late inputs for different strengths of inhibitory and excitatory connections. Red squares represent regions where no signal propagation is observed. Fraction of late inputs is high for strong excitation and weak inhibition, and remains significant across the entire phase diagram.

Fig. 3.8B). Late inputs are unavoidable in synfire chains with synchronous activity in synfire groups. Indeed, if neurons in one group fire synchronously but connect to the next group with distributed axonal conduction delays, neurons in this next group do not receive synchronous input. Following this argument, the late inputs should correspond to input connections with long axonal conduction delays, which is exactly what we observe (see Fig. 3.8C).

The amount of late inputs in the pruned synfire chain depends on the strength of

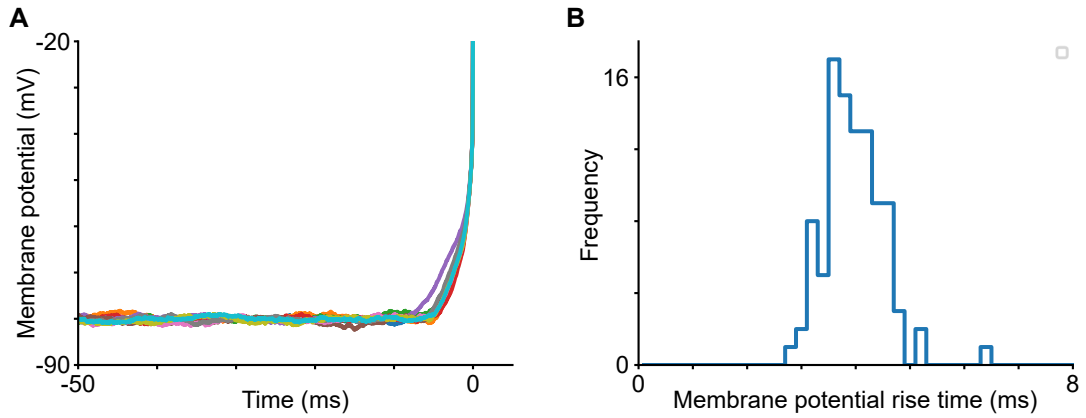


**Figure 3.9.** Membrane potential rise time for pruned synfire chain with  $G_{ie} = G_{ee} = 0.050 \text{ mS/cm}^2$ . (A) Average membrane potential traces of 10 neurons before burst onset, based on 25 test runs of the network dynamics. A membrane potential rise time is defined as the distance from the burst onset time to the first time when the membrane potential exceeds 5 standard deviations of the baseline (estimated in 100 ms time window, starting 20 ms before the burst onset time) (B) Histogram of membrane potential rise times shows a peak at  $\sim 4$  ms.

excitation and inhibition. It is easy to understand if we think in terms of neuronal integration times. If excitation is weak or if inhibition is strong, a neuron has to integrate many inputs before it produces a burst. Thus, its integration time becomes longer and almost all inputs can arrive before the burst onset of postsynaptic neurons, i.e., be on time. In our case, the distribution of axonal conduction delays has a long tail, therefore even in the limit of weak excitation and strong inhibition there is still a considerable amount of late inputs (see Fig. 3.8D).

Late inputs are not useful because they are not driving postsynaptic neurons, and they are also not biologically plausible. A classical Hebbian synaptic plasticity rule dictates that synapses corresponding to late inputs should be weakened and eventually pruned away. Therefore, it is unlikely that there is a significant fraction of late inputs in HVC. This, together with a 5 ms estimate of HVC-RA integration time, rules out a possibility of exceptionally strong excitatory connections that create smooth burst activity of HVC-RA neurons.

### 3.5.4 Membrane potential rise time

It is a challenge to experimentally measure input times to neurons. Instead, Long et al. [66] recorded membrane potential traces of HVC-RA neurons during singing and estimated a membrane potential rise time before the onset of the burst. The obtained rise times are  $\sim 5$  ms. We wonder if HVC-RA neurons in our pruned chain have similar

membrane potential rise time. To estimate the membrane potential rise time, we track membrane potentials of 100 randomly selected HVC-RA neurons for 25 testing runs of the pruned chain with moderate inhibition and excitation (see Fig. 3.9A-B). For each neuron we compute an average membrane potential relative to the burst onset time. Fig. 3.9A shows average membrane potential traces of 10 HVC-RA neurons. Next, we estimate the baseline membrane potential before the burst by calculating the mean voltage in 100 ms time window starting 20 ms prior to the burst onset time. Membrane potential rise time is defined as the distance from the burst onset time to the first time when membrane potential exceeds 5 standard deviations from the baseline. Resulting membrane rise time for simulation with  $G_{ie} = 0.05 \text{ mS/cm}^2$  and  $G_{ee} = 0.05 \text{ mS/cm}^2$  is  $4.0 \pm 1.0 \text{ ms}$ , which consistent with experimental observations. Therefore, HVC-RA neurons in our simulations have reasonable integration times, which suggests that our modeling results are relevant to the real songbird HVC.

Based on the results of our simulations, we conclude that pruned synfire chain model, which satisfies all experimentally known constrains of songbird HVC, produces prominent oscillations in neural activity, which is inconsistent with experimental observations. The oscillations arise due to the synchronous spiking of neurons in synfire groups. This synchronous spiking of synfire chains is, in fact, promoting the network resilience to the changes in parameters and noise, and is a well-known property of synfire chains [69]. Moreover, due to widely distributed axonal delays, the amount of un-biological late inputs is large, which motivates the search for another network topology.

### 3.6 Parallel pruned synfire chains

Dynamics of single synfire chain contains significant silent gaps due to axonal conduction delays and finite neuronal integration times. Thus, a logical way to smooth the dynamics is to somehow fill these silent gaps. A natural extension of a single synfire chain is a model with multiple parallel synfire chains. The idea is that due to variations in axonal conduction delays and neuronal integration times, neural activity in different synfire chains will have silent gaps of different size. The misalignment of the silent gaps of different synfire chains may produce a smooth neural activity of the entire network. We refer to this model as *parallel pruned synfire chains*.

To test this idea, we embed multiple synfire chains with smaller group width. To create parallel pruned synfire chains, we first sample independent perfect synfire chains (with each neuron only participating in one synfire chain). Then, we prune each perfect synfire

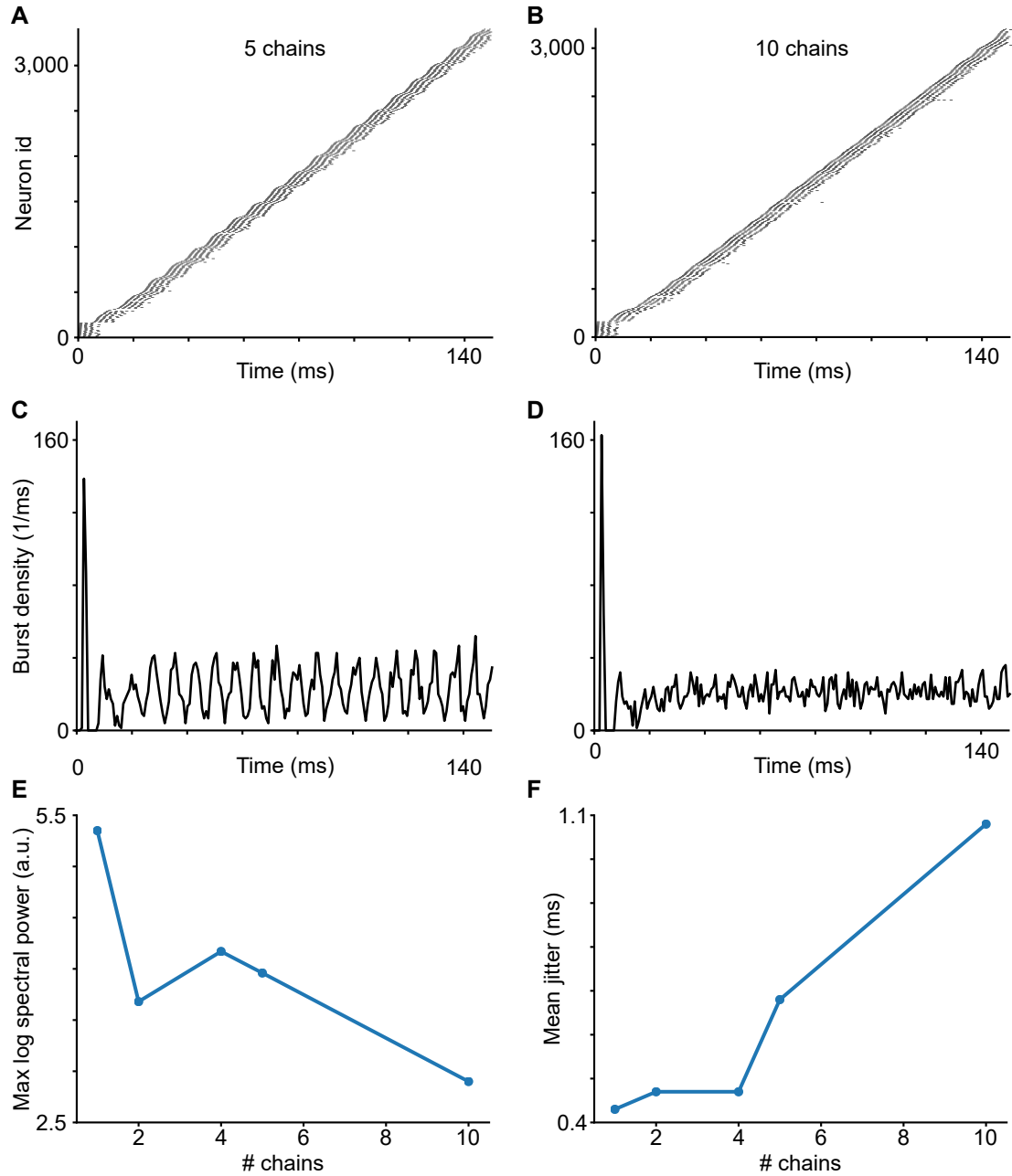


**Figure 3.10.** Parallel pruned synfire chains. Spike raster plots of the first 150 ms of HVC-RA dynamics (only 10% of neurons shown) in the network with 5 (A) and 10 (B) parallel pruned synfire chains. Corresponding burst onset density graphs show noticeable oscillation in dynamics of 5 parallel pruned synfire chains (C), and smooth dynamics for 10 chains (D). (E) Cumulative graph showing maximal log of spectral power between 50 and 250 Hz for different number of parallel synfire chains. (F) Precision in burst onset times of HVC-RA neurons for different number of parallel synfire chains. The jitter of the network with 10 parallel chains is higher than experimentally observed sub-millisecond precision.

chain to match the experimental spatial synaptic distribution for HVC-RA connections. Since the group width of individual chains is smaller compared to the case of a single pruned chain, the excitatory connections have to be scaled up to ensure the signal propagation. We maintain the average strength of excitatory input by keeping the product  $w * G_{ee}$  constant, where  $w$  is the width of individual pruned chain,  $G_{ee}$  is the maximal strength of excitatory connections between HVC-RA neurons. Five different network configurations are tested: 1 chain (width = 170), 2 chains (width = 85), 3 chains (width = 42), 5 chains (width = 34) and 10 chains (width = 17).

To generate activity in parallel pruned synfire chains, we excite the first synfire chain group of each chain by a strong synchronous conductance pulse of 300 nS. All chains are ignited at the same time. Incorporation of a small number of parallel chains (up to 5) does not completely erase the oscillations, which are still visible in spike raster plots and burst onset density histograms (see Fig. 3.10A,C). However, the amplitude of oscillations is significantly reduced as revealed by spectral power analysis (see Fig. 3.10E). Upon further increasing the number of parallel chains to 10, the activity becomes smooth and oscillations are no longer distinguishable (see Fig. 3.10B,D,E). Therefore, incorporation of a large enough number of parallel pruned synfire chains can produce smooth neural dynamics.

This, however, comes at a cost. Since the overall number of HVC-RA neurons in the network is kept the same, the increase in the number of parallel chains leads to a smaller synfire group width. Neurons receive less inputs and outputs, and the variability in input strength goes up. As a result, networks with many parallel synfire chains demonstrate poor precision of the burst onset times (see Fig. 3.10F). The network with 10 parallel chains that has a smooth dynamics with no oscillations, shows  $1.1 \pm 0.5$  ms jitter in burst onset times, which exceeds the experimentally observed sub-millisecond jitter level. Therefore, while parallel pruned synfire chains produce smooth neural dynamics and satisfy all experimentally known HVC constraints, they have a disadvantage of being imprecise.

It is important to note that in our simulations, parallel chains are ignited at the same time by externally provided excitation. The most likely source of the external input to HVC at the syllable onset times is the thalamic nucleus Uvaeformis (Uva). Multiunit neural activity in Uva shows a single  $\sim 10$  ms wide peak shortly before the syllable onset times [95]. Therefore, it is unlikely that parallel chains, if exist, are ignited at different times, which can potentially decrease the number of parallel chains needed to smooth dynamics and achieve a reasonable jitter level. In addition, as in the case of a

single pruned chain, there is still a problem of a significant amount of non-functional late inputs.

## 3.7 Polychronous network

In synfire chain with distributed axonal conduction delays, synchronous activity is converted to asynchronous inputs, which leads to some inputs arriving late. Motivated by this issue, we create a network where all inputs arrive synchronously and efficiently drive the postsynaptic neuron to fire. The network with such property is called a polychronous network (see [73] and Introduction).

### 3.7.1 Mechanistic wiring algorithm

To the best of our knowledge, there is no algorithm available that is able to wire long polychronous sequences. Izhikevich [73] showed that short polychronous sequences (with average length  $\sim 70$  ms and size 50 neurons) can self-assemble via Hebbian synaptic plasticity in the balanced networks of randomly spiking neurons. However, these sequences were short and unstable that prevents their use in practice. Therefore, we develop our own mechanistic algorithm which allows to wire a long polychronous sequence with given spatial synaptic and axonal delay distributions (see Fig. 3.11A).

The algorithm is iterative and starts with selection of  $N_{start}$  neurons ('starter neurons'), that form a starting seed for the network growth. Wiring iterations are run until all 20,000 HVC-RA neurons are incorporated into the network.

Each iteration of the wiring algorithm consists of two main and one optional steps. In the first step (i) (see Fig. 3.11B), network dynamics is simulated and burst onset times of all neurons that produced bursts are recorded. Network dynamics simulation is performed by exciting the starter neurons by a synchronous excitatory kick delivered at time 50 ms. To save computational time, the dynamics is simulated until time  $t_{sim} = t_{last} + 20$  (ms), where  $t_{last}$  - is the largest burst onset time of any neuron in the previous iteration. For the first iteration of the algorithm, dynamics is simulated until time  $t_{sim} = 70$  ms.

In the second step (ii) (see Fig. 3.11C), feedforward connections are added between 'source neurons' (presynaptic neurons) and 'target neurons' (potential postsynaptic partners, defined as neurons that receive at least one input and are not among 'source neurons'). The step starts by moving  $N_{new\ source}$  neurons from the set of 'target neurons' to the set of 'source neurons'. These  $N_{new\ source}$  neurons are selected as 'target neurons'

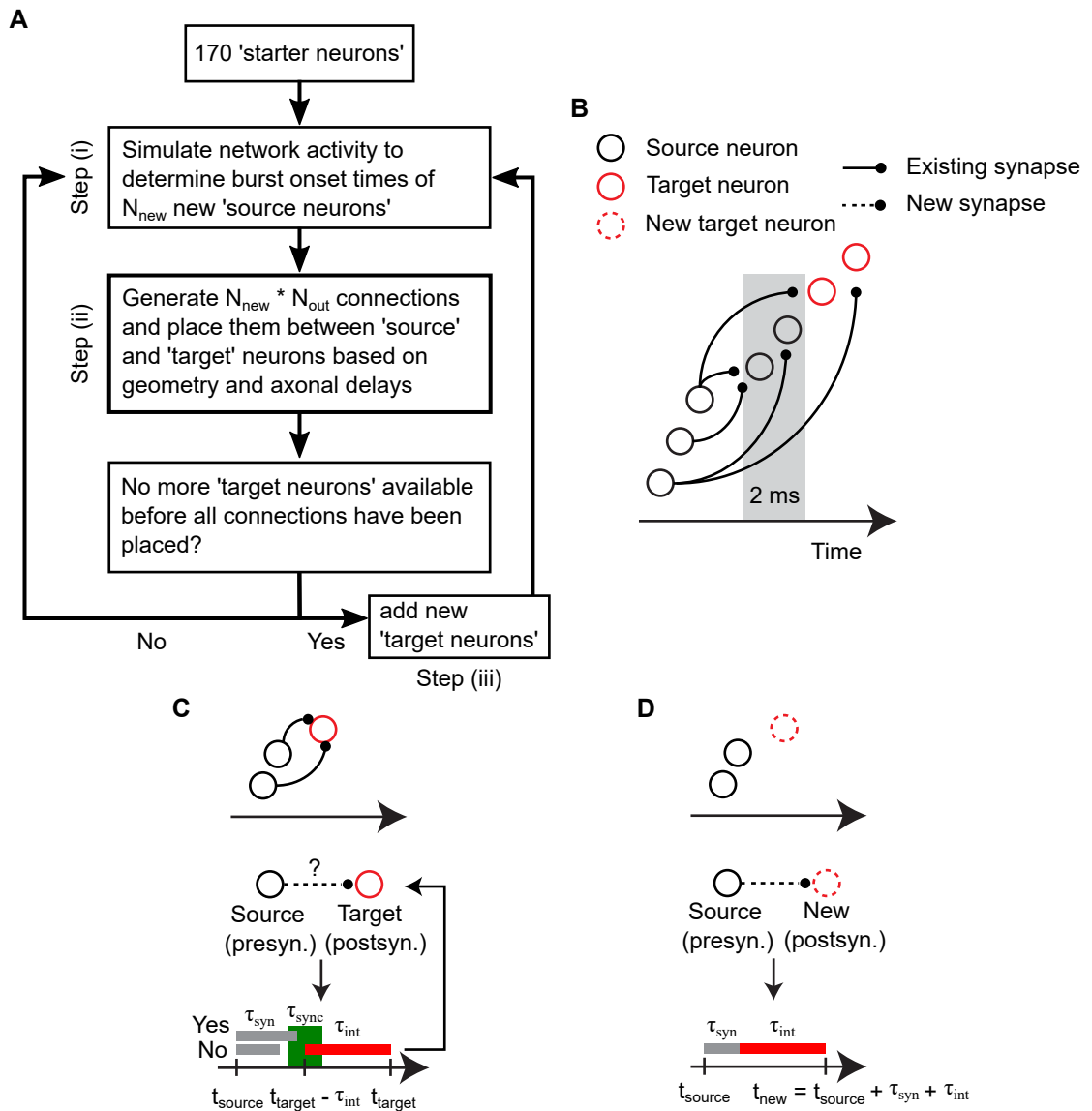


**Figure 3.11.** Mechanistic algorithm for wiring a polychronous network. (A) Schematic of the algorithm. (B) Step (i). After network dynamics is simulated, burst onset times of network neurons are determined. New source neurons are selected from the set of target neurons (i.e., neurons that don't have output connections) with burst onset times within 2 ms time window from the earliest burst onset time of all target neurons. (C) Step (ii). (Top) Connections are made between source and target neurons respecting spatial synaptic distribution and polychronicity principle. (Middle and Bottom): Connection can only be established if input (grey bar) arrives within a window of size  $\tau_{sync}$  relative to the putative burst onset time of the target neuron adjusted by its integration time. (D) Step (iii) (Top) New target neuron is sampled to the network. (Middle and Bottom) The putative target burst onset time is determined by the burst onset time of the presynaptic source neuron, axonal delay, and integration time.

with burst onset times within 2 ms window from the earliest burst onset time of all 'target neurons' (see Fig. 3.11B). Next, a synaptic pool of  $N_{new\ source} * N_{out}$  connections is generated, where  $N_{out}$  is the average number of output connections per neuron. Each connection in the pool is a triple of synaptic distance from the presynaptic soma, axonal delay and synaptic weight:  $(l_{syn}, \tau_{syn}, w_{syn})$ . The pool is created by first sampling from a synaptic spatial distribution for HVC-RA to HVC-RA connections, and then sampling axonal conduction delays based on the obtained synaptic distances. Synaptic weight is sampled randomly between 0 and  $G_{ee}$ . Next, the algorithm iterates over 'target neurons' sorted according to their number of input connections, starting from the smallest. Such iteration order makes the input convergence more even and helps to achieve precise bursting of all HVC-RA neurons. For each 'target neuron', a random 'source neuron' is selected that is able to satisfy spatial and time constraints using a connection from the synaptic pool. Spatial constraint is a geometrical one and requires a presynaptic neuron to be able to contact the dendritic tree of the postsynaptic neuron. The requirement is fulfilled if a sphere centered at the soma of the presynaptic neuron with radius equal to the synaptic distance intersects one of the dendrites of the postsynaptic neuron. Time constraint ensures that all inputs arrive within a synchronous time window to a postsynaptic neuron, fulfilling the polychronicity principle. The constraint is satisfied if  $|t_{target} - \tau_{int} - \tau_{syn} - t_{source}| \leq \tau_{sync}$ , where  $2 * \tau_{sync}$  is the size of the synchronous time window,  $t_{source}$  is the burst onset time of the 'source neuron',  $\tau_{int}$  is the average integration time constant of HVC premotor neurons from onset of the synaptic inputs to burst threshold, and  $t_{target}$  is the putative burst onset time of the 'target neuron'. When multiple connections satisfy both the spatial and the time constraints, the one that has the smallest  $|t_{target} - \tau_{int} - \tau_{syn} - t_{source}|$  is selected, corresponding to the input arriving on time. The connection is placed at the intersection point on the dendrite of the 'target neuron' and is removed from the synaptic pool. 'Target neuron' is removed from the set of target neurons in two cases: if the number of inputs to the 'target neuron' reaches  $N_{max}$ , and if the 'target neuron' cannot be contacted by any of the source neurons with any of the connections from the synaptic pool.

If after the second step the synaptic pool is not empty, new  $N_{new\ target}$  'target neurons' are sampled in the third step (iii) to increase the network size (see Fig. 3.11D). A new 'target neuron', which does not have any input or output connections, is added into the network by randomly selecting one 'source neuron' and placing one of the remaining connections from the synaptic pool onto a neuron satisfying spatial constraint. The putative burst onset time of the new 'target neuron' is defined as:  $t_{target} = t_{source} + \tau_{syn} +$

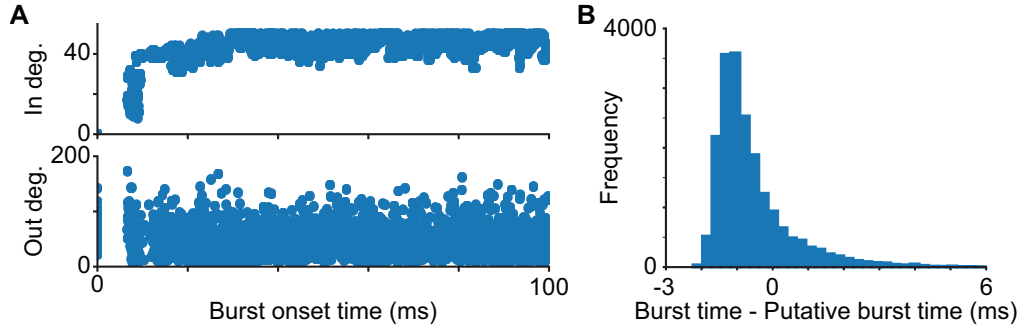


**Figure 3.12.** Behavior of the wiring algorithm. (A) In and out degrees of the neurons for the first 100 ms of dynamics. In degrees of neurons with burst onset times within first 20-30 ms demonstrate a transient state, in which the neurons have lower in degree. It is caused by the influence of synchronously firing starter neurons (see text). (B) The difference between actual burst onset times and the putative burst onset times assigned to target neurons during wiring. Most neurons have a slightly negative difference  $\sim -1$  ms, meaning that the neurons integrate 1 ms faster than the integration time in the algorithm.

$\tau_{int}$ . Then, the set of 'target neurons' is restored back to its original state in the beginning of the second step, and new sampled targets are added to the set. All connections made between neurons in step (ii) are removed and put back to the synaptic pool. Next, steps (ii) and (iii) are repeated until synaptic pool is exhausted. This procedure ensures that new sampled 'target neurons' get enough connections from the 'source neurons' and increases robustness of the algorithm.

The wiring algorithm described above is computationally expensive in case of many output connections. Indeed, step (ii) of the algorithm involves checking both if connection can be geometrically placed on one of the dendrites of a target neuron and if connection satisfies polychronicity principle. Both checks often fail, which results in long search of an appropriate presynaptic source neuron and slow algorithm performance.

### 3.7.2 Polychronous network with satisfied HVC constrains

To compare the network directly with pruned synfire chain, we wire a polychronous network with spatial synaptic distribution and axonal delays matching the experimental data in HVC, 45 output connections per neuron (50 inputs at most) and moderate excitation and inhibition  $G_{ee} = G_{ei} = 0.050 \text{ mS/cm}^2$ . We use a synchronous time window of 4 ms and set integration time to 5 ms. The noise inputs to HVC-RA and HVC-I neurons are turned off during polychronous network wiring to ensure deterministic behavior of the wiring algorithm.

During initial iterations, the network goes through a transient state, in which the

number of input and output connections have not yet reached a stable value (see Fig. 3.12A). Neurons with burst onset times within first 20-30 ms of dynamics, have smaller number of inputs. This transient is caused by the influence of synchronous starter neurons. Since axonal delays have a wide distribution, synchronously firing starter neurons are not able to provide high convergence to initially recruited targets. With more iterations of the algorithm, burst onset times of neurons spread, which allows the efficient use of all delays and leads to a larger convergence of inputs.

The algorithm establishes new connections to the target neurons using their putative burst onset times, assigned at the time when the targets are recruited. The use of putative burst onset times ensures that connections arrive within a synchronous time window. The actual burst onset times of target neurons change a lot during iterations of the algorithm due to the gradual increase in the number of their input connections. Therefore, if we used the actual burst onset times, connections would not arrive synchronously. That raises a question of how different putative burst onset times are from the actual ones. The majority of neurons have a slightly negative  $\sim -1$  ms difference between actual burst onset times and the putative burst onset times (see Fig. 3.12B). This difference suggests that our predictions on the integration times of the neurons are off and the neurons integrate 1 ms faster than the integration time in the algorithm. The magnitude of the difference depends on the strength of excitation and inhibition used in the algorithm. With strong excitatory connections, the neurons will integrate even faster, while the use of stronger inhibition will increase the integration time. In practice, having a small difference about 1 ms does not create any problems with the algorithm's performance. Larger differences need to be adjusted by the corresponding change in the strength of connections or integration time to ensure the proper synchronous arrival of inputs.

The wired polychronous network does not have any apparent structure that could be revealed by visualizing the network using synaptic weights between HVC-RA neurons. Fig. 3.13A shows network topology plotted with Kamada-Kawai algorithm in Pajek software program for network analysis [113]. The spatial synaptic distribution agrees well with experimental one, confirming the correct algorithm performance (see Fig. 3.13B). Since axonal delays are sampled based on synaptic distances, the axonal delay distribution automatically matches the experimental. The neurons have a tight distribution of in-degrees with a prominent peak at 50 inputs - the maximal allowed number of input connections (see Fig. 3.13C). Tight distribution of in-degrees ensures that during signal propagation all neurons receive similar excitatory input and can spike robustly. The out-degree distribution is wider with out-degrees ranging between 0 and almost 200 (see

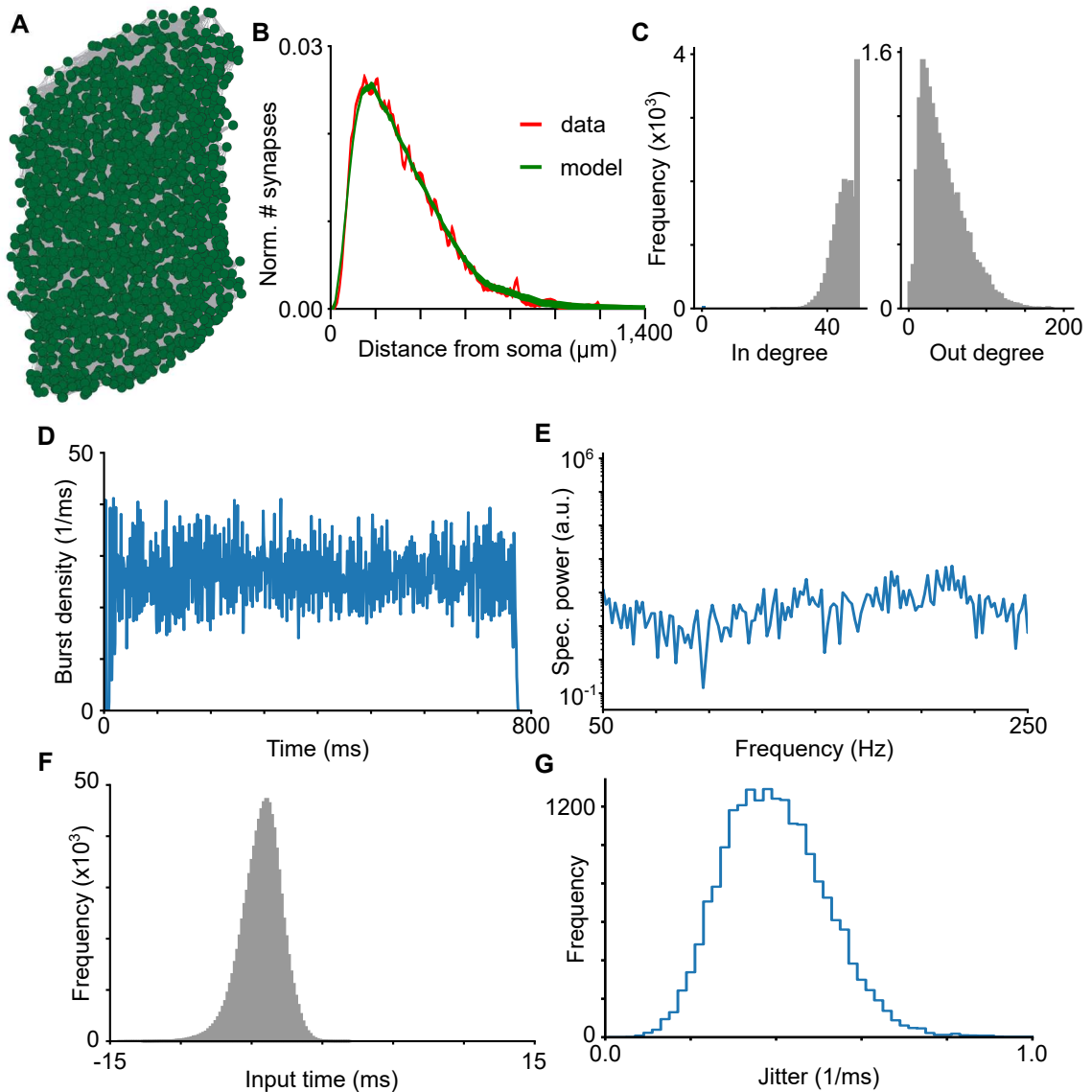


**Figure 3.13.** Polychronous network embedded in space. (A) Plot of network topology based on synaptic weights (see text) does not show any apparent network structure. (B) Synaptic spatial distribution matches the experimental. (C) In (left) and out (right) degree distributions. In degree distribution is tight with a prominent peak at the maximal allowed number of inputs (50). Out degree distribution is much wider, with center neurons having numerous outputs, and edge neurons having a few. (D) Burst onset density histogram shows continuous and smooth network dynamics. (E) Spectral power analysis does not show any distinguishable oscillations in activity. (F) Input time histogram shows the absence of late inputs, those with positive input times. (G) Jitter in burst onset times is below 1 ms, consistent with experimental sub-millisecond range precision.

Fig. 3.13C). Large difference in the shape between in and out degree distributions is created by step (ii) of the wiring algorithm, in which target neurons are connected in the order of the number of inputs they receive, starting from the smallest. Therefore, the algorithm pushes the in-degree distribution to the right, as close as possible to the maximal number of allowed inputs. At the same time, it does not control the out degree, turning some neurons into the hub neurons with numerous output connections. The hub neurons correspond to the neurons near the center of HVC, while neurons with small number of outputs are located at the edge of HVC. This is not surprising, since center neurons have more local candidates to connect and therefore they more often satisfy the spatial constrain of the algorithm.

Dynamics of the network is continuous and smooth, with no silent gaps in burst density (see Fig. 3.13D). Spectral power analysis also does not reveal any distinguishable oscillations (see Fig. 3.13E). Thus, the wired polychronous network does not have a disadvantage of synchronously firing neurons, as in the case of pruned synfire chain. What about the late inputs, which are numerous for pruned chain due to the presence of widely distributed axonal delays? The wired polychronous network contains only a negligible amount of late inputs ( $\sim 0.03\%$ , see Fig. 3.13F) with majority of inputs arriving within time window of 4.5 ms (5-th percentile is -6.8 ms, 95-th percentile is -2.2 ms). This is close to the synchronous time window size of 4 ms used in the algorithm. The average input time is -4.3 ms, which roughly corresponds to the average neuronal integration time of  $\sim 4$  ms. So far, the wired polychronous network demonstrates properties superior to the pruned synfire chain and fully compatible with the experimental observations. But is this network precise? The estimated jitter in burst onset times, based on 25 testing trials, is  $0.41 \pm 0.12$  ms (see Fig. 3.13G), the value well in sub-millisecond range, which is consistent with experimental data. Therefore, we conclude that the wired polychronous network satisfies all HVC constrains and produces smooth and continuous dynamics with no dis-functional late inputs.

### 3.7.3 Investigation of polychronous networks

We next wonder how the distribution of axonal conduction delays affects wiring of polychronous networks. To address this questions, we simplify the model to the most basic components by eliminating space and interneurons. The simplified model consists of 20,000 HVC-RA neurons. Connections between the neurons does not contain the spatial aspect and are characterized by delay-weight pairs. We use a modified version of our wiring algorithm, that ignores the synaptic spatial distribution and spatial constrain.

We use 170 output connections per HVC-RA neuron (with the maximal number of inputs set to 180), as in the experimental data. Since the interneuron population is absent and the number of inputs is higher than in the pruned chain case, we set a smaller maximal strength of excitatory connections  $G_{ee} = 0.004 \text{ mS/cm}^2$ . We also set a synchronous time window size to 1 ms, to achieve more synchronous arrival of inputs.

When we wire a polychronous network using axonal conduction velocity as in real HVC (i.e., normal velocity), the network produces smooth activity with no obvious oscillations in burst density (see Fig. 3.14A). However, when we down-scale all delays by using ten times faster (i.e., 10x) axonal conduction velocity, dynamics of the wired polychronous network contains synchronously firing groups of neurons separated by silent intervals  $\sim 6\text{-}7$  ms (see Fig. 3.14B). Our collaborators at NYU compared model burst density with the burst density of extracellularly recorded HVC-RA neurons in adult zebra finch during singing (see Fig. 3.14C). Briefly, for each syllable, burst onset times of recorded HVC-RA neurons were extracted and aligned to syllable onset times. Then, synthetic data was created by sampling burst onset times randomly from the model distribution of burst density, preserving the syllable length and the number of recorded neurons. , the mean spectral power between 155-180 Hz was computed for each syllable and averaged. By repeating this procedure 10,000 times, confidence intervals of the mean spectral power were estimated as  $\pm 3$  standard deviations from the mean. The comparison confirmed that the network with normal conduction velocity did not contain distinguishable oscillations in burst density, while the oscillations in the network with 10x velocity were significant. Next, we systematically vary the axonal conduction velocity between 0.5x and 10x (see Fig. 3.14D) and estimate the mean spectral power between 155-180 Hz (see Fig. 3.14D). The oscillations in burst density develop gradually, and are significant for velocity larger than 2x.

Why do oscillations in neural activity emerge for fast axonal conduction delays? To understand this, let's consider a simple extreme case of infinitely fast axonal conduction velocity, which corresponds to zero delays. In our wiring algorithm, at each iteration neurons in the starter seed receive synchronous external input and therefore burst synchronously. When a first target neuron is recruited, it is assigned a burst onset time based on the burst time of a presynaptic starter neuron and the integration time, which is identical to all neurons. Since there is only a single value for the axonal delays, all starter neurons will establish convergent connections to this target neuron. When its number of inputs reaches the maximal allowed value, the second target neuron is recruited with an identical burst onset time. Similar convergent connections will emerge to the second

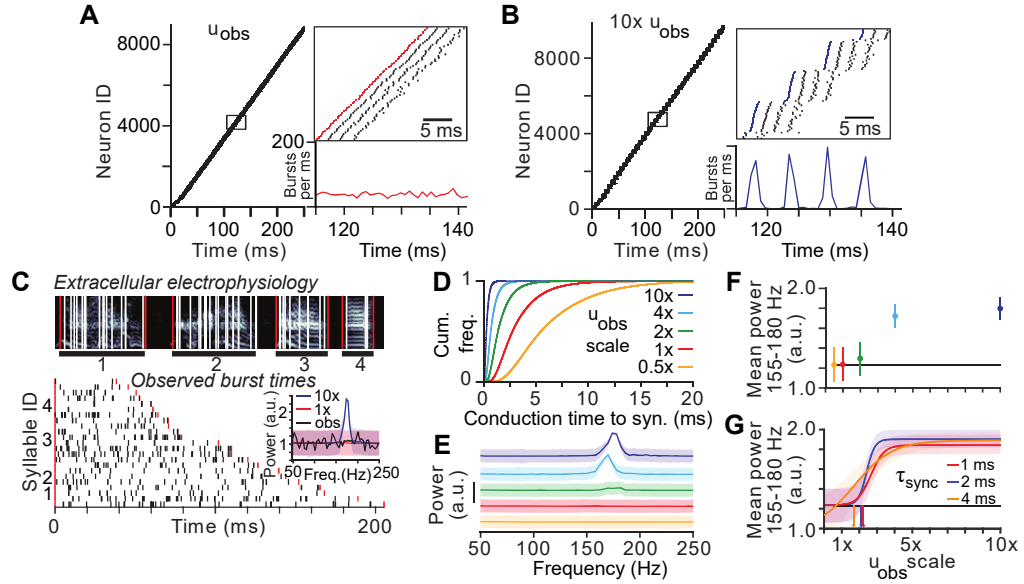


**Figure 3.14.** Polychronous networks with different axonal conduction velocity. Spike raster plot and burst onset density histogram of a polychronous network with axonal conduction velocity observed in HVC (i.e., normal) (A) and ten times faster (B). The network with faster conduction velocity shows prominent oscillations and silent gaps in burst density. (C) Comparison with burst activity of extracellularly recorded HVC-RA neurons in adult zebra finch, performed by our collaborators in NYU (see text), shows that the network with normal conduction velocity does not have distinguishable oscillations in burst density, while the network with 10x faster velocity contains strong peak in spectral power at  $\sim 180$  Hz. (D) Cumulative density plots for different scales of axonal conduction velocity. (E) Spectral power of burst onset density for different values of axonal conduction velocity. (F) Mean spectral power in frequency band 155 - 180 Hz versus axonal conduction velocity. Transition from smooth to oscillatory neural activity happens with increase in conduction velocity. (G) Fits of mean spectral power in frequency band 155 - 180 Hz versus axonal conduction velocity for different values for synchronous window size. Larger size of synchronous window smooths the transition.

target from the starter neurons and the procedure will repeat until synaptic pool is exhausted. As a result, the first iteration of the algorithm creates a perfect synfire chain group, receiving all-to-all connections from starter neurons. Then, the second iteration of the algorithm creates the second synfire group and so on, until all HVC-RA neurons are incorporated into the network. Thus, identical axonal delays lead to the emergence of perfect synfire chain. These results hold when delays are not exactly identical but sufficiently similar, as happens in the case of fast axonal conduction velocity 10x.

Our previous argument is based on the assumption that starter neurons burst synchronously. What happens if this assumption is violated? To address this question, we run our wiring algorithm with starter neurons receiving external inputs with arrival times sampled randomly within 7 ms. The network wired using axonal delay distribution

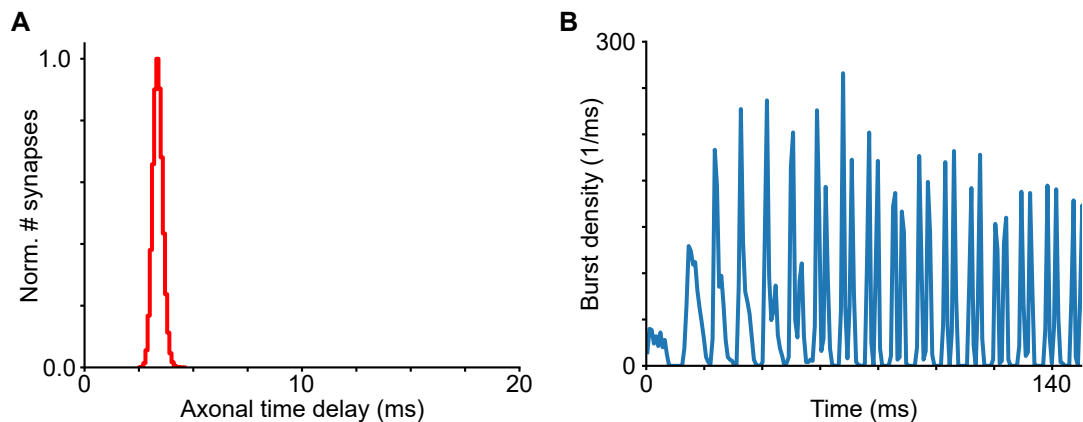


**Figure 3.15.** Two parallel chains emerge when wiring a polychronous network with narrow axonal delay distribution and starter neurons with a fixed spread in burst onset times (here, 7 ms). (A) Axonal delay distribution used in wiring is log-normal distribution with mean 3.4 ms and variance  $0.05 \text{ ms}^2$  (B) Burst density of the wired network shows two distinct peaks, meaning that the network contains two separate parallel chains.

with mean 3.4 ms and variance  $0.05 \text{ ms}^2$  (see Fig. 3.15A) contains two parallel synfire chains, as revealed by a double peak in burst density (see Fig. 3.15B). Note, that due to the spread in burst times of starter neurons there is no peak in burst density near time  $t = 0 \text{ ms}$ . Why 2 parallel chains emerge instead of a single chain, as in the case of synchronous starter neurons? The reason is again in almost identical axonal delays. In the first iteration of the wiring algorithm, starter neurons recruit new targets. But now starter neurons do not burst synchronously and therefore targets are assigned different burst onset times. In ideal case of an infinitely narrow synchronous time window of input arrivals, each starter neuron connects to a single separate target neuron. In subsequent iterations, target neurons become new source neurons and also send output connections only to a single neuron. Thus, numerous parallel chains of width 1 emerge. In practice, synchronous time window has a finite size and therefore there is a cross-talk between the chains. In simulation that produces 2 parallel chains, we use a synchronous window of size 1 ms, which is big enough to result in significant convergence of connections.

If our reasoning is correct, then we should obtain oscillatory dynamics in the case of narrow axonal delay distribution, and smooth dynamics for the wide distribution. To test this prediction, we first notice that the experimental axonal delay distribution in HVC can be well approximated by a log-normal distribution with mean 3.4 ms and standard deviation 2.27 ms. Based on that, we create a two-dimensional parameter grid with different values for the mean (between 0.5 ms and 4.5 ms) and standard deviation (between 0.25 ms and 2.75 ms) of log-normal distribution and use these

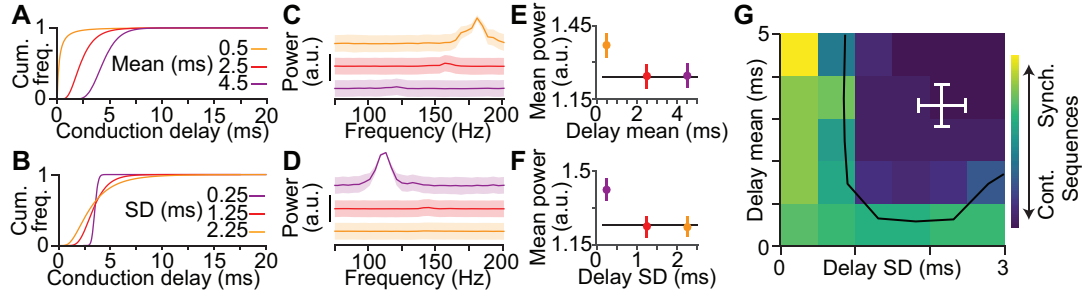


**Figure 3.16.** Polychronous network with different parameters of log-normal axonal conduction delay distribution. Cumulative density for three examples of log-normal axonal delay distributions with different mean and fixed standard deviation (i.e. std, here 1.25 ms, A), and different std and fixed mean (here 3.5 ms, B). (C-D) Corresponding spectral power shows prominent peak for small mean and small standard deviation of axonal delay distribution. (E-F) Corresponding mean spectral power in 75-200 Hz frequency band. Error bars: 5th and 95th percentiles (bootstrap). (G) Mean spectral power for a two-dimensional parameter grid of mean and std of axonal delay distribution. Black line separates region with significant oscillations in burst density (bright region with yellow and green color) from the region with smooth neural activity (dark region with blue color). White cross denotes the parameter region where HVC resides. It lies comfortably inside the region with smooth neural activity.

distributions to wire polychronous networks. For a fixed value of the standard deviation (see Fig. 3.16A,C,E for std 1.25 ms), prominent peak in spectral power emerges for a small mean. Log-normal distribution with small mean and large standard deviation looks very similar to exponential distribution, and most of the density is concentrated near zero. Thus, majority of delays have similar values, which leads to the emergence of oscillations. For a fixed value of the mean (see Fig. 3.16B,D,F for mean 3.5 ms), prominent peak in spectral power emerges for a small standard deviation. For a large mean and small standard deviation, log-normal distribution resembles a Gaussian, and most of the density is concentrated near the mean. Again, the majority of delays have similar values, which results in the emergence of synfire chain with oscillatory dynamics. Spectral power analysis of all polychronous networks in two-dimensional parameter space (see Fig. 3.16G) shows two distinct regions: one with highly oscillatory activity, and another one with smooth activity. The parameter region corresponding to axonal delays in HVC (see white cross in Fig. 3.16G) is comfortably inside the smooth activity region.

### 3.7.4 Polychronous network with uniform delay distribution

Log-normal distribution used in wiring polychronous networks is a long-tail distribution with a small number of particularly long delays. Are these long delays important to achieve smooth neural dynamics, or is it just the width of axonal distribution that

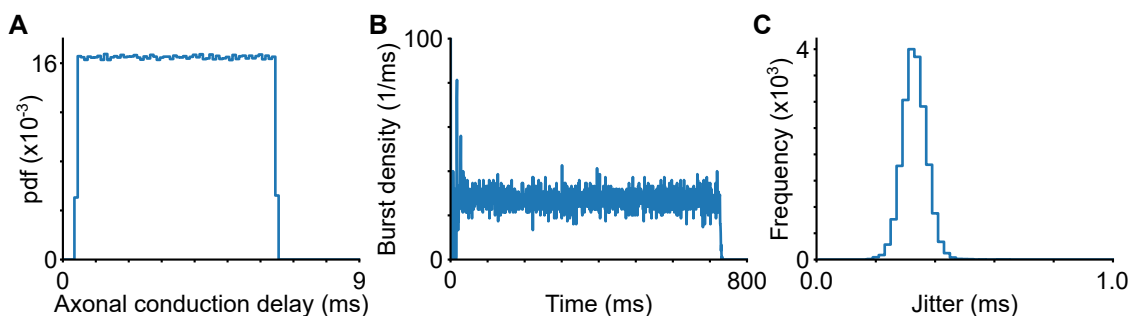


**Figure 3.17.** Polychronous network with wide uniform axonal delay distribution (mean = 3.5 ms and std = 1.75 ms) produces smooth and precise neuronal activity. (A) Pdf of the axonal delay distribution used in wiring. (B) Burst density of the wired network shows smooth neuronal activity. (C) Jitter in burst onset times is in sub-millisecond range.

controls the smoothness? To address this question, we wire polychronous networks with uniform axonal delay distribution. Axonal distribution with mean 3.5 ms and standard deviation 1.75 ms (close to HVC values, see Fig. 3.17A) produces a polychronous network with smooth network dynamics (see Fig. 3.17B). The network is also precise as other polychronous networks reported above (see Fig. 3.17C). Therefore, we conclude that the width of axonal delay distribution controls the smoothness of neural activity in polychronous networks. Distributed delays alone are enough to produce continuous dynamics with no silent intervals.

### 3.7.5 Randomly rewired polychronous network

During the construction of a polychronous network, we make connections between neurons to achieve synchronous arrival of inputs. It results in the emergence of a pristine feedforward network, i.e. the network with no recurrent connections or loops. Is this perfect alignment of all inputs necessary to achieve continuous network dynamics? Can we have a more random feedforward network with some recurrent connections that explains the data? To address these issues, we explore how random rewiring of the grown polychronous network affects its dynamics.

Starting from the polychronous network wired with log-normal axonal delay distribution with mean 3.5 ms and std 2.25 ms, we rewire a fraction of all synapses randomly, creating recurrent neural networks. Networks with both moderate (fraction rewired = 0.2) and large (fraction rewired = 0.65) rewiring of synapses produce smooth neural dynamics (see Fig. 3.18A,B). As expected, the jitter in burst onset times goes up with the increase in the fraction of rewired connections (see Fig. 3.18C). Rewiring of more than 65% of

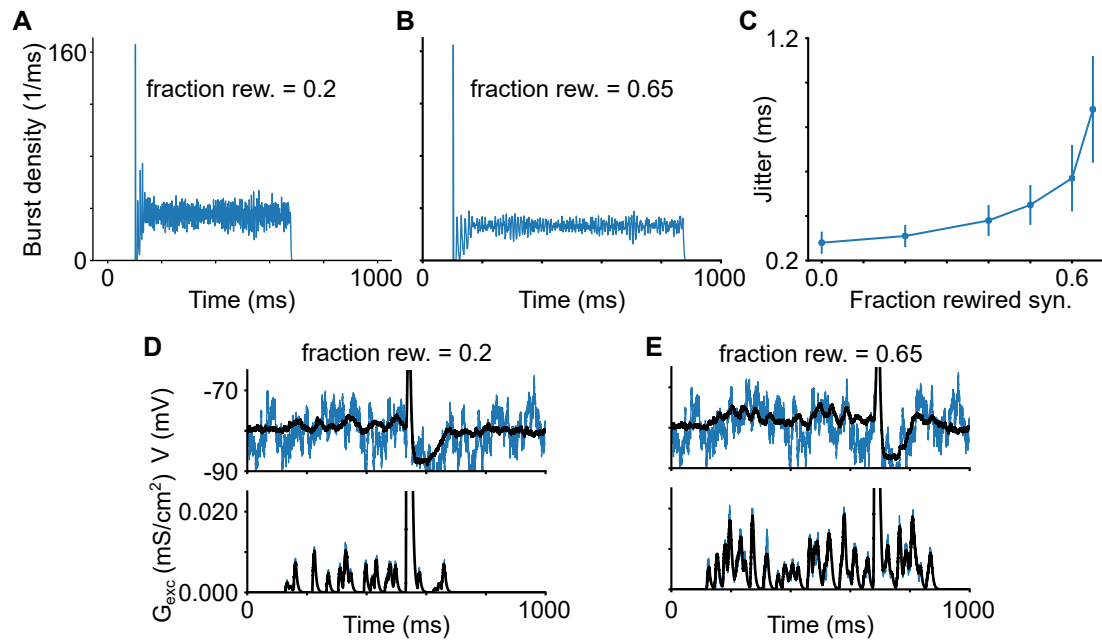


**Figure 3.18.** Randomly rewired polychronous network demonstrates smooth dynamics and supports sequence propagation until up to 65% of rewired synapses. Burst density of the network with 20% (A) and 65% (B) of rewired synapses does not reveal oscillations. (C) Jitter in burst onset times goes up with increase in the fraction of rewired synapses, until the network breaks completely. Example of additional EPSPs (top) and conductance traces (bottom) throughout the sequence, created by the random connections in the network with 20% (D) and 65% (E) of rewired synapses. Blue lines show one trial traces, while black lines represent the average traces. EPSPs are larger for higher fraction of rewired connections.

the network connections produces networks that are not able to support propagation of the signal. Interestingly, rewired synapses create additional excitatory postsynaptic potentials (EPSP) in the neurons throughout the sequence, and the EPSPs are more pronounced at larger rewiring fractions (see Fig. 3.18D,E). These EPSPs are very similar to the stereotypical EPSPs observed in the experiment with singing zebra finches [65]. We conclude, that neural networks with polychronous feedforward sequences containing some random recurrent connections also produce continuous and precise neural activity.

## 3.8 Alternative ways to achieve smooth neural activity

### 3.8.1 Random network

If a polychronous network with a large amount of 65% randomly rewired synapses is able to support robust propagation of a continuous sequence, we wonder whether a completely

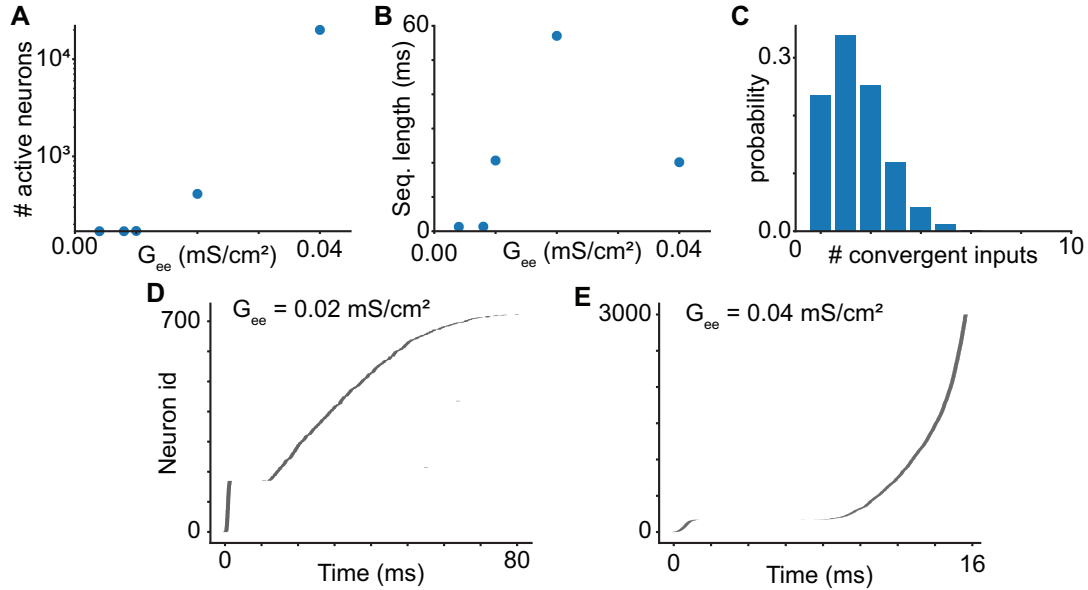


**Figure 3.19.** Random network cannot support propagation of long smooth sequences. (A) Average number of active neurons increases with the strength of excitatory synaptic weight, eventually incorporating the entire network. (B) Average temporal sequence length shows a non-monotonic dependence on synaptic weight. First, sequence becomes longer due to incorporation of more active neurons. For larger weights, the entire network spikes almost synchronously with a rapid response, reflecting the presence of divergent recurrent connections. (C) Distribution of the number of convergent inputs from 170 random presynaptic neurons to a randomly chosen HVC-RA. Due to the random network topology, convergence is low and a strong excitatory synaptic weight is needed to support signal propagation. Example of network dynamics with maximal synaptic weight  $G_{ee} = 0.02$  mS/cm<sup>2</sup> (D), producing a short sequence, and  $G_{ee} = 0.04$  mS/cm<sup>2</sup> (E), producing a synchronous spiking of the entire network (only 3000 neurons shown)

random recurrent network can do the same. To address this question, we create a random network of 20,000 HVC-RA neurons with 170 connections per neuron. Only a single connection between a pair of neurons is allowed and we prohibit any self-connections. All axonal delays are set to zero and we assume no spatial structure.

We randomly sample 170 starter neurons and excite them by a synchronous excitatory conductance kick of 300 nS. Produced network dynamics is characterized by the number of active neurons (i.e. those that produced bursts) and the sequence length (time difference between the last burst onset time and the first burst onset time of all neurons). We repeat the procedure 100 times by randomly sampling different starter neurons and estimate the mean number of active neurons (see Fig. 3.19A) and the mean sequence length (see Fig. 3.19B) for systematically varied strength of excitatory synaptic weights. For a small strength of excitatory synaptic weight, the sequence fails to activate and only

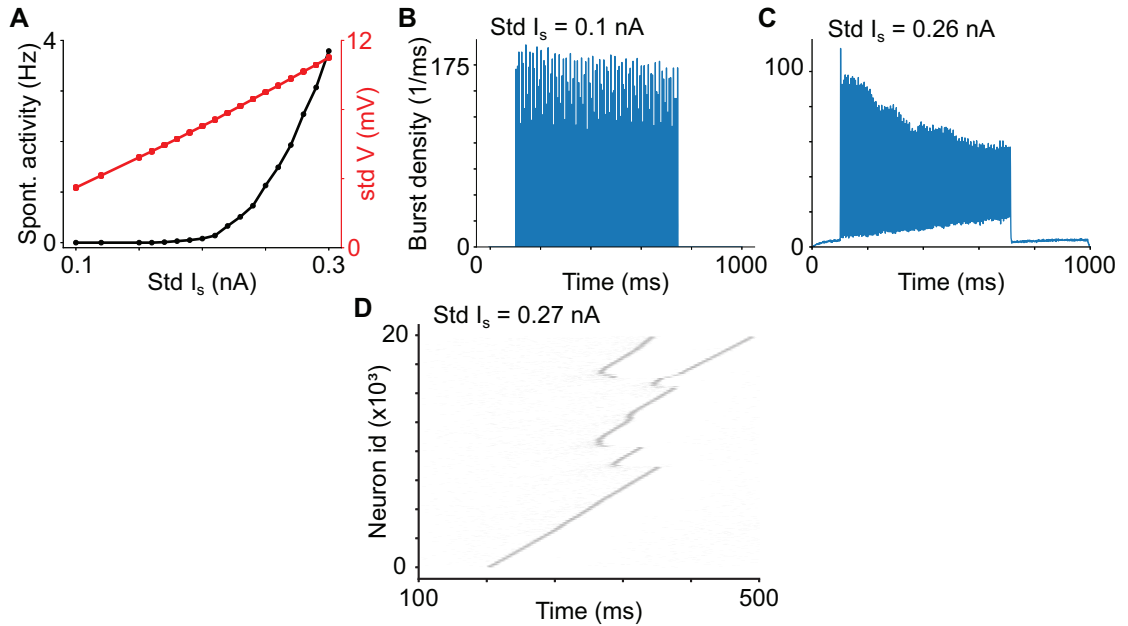


**Figure 3.20.** Synfire chain with large noise fails to produce smooth neural sequence. (A) Spontaneous activity (left y-axis) and strength of membrane potential fluctuations (right y-axis) of HVC-RA neuron versus the strength of white noise current injected to somatic compartment. Burst density for simulations with moderate noise  $\text{std } I_s = 0.1$  nA (B) and large noise  $\text{std } I_s = 0.26$  nA (C) contain prominent oscillations. (D) Spike raster plot of a simulation with larger noise  $\text{std } I_s = 0.27$  nA produces chain reactivations.

starter neurons produce bursts. For larger synaptic weights, there is a short sequence produced that does not span more than 100 ms and incorporates only a small fraction of the network (less than 1000 neurons, see Fig. 3.19D). Finally, in the case of strong excitatory synapses, the network responds rapidly with almost synchronous spiking event that incorporates the entire network, thus producing run-away excitation (see Fig. 3.19E).

The network behavior is caused by the highly divergent nature of connections in the random network. For example, randomly chosen set of 170 neurons sends at most  $\sim 5$  convergent inputs to postsynaptic neurons (see Fig. 3.19C). That requires exceptionally strong synapses to drive the activity of the network. Due to the numerous recurrent connections and no mechanism to control the activity level (for example, inhibition), the network easily falls into run-away excitation regime.

Thus, we conclude that random networks without inhibition fail to produce long sequences due to the lack of convergent connections.

### 3.8.2 Synfire chain with strong noise

The next simple model having a high convergence of inputs is a synfire chain. It produces prominent oscillations in burst density due to synchronous activity in synfire groups. Using a pruned chain model, we have already demonstrated that the changes in the strength of excitation and inhibition do not significantly affect the smoothness of neural activity. Another idea is to make neurons very noisy in the hope to spread burst times of the neurons and smooth the oscillations.

We assemble a synfire chain model with 117 groups and 170 HVC-RA neurons per each group (19790 neurons in total). The groups are connected sequentially in all-to-all manner, with the last group sending no outputs. There is no spatial structure in the model, nor the interneuron population, similar to model where we explored polychronous network with different axonal delay distributions. We set all axonal delays to zero and use maximal synaptic weight  $G_{ee} = 0.004 \text{ mS/cm}^2$  as in the polychronous network model.

We systematically vary the membrane potential fluctuations in the neurons by changing the amplitude of white noise current injected to somatic compartment (see Fig. 3.20A). White noise input to dendrite is set to zero in order to prevent neurons from producing spontaneous dendritic spikes and as a result somatic bursts. For strong current injections with white noise amplitude larger than 0.2 nA, the neurons spike spontaneously, reflecting large voltage fluctuations. We define a burst as a sequence of more than 1 spike with interspike intervals less than or equal to 10 ms. In this case, spontaneous bursts are sometimes produced at a high noise level. To make the burst density plots, we run 50 simulations of synfire chain dynamics at a given noise level and generate an average time histogram for all elicited bursts in the simulations. Neurons in the starter synfire groups are ignited by a strong synchronous conductance pulse of 300 nS at time 100 ms. For small noise amplitude 0.1 nA, burst density contains strong oscillations, similar to the pruned chain (see Fig. 3.20B). For large noise amplitude 0.26 nA, neurons are spontaneously active, which is seen as non-zero burst density before the ignition of the starter synfire group (see Fig. 3.20C). Strong noise, however, does not significantly smooth the oscillations in burst density. White noise with amplitude larger than 0.26 nA, leads to spontaneous reactivations of the synfire chain, representing a noise limit in the model (see Fig. 3.20D). Therefore, we conclude that neural activity of synfire chain cannot be made smooth with the increase in noise fluctuations.

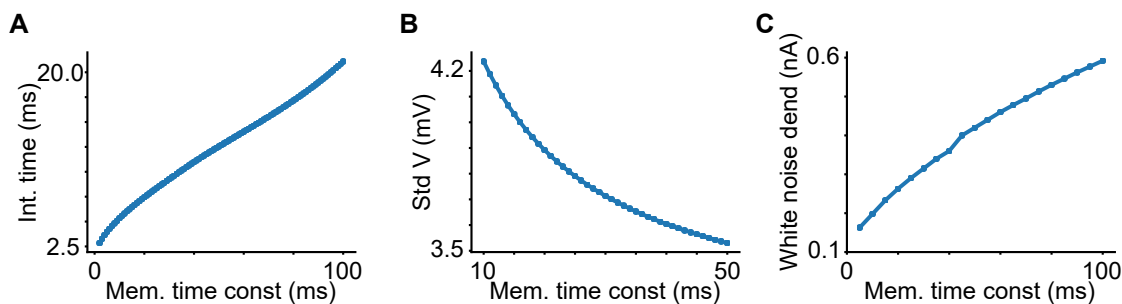


**Figure 3.21.** Dendritic membrane time constant affects both the integration time and membrane potential fluctuations in HVC-RA neurons. (A) Integration time increases almost linearly with dendritic membrane time constant. (B) Same strength of white noise current stimulation (0.1 nA in soma and 0.2 nA in dendrite) produces smaller membrane potential fluctuations for a neuron with larger membrane time constant. (C) Adjusted strength of white noise stimulus to dendritic compartment, which produces the same membrane potential fluctuations.

### 3.8.3 Synfire chain with distributed neuronal integration times

In the previous simulations, all neurons were modeled by the same set of differential equations and therefore had the same physiological properties. Real biological neurons are never identical and can differ a lot in terms of their shape, input resistance, capacitance etc. We therefore wonder whether distributed physiological parameters of the neurons can smooth the neural dynamics of a synfire chain network. Neurons in synfire groups receive synchronous excitatory input. Thus, in order to spread their burst times, we need the neurons to have a distribution of response times, i.e., we need different neuronal integration times. The integration time depends on the strength of input that the neuron receives and the membrane time constant, which is proportional to the leak resistance and membrane capacitance. Below we explore how distributed dendritic membrane time constants affect the smoothness of synfire chain dynamics.

To investigate how dendritic membrane time constant affects the neuronal integration time, we perform a simulation in which one HVC-RA neuron (i.e. postsynaptic neuron) receives 170 synchronous inputs from other HVC-RA neurons (i.e. presynaptic neurons) with synaptic strength of each input sampled randomly between 0 and  $0.004 \text{ mS/cm}^2$ . Presynaptic neurons are ignited by a delivery of excitatory conductance kicks of strength 300 nS. The delivery times of excitatory kicks are sampled randomly within 1 ms time window to create a spread in presynaptic burst times and, as a result, a spread in input arrival times to the postsynaptic neuron. We also tested that the results do not change significantly with a larger window size of 6 ms. In the simulation, we systematically vary the dendritic membrane time constant and estimate the integration time of the

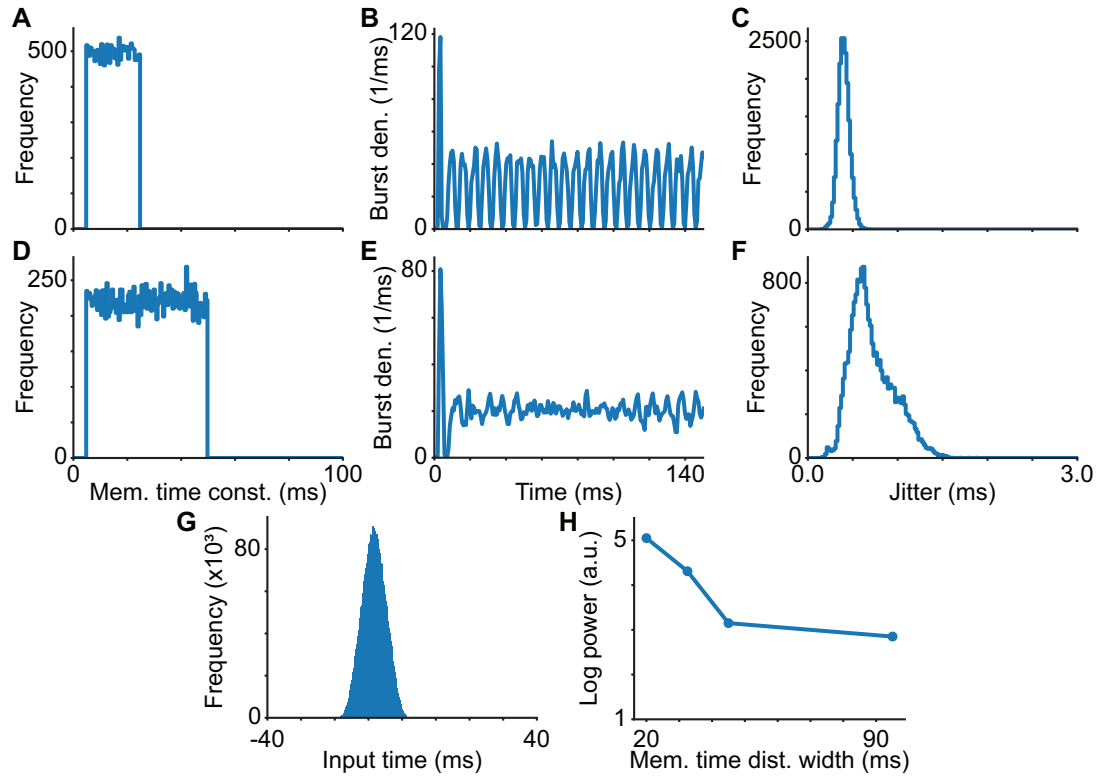


**Figure 3.22.** Synfire chain with widely distributed membrane time constants produces smooth activity. Examples of two synfire chains with uniform membrane time constant distributions between 5 ms and 25 ms (A-C) and between 5 ms and 50 ms (D-G). (A,D) Histograms showing membrane time constant distributions. Burst density plots show oscillations in the case of narrow distribution (B) and smooth activity for a wide distribution (E) of membrane time constants. (C,F) Jitter in burst onset times. The jitter increases for neurons with longer integration times (F). (G) Histogram of input times shows a wide distribution. (H) Log of maximal spectral power of burst density between 50 Hz and 250 Hz shows a transition from oscillatory to smooth activity.

neuron, defined as the difference between postsynaptic burst onset time and the mean input arrival time. The integration time changes almost linearly with the membrane time constant and varies in a large range between 2.5 ms and 20 ms for membrane time constants between 5 ms and 100 ms (see Fig. 3.21A).

We notice, that the same strength of white noise current stimulation (0.1 nA in soma and 0.2 nA in dendrite) produces different membrane potential fluctuations depending on the membrane time constant (see Fig. 3.21B). This is expected behavior, since large membrane time constant effectively weakens the strength of received input. To account for that, we adjust the white noise current stimulus to dendritic compartment, so that an HVC-RA neuron has the same level of membrane potential fluctuations regardless of

its membrane time constant (see Fig. 3.21C).

Next, we assemble a synfire chain with parameters identical to the ones in the previous section. We sample dendritic membrane time constants from uniform distribution. We set the smallest dendritic membrane time constant to 5 ms and systematically vary the upper range of the uniform distribution. For a uniform distribution of dendritic time constants between 5 ms and 25 ms (see Fig. 3.22A), the dynamics still contains prominent oscillations (see Fig. 3.22B) and is precise with sub-millisecond jitter in burst onset times (see Fig. 3.22C). Wider distribution with membrane time constants between 5 ms and 50 ms (see Fig. 3.22D), produces a smooth burst density with no distinguishable oscillations (see Fig. 3.22E). However, due to long integration times, neurons are more affected by noise and their burst onset times become less precise (see Fig. 3.22F). The distribution of input times relative to postsynaptic burst onsets is wide and shifted to the left, compared to original synfire chain, reflecting both the spread in integration times and the spread in presynaptic burst times. Almost no inputs are arriving late, making an efficient use of all synapses. Overall, we observe a disappearance of oscillation in burst density for wide dendritic membrane time constant distributions (see Fig. 3.22H).

In the original model, dendritic membrane time constant is  $\tau = A_d * C_m / G_{d,L} = 10$  ms which results in neuronal integration times 4-5 ms. Given the experimentally observed  $\sim 5$  ms integration time of HVC-RA neurons [66], it is unlikely that real neurons in HVC have wide enough distribution of membrane time constants in order to achieve smooth dynamics assuming synfire chain connectivity.

### 3.8.4 Polychronous network with distributed neuronal integration times

Finally, we wonder whether we can achieve smooth network dynamics if we wire a polychronous network using distributed integration times, rather than distributed conduction delays. In the investigation of synfire chains with distributed membrane time constants, we sampled from a uniform distribution, which gives equal weights to both the central and edge values of the distribution. Provided that both spatial synaptic distributions and axonal delay distributions for efferent HVC-RA connections follow log-normal rather than the uniform distribution, we switch to a more realistic log-normal distribution for integration times. However, log-normal distribution has an unbounded support which extends from 0 all the way to infinity, which would generate unrealistic values for integration times. Therefore, we truncate a log-normal distribution on both

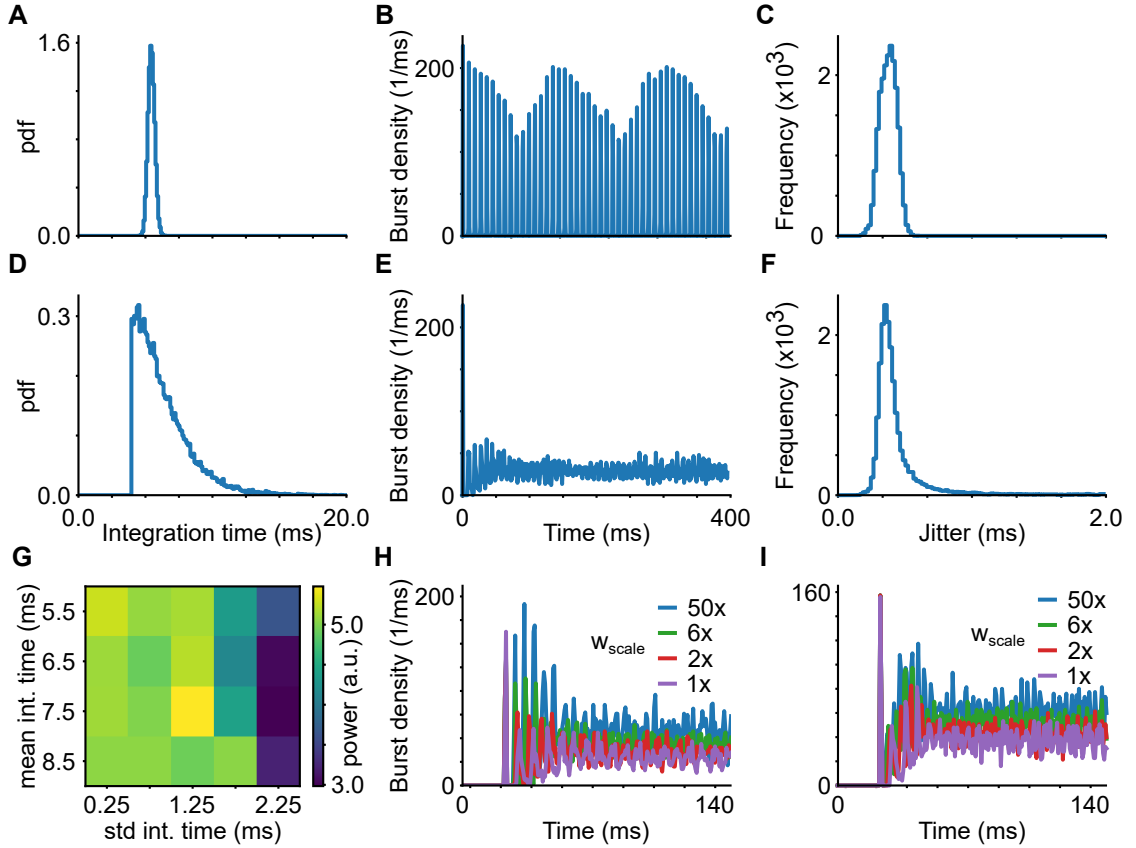


**Figure 3.23.** Polychronous network with wide log-normal distribution of integration times produces smooth dynamics. Results for polychronous networks wired with mean 5.5 ms and std 0.25 ms (A-C), and std 2.25 ms (D-F). (A,D) Pdf of integration time distributions. Burst density of network dynamics shows prominent oscillations (B) and smooth sequence (E). (C,F) Jitter in burst onset times. (G) Spectral analysis of burst density for polychronous networks wired with different mean (vertical axis) and standard deviation (horizontal axis) of integration time distribution shows smooth dynamics only for the largest standard deviation. Burst density plots with rescaled synaptic weights for a polychronous network wired with distributed integration times (mean = 5.5 ms, std = 2.25 ms, H) and those with distributed axonal delays (mean = 3.5 ms, std = 2.25 ms, I) shows prominent transient oscillations for distributed integration times.

the lower range (at 4 ms) and on the upper range (at 21 ms).

We systematically vary the mean and the standard deviation of the log-normal distribution of integration times and wire polychronous networks with 170 output connections per neuron with a maximal synaptic strength  $G_{ee} = 0.004 \text{ mS/cm}^2$  and a single axonal delay value of 3.4 ms, which corresponds to the mean axonal delay in HVC. Integration times of starter neurons are set to 4.0 ms to ensure synchronous spiking. The wiring algorithm proceeds in the same way as before, with the only difference that neurons have different integration times. The algorithm fails for small size of synchronous time

windows and we use a larger window of 6 ms.

Narrow integration time distribution with mean 5.5 ms and std 0.25 ms (see Fig. 3.23A) produces network with prominent oscillations in burst density (see Fig. 3.23B). The distribution with the same mean and large std 2.25 ms (see Fig. 3.23D) results in network with no distinguishable oscillations (see Fig. 3.23E). The wired networks are on average precise. Jitter distribution has a longer tail for larger standard deviation of integration times, due to noisy neurons with long integration times (see Fig. 3.23C,F). Overall, continuous dynamics is achieved only for the largest standard deviation used (2.25 ms, see Fig. 3.23G).

Do these polychronous networks wired with distributed integration times have different properties compared to the polychronous networks wired with distributed conduction delays? Neuronal integration time depends on the strength of excitatory connections, which may fluctuate in the real biological network. On the other side, axonal delays are determined by the geometry of connections (length and width) and are not assumed to change. Thus, the network wired with distributed integration times may be more resilient to the changes in synaptic weight strength. To test this hypothesis, we systematically rescale the synaptic weights of two grown polychronous networks and compare their dynamics. Polychronous network wired with distributed integration times (see Fig. 3.23H) shows strong transient oscillations, which are further enhanced by larger synaptic weights. Polychronous network wired with distributed axonal delays also shows some transient oscillations, but they are much less prominent. Why transient oscillations are so strong in the case of distributed integration times? This is because initial layers of this network are similar to synfire groups. To see this, let's consider the first iteration of the wiring algorithm, during which synchronous starter neurons recruit new targets into the network. Since there is only a single delay value, starter neurons converge perfectly on all recruited targets, forming a perfect synfire group. The targets in this group, however, have distributed integration times and do not fire synchronously. Thus, when they become new source neurons and recruit new targets, they are not able to converge perfectly and do not form a new perfect synfire group. Gradually, the burst onset times of target neurons spread more and shift the network topology away from a synfire chain.

We did not observe any other significant differences between these networks. Therefore, we conclude that distributed neuronal integration times can also be used to produce a smooth network dynamics. Whether real HVC-RA neurons have a wide enough distribution of integration times remains unclear and needs further experimental studies. Potentially, both distributed axonal conduction delays and integration times work

together to create a continuous neural sequence. However, our study provides a strong evidence that axonal delays alone can achieve this goal.

### **3.9 Conclusions**

In this section, we developed a detailed model of HVC microcircuit for zebra finch. The model incorporates all known experimental features of HVC, including realistic neuron numbers, spatial distributions and distributed axonal delays. We showed that a single synfire chain model produces strong oscillations in neural activity, inconsistent with experimental observations. Extension of the synfire chain model, several parallel synfire chains, were able to produce a smooth neural dynamics, however, with a loss in precision. In addition, due to distributed axonal conduction delays, synfire chain model contained a significant amount of late inputs, inefficient connections that do not drive postsynaptic neurons. Motivated by these observations, we created a polychronous network, the model in which all inputs arrive synchronously to postsynaptic neurons. We showed that the polychronous network with experimental axonal delay distribution was able to satisfy all experimentally known HVC constraints, including the smooth network dynamics. We further explored the role of axonal conduction delays in polychronous network and demonstrated that width of the axonal delay distribution controls the smoothness of network dynamics. Narrow distributions produced networks with prominent oscillations, while wide distributions resulted in networks with smooth dynamics. Therefore, axonal delays may play an important role in shaping neural dynamics and should not be ignored in neural network models.

# Chapter 4 |

## Sequence development in HVC

Development of neural circuits is an intricate process that involves many well-orchestrated steps. The newborn neurons commonly have to migrate long distances to their destinations, where they settle down, extend the dendrites and the axon, establish connectivity with other existing neurons and finally reach adult-like mature state. The birth order of neurons plays a critical role in the development of neural networks. In mammalian cortex, neurons that are destined to the deep cortical layers are born earlier than those to the superficial layers and this process is regulated by cell-intrinsic and environmental factors [96,97]. Depending on the order of birth, cortical neurons have to migrate different distances and get incorporated into local microcircuits with unique properties. In rodent hippocampus, earlier born neurons and late born neurons form distinctive parallel circuits through the hippocampal pathway [98]. However, the role of birth order in constructing microcircuits in local brain areas is unknown [99]. The premotor nucleus HVC of the zebra finch provides an excellent opportunity to investigate this issue.

Majority of HVC-RA neurons are born and added to HVC after hatch. The most active period of HVC-RA neurogenesis happens from 20 to 50 days after hatch [35], which coincides with the period of song learning. The other two major neuron types: interneurons and area X projecting neurons are get incorporated into HVC before hatch and are presumably mature during song learning [32]. Therefore, throughout vocal development, HVC-RA neurons have a wide range of birthdates, which provides an opportunity to investigate the HVC-RA birth order role in the formation of HVC microcircuit for song production.

Previous theoretical [100,101] and experimental [102] studies of HVC have proposed the gradual growth of a feedforward synaptic chain of HVC-RA neurons. However, the role of neurogenesis, happening actively during this process, has not been explored in any of these studies. Indeed, although neurogenesis in HVC has been observed for decades,

its role for song learning in zebra finch has remained a mystery [34, 103].

We start this Chapter by re-analyzing the publicly available data set of extracellular recordings of HVC projection neurons in singing juvenile zebra finches [104]. We find that in early stages of vocal development, HVC-RA neurons have less tight bursting patterns, presumably due to their immaturity. We also find that less tight bursts are the features of the neurons that burst later in the syllables, supporting the hypothesis that the network in HVC grows by recruiting new immature neurons to the end of the existing sequence.

Next, we develop a computational model of sequence growth in songbird HVC, which relies on a constant supply of newborn immature HVC-RA neurons. The model assumes that immature neurons are more spontaneously active and therefore they become prime targets of a self-organized growth process via synaptic plasticity. Once recruited, the new neurons fire readily at precise times, and they become mature. Neurons that are not recruited become silent and replaced by new immature neurons. The model predicts that the neurons get incorporated into the growing sequence based on their birth order, creating a correlation between birth date and firing time. Thus, the model can be tested directly by checking if earlier born neurons fire before the neurons that are born later.

The model also incorporates biologically realistic features of HVC, such as explicit population of interneurons, spatial distributions of HVC-I and HVC-RA, and distributed axonal conduction delays. These features provide novel insights into the formation of feedforward sequences with precise timing, such as the dependence of emerged network topology on axonal delay distribution, and the role of inhibition during sequence growth.

Significant portions of this Chapter are parts of the Tupikov and Jin, 2019 paper (unpublished).

## **4.1 Re-analysis of spike patterns of HVC projection neurons in juvenile zebra finches**

In recent study [102], Okubo et al. reported extracellular recordings of single neurons in HVC of juvenile zebra finches during vocal development. The authors observed a gradual increase in the fraction of projection neurons that were active during singing, and a gradual spread of the latency of their burst times relative to the syllable onsets. These observations are supporting the hypothesis that there is a gradual sequence growth in HVC during vocal development. Provided that during this period there is an active

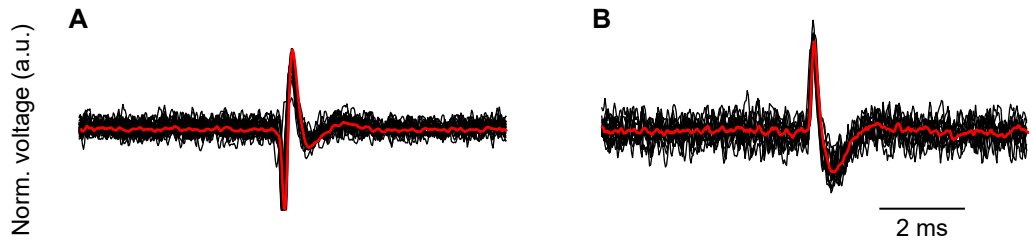


**Figure 4.1.** Projection neurons show two distinct spike shapes. (A) One spike shape has a strong hyperpolarizing dip in the membrane potential traces prior to the spike peak and another, much smaller, hyperpolarization after the peak. (B) Another spike shape does not contain the dip prior to spike peak, the membrane potential just stays flat until the action potential upstroke

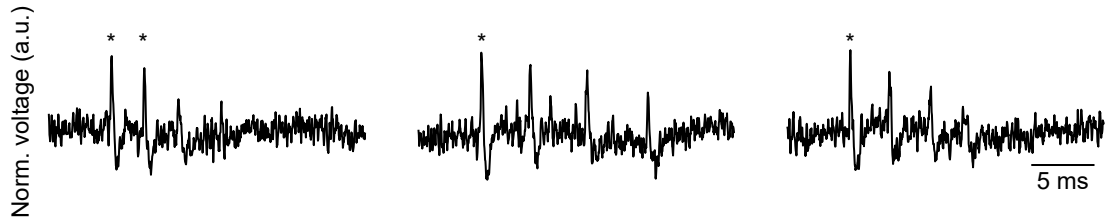


**Figure 4.2.** Examples of missed spikes in the data set. Spikes that were labeled in the data are marked with asterisk. Un-labeled spikes usually have smaller amplitude.

addition of new HVC-RA neurons, we wonder if immature neurons are involved in sequence formation. To address this question, we re-analyze the data set provided in the above mentioned study [104].

The dataset is organized into four stages of song development [102]: subsong, which is highly variable ( $\sim 48$  days post hatch (dph)); protosyllable song, which contains syllables with definable durations around 100 ms ( $\sim 58$  dph); multi-syllable song, which contains syllables with distinctive spectral characteristics ( $\sim 62$  dph); and motif song, which consists of a reliable sequence of syllables like adult song ( $\sim 73$  dph). The following neuron types are reported: HVC-RA neurons (identified by antidromic stimulations in RA), HVC-X neurons (identified by antidromic stimulations in area X) and HVC-p - putative projection neurons. The dataset contains audio and neural recordings with useful metadata: onset and offset syllable times; spike times of neurons; types of syllables, quality of single unit recording etc. The data is split based on the neuron identity. The spikes are also classified into artifacts and signal. In our analysis, we consider only recordings with high quality of single unit isolation  $\geq 2$ , and ignore un-classified population of neurons (HVC-p).

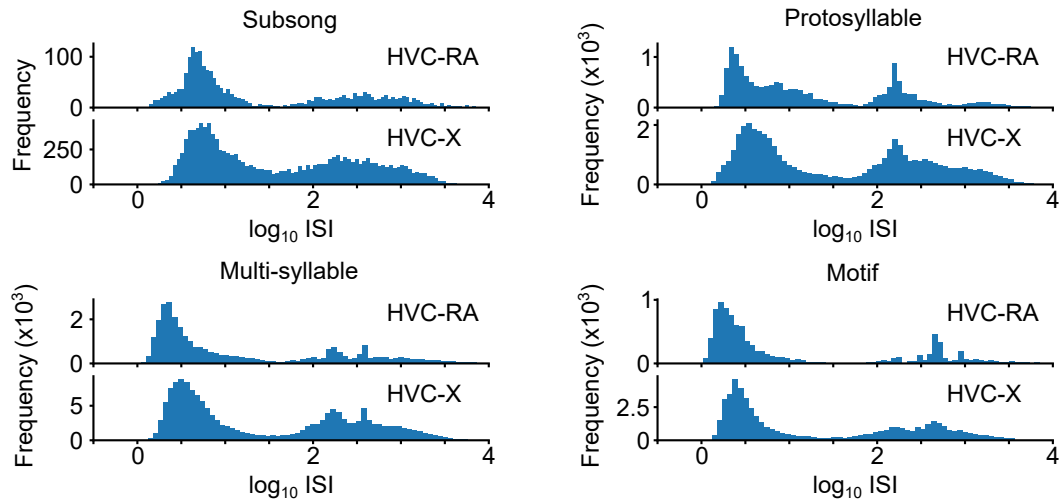


**Figure 4.3.** Distributions of interspike intervals (ISIs) of HVC-RA and HVC-X neurons in different stages of vocal development. At all stages, distributions are bimodal. One mode (with small ISIs) corresponds to spikes within individual bursts (i.e., "burst mode"). Another mode (with large ISIs) corresponds to interburst intervals due to repetition of the same sound in the song and determines the song rhythm (i.e., "rhythmic mode"). Both modes progressively tighten during song learning.

### 4.1.1 Data set exploration

During the exploration of the data set, we notice that projection neurons produce two different spike shapes. One spike shape has a strong hyperpolarizing dip in the membrane potential traces prior to the spike peak and another, much smaller, hyperpolarization after the peak (see Fig. 4.1A). Another shape does not contain the dip prior to spike peak, the membrane potential just stays flat until the action potential upstroke (see Fig. 4.1B). It also shows a more pronounced after-spike hyperpolarization. It is not clear if these differences in spike shapes are some artifacts in the recordings, or they actually represent populations of neurons with distinct physiological properties.

We also observe features in membrane potential traces that look like spikes, but were not labeled as spikes in the data set (see Fig. 4.2). These features often occur next to other groups of spikes, presumably forming bursts. We hypothesize that these features represent the actual spikes, which were missed in the data set due to their small amplitude. Indeed, many of the spike sequences start with high amplitude spikes and show a gradual decrease in the spike amplitude. Most of the observed features occur at the end of the spike sequences, when the amplitude is small.

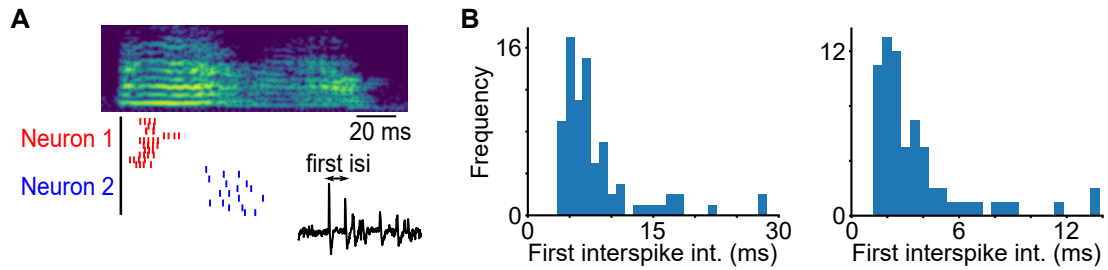


**Figure 4.4.** First interspike interval. (A) Example of spike patterns of two HVC-RA neurons in the protosyllable stage aligned to a syllable onset. First interspike interval is defined as the temporal distance between first two spikes in burst. (B) Two examples of first interspike distributions for individual HVC-RA neurons in protosyllable stage. Each distribution contains outliers, therefore a median of the distribution is used to estimate the first interspike interval of the neuron.

### 4.1.2 Interspike intervals

We start the analysis by looking into interspike intervals (ISIs) of different neuron types at different stages of vocal development. Throughout all song stages, distributions of ISIs contain two distinct modes (see Fig. 4.3). One mode (i.e., "burst mode"), with small interspike intervals, corresponds to spikes inside individual bursts. Another mode (i.e., "rhythmic mode"), with large interspike intervals, corresponds to spikes produced in different repetitions of the same sound, reflecting a song rhythm. All neuron types gradually develop tight distribution modes, which reflects more stable spike patterns. In subsong stage, the rhythmic mode does not have any noticeable peak, meaning that projection neurons do not burst rhythmically. The peak is visible in the protosyllable stage, and for later song learning stages it is gradually shifting right toward larger values of interspike intervals. That reflects the increasing complexity of the song, which incorporates new syllable types and therefore decreases the frequency of the repetition of the same sound. Based on bimodal nature of ISIs distributions, it is natural to define a burst using a maximal ISI of the burst mode. Thus, we follow the procedure in the original paper, and define a burst as a continuous group of spikes separated by interspike intervals of no more than 30 ms (since  $\log_{10}(30) \sim 1.5$ ).

### 4.1.3 Burst tightness

Spike patterns of projection neurons during song development vary significantly in the number of spikes produced per burst and in the burst duration. We therefore use first interspike interval in the burst as a measure of burst tightness (see Fig. 4.4A). First interspike intervals of individual neurons across many bursts demonstrate wide

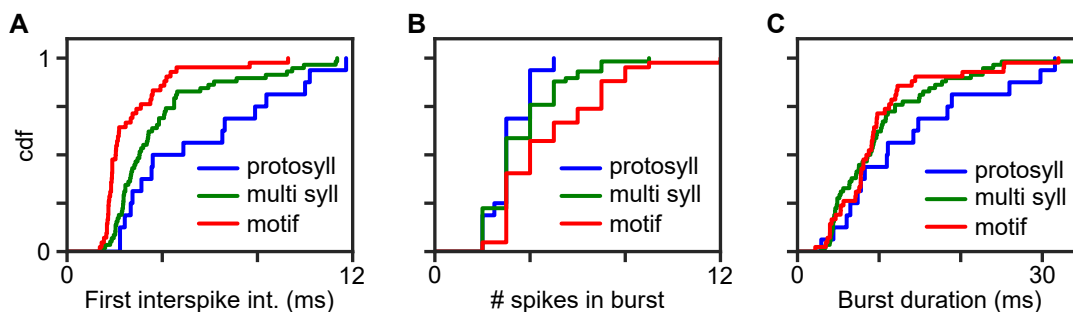


**Figure 4.5.** Maturation of spike properties of HVC-RA neurons. Cumulative density functions for first interspike interval (A), number of spikes in burst (B), and burst duration (C) of HVC-RA neurons at different stages of song learning. First interspike intervals progressively tighten during vocal development. Burst durations slightly decrease, but the decrease is not statistically significant ( $p = 0.08$ ). Number of spikes in burst does not change.

distributions with some outliers (see Fig. 4.4B). Therefore, we use a median first interspike interval, rather than the mean, to get a more robust estimate of first interspike interval. In addition to the burst tightness, we also estimate other spike properties: number of spikes in a burst and burst duration. For both of these measures, we again use a median value to get a robust estimate. We observe that bursts in the HVC-RA neuron population gradually tighten as the song progresses through the protosyllable, multi-syllable and motif stages (see Fig. 4.5, multi-syllable versus protosyllable,  $p = 0.023$ , one-sided Wilcoxon rank sum test; motif versus multi-syllable,  $p < 0.0001$ , one-sided Wilcoxon rank sum test), supporting that burst tightness is positively linked to song development and presumably to HVC-RA neuron maturation. Neither the number of spikes in a burst, nor the burst duration changes significantly (though burst duration in multi-syllable stage is slightly smaller than in the protosyllable stage with statistical significance of  $p = 0.08$ , one-sided Wilcoxon rank sum test).

#### 4.1.4 Syllable locking

We next wonder if burst tightness of HVC-RA neurons depends on the time when they fire in syllables. We follow the procedure in the original paper, and define syllable locked HVC-RA neurons, i.e., those that tend to burst at fixed latency relative to the syllable onset time. To find syllable locking time, spikes of the neurons in each recording are aligned to the syllable onset times (between -500 ms and 500 ms) (see Fig. 4.6A). Then, the largest peak in firing rate between -50 ms to 200 ms from syllable onsets is selected as a candidate locking time. Significance of the locking time is determined by bootstrapping 1,000 samples of spike trains, which is done by shifting spikes in the individual recordings

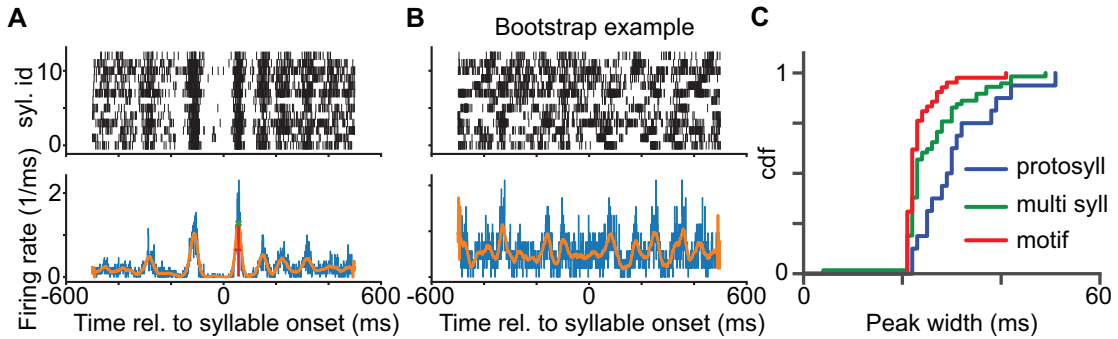


**Figure 4.6.** Syllable locking and peak width in syllable locking firing rate. (A) Top: An example of spikes of one HVC-RA neuron in protosyllable stage aligned to onset times of different syllables. Bottom: Corresponding raw firing rate (blue) and smoothed firing rate (orange). To find syllable locking time, the peak in smoothed firing rate is selected between -50 ms and 200 ms (green cross). Peak significance and width are shown with red vertical and horizontal lines correspondingly. (B) An example of bootstrap spike sample for spikes in (A), used to estimate the significance of syllable locking. (C) Cumulative density function for peak width at different stages of song learning shows progressive peak width tightening.

randomly, preserving inter-spike intervals (see Fig. 4.6B). The neuron is defined as syllable locked if the peak in original firing rate is larger than the peaks in 95% of bootstrapped samples (i.e.  $p$ -value 0.05).

We also estimate the peak width in syllable locking firing rate. The peak width is evaluated at the half height of the peak’s prominence, which we will define later. At the evaluation height, a horizontal line is drawn to both sides, starting at the peak’s current horizontal position, until it crosses the signal, and the distance between the endpoints is defined as the peak’s width. To calculate the peak prominence, first, a horizontal line from the peak is extended to the left and right until the line intersects the signal again at the slope of a higher peak or the line reaches the time boundaries. On each side, the minimal signal value is found within the interval defined above. These points are the peak’s bases. The higher one of the two bases marks the peak’s lowest contour line. The prominence is then calculated as the vertical difference between the peak’s height and its lowest contour line.

The peak width provides an estimate of both the neuron precision and the burst duration. Indeed, a wide peak in syllable locking firing rate may arise either due to poor alignment of spikes produced in different repetitions of the same syllable, or due to long bursts. We observe that peak width in the HVC-RA neuron population gradually tightens as the song progresses through the protosyllable, multi-syllable and motif stages (see Fig. 4.6C, multi-syllable versus protosyllable,  $p = 0.004$ , one-sided Wilcoxon rank sum

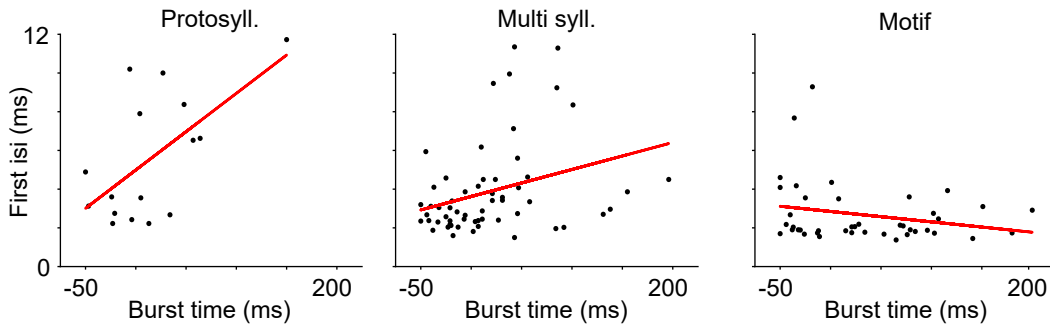


**Figure 4.7.** Burst tightness and latency of HVC-RA neurons at different stages of vocal development. In the protosyllable stage, bursts are tighter for neurons with small burst latency, those that fire near the syllable onset time. The same trend is visible in the multi-syllable stage, but disappears in the motif stage.

test; motif versus multi-syllable,  $p < 0.006$ , one-sided Wilcoxon rank sum test). Since the burst duration of HVC-RA neurons doesn't change much during vocal development, we treat this observation as an evidence for the increasing neuronal precision in spike times. The peak width is also correlated with first interspike interval, suggesting that both measures can be used to evaluate neuron immaturity ( $p < 10^{-16}$ , two-tailed t-test).

In the protosyllable stage (see Fig. 4.7), the first interspike interval significantly increases with the burst latency ( $p = 0.012$ , two-tailed t-test), suggesting that bursts are tighter for neurons bursting at the start of the syllables than those at the end. Thus, the maturity of HVC-RA neurons is heterogeneous in this stage, and immature neurons tend to burst towards the end of the syllables. This trend is less pronounced but still significant in the multi-syllable stage ( $p = 0.017$ , two-tailed t-test). It disappears in the motif stage ( $p = 0.14$ , two-tailed t-test).

### 4.1.5 Spike width

We next wonder if there are any changes in spike width during development. Immature neurons throughout multiple brain regions commonly show wider spikes due to smaller sodium and potassium conductance. The spikes become narrower during development, when additional ionic channels are added into the membrane. To find spike width of a neuron, for each recording we extract membrane potential traces in time window extending from 1 ms before to 1 ms after labeled spike times. Next, we find the maximal voltage in this time interval and define a spike half-height as the difference between the maximal voltage and the mean voltage of the neuron in this recording. Finally, we extend a horizontal line to the left and right at the half-spike height starting from the position

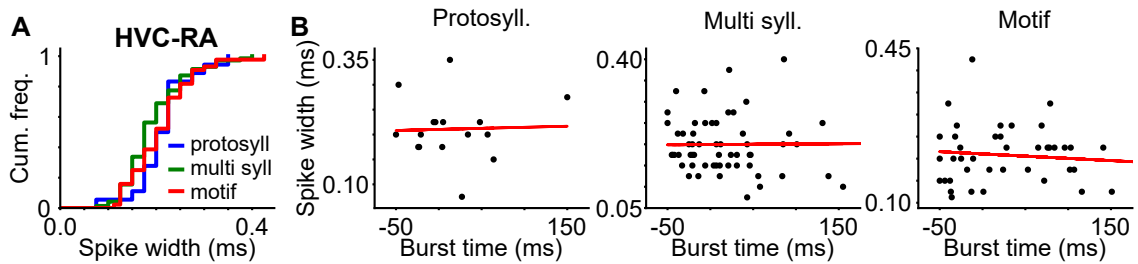


**Figure 4.8.** Spike width of HVC-RA neurons does not change during vocal development. (A) Cumulative density functions for spike width at different stages of song learning. (B) Spike width of syllable locked neurons does not depend on syllable locking time at any stage of song learning

of the maximal voltage, and define a spike width as the temporal difference between intersection points with the voltage trace. If the maximal voltage occurs at the distance of more than 0.5 ms from the spike time, or one of the intersections does not occur within the extracted time interval, the spike is ignored. A spike width of a neuron is estimated as the median spike width of all its valid spikes.

We observe that spike width of HVC-RA neurons does not change significantly during development (see Fig. 4.8A). In addition, spike width does not show significant correlation with syllable locking time at all stages of song learning (see Fig. 4.8B). This may reflect that recorded immature neurons already have well-developed sodium and potassium ionic channels to produce spikes.

#### 4.1.6 HVC-X neurons

What about spike properties of HVC-X neurons? As in the case of HVC-RA neurons, first interspike intervals of HVC-X show gradual tightening during song learning (see Fig. 4.9, multi-syllable versus protosyllable,  $p < 10^{-6}$ , one-sided Wilcoxon rank sum test; motif versus multi-syllable,  $p < 10^{-11}$ , one-sided Wilcoxon rank sum test). Burst duration decreases slightly in multi-syllable stage compared to protosyllable stage ( $p = 0.016$ , one-sided Wilcoxon rank sum test). Peak width also shows progressive tightening during vocal development (multi-syllable versus protosyllable,  $p < 10^{-5}$ , one-sided Wilcoxon rank sum test; motif versus multi-syllable,  $p < 10^{-4}$ , one-sided Wilcoxon rank sum test). Number of spikes in a burst does not change significantly.

Like HVC-RA neurons, HVC-X in the protosyllable stage demonstrate a significant increase of the first interspike interval with the burst latency (see Fig. 4.10,  $p < 10^{-4}$ , two-tailed t-test). In the multi syllable stage, the first spike interval does not change ( $p = 0.94$ ), and in the motif stage it even shows a small, but statistically significant

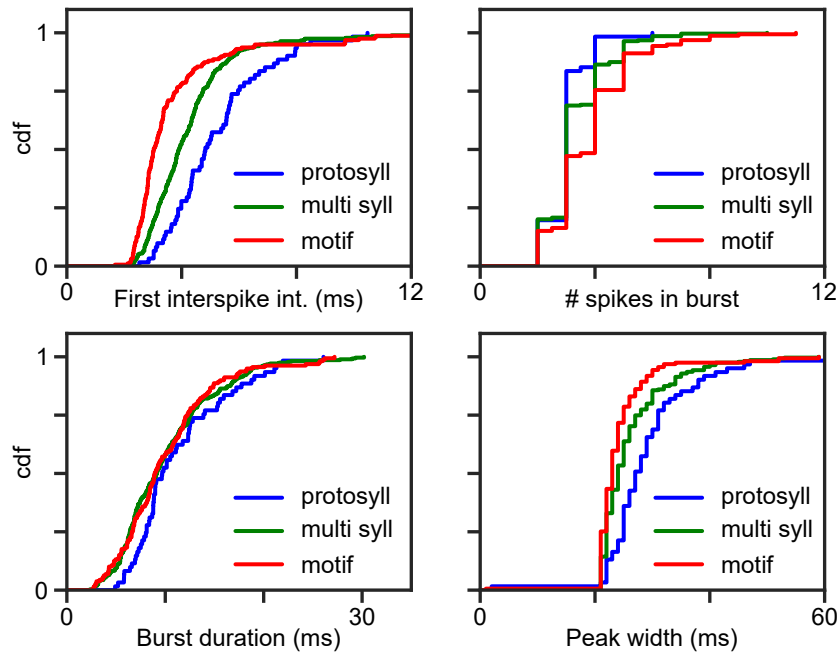


**Figure 4.9.** Maturation of spike properties of HVC-X neurons. Cumulative density functions for first interspike interval, number of spikes in burst, burst duration, and peak width in syllable locking firing rate of HVC-X neurons at different stages of song learning. First interspike intervals progressively tighten during vocal development. Peak width also tightens and burst duration slightly decreases. Number of spikes in burst does not change.

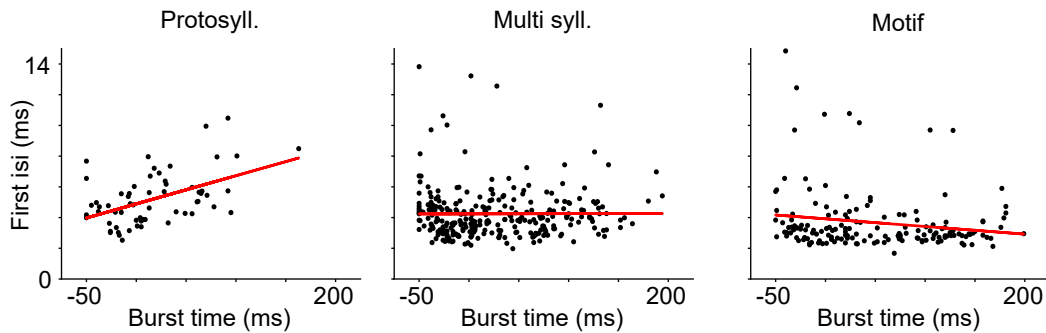


**Figure 4.10.** Burst tightness and latency of HVC-X neurons at different stages of vocal development. In the protosyllable stage, bursts are tighter for neurons with small burst latency, those that fire near the syllable onset time. The trend disappears in the multi-syllable and motif stages.

decrease ( $p = 0.03$ ). We believe that the latter trend is an artifact created by the outliers that have large first interspike interval, but burst close to the syllable onset time.

Spike width of HVC-X neurons also does not change significantly during development (see Fig. 4.11A) and there is no correlation between syllable locking time and spike width at any vocal development stage (see Fig. 4.11B).

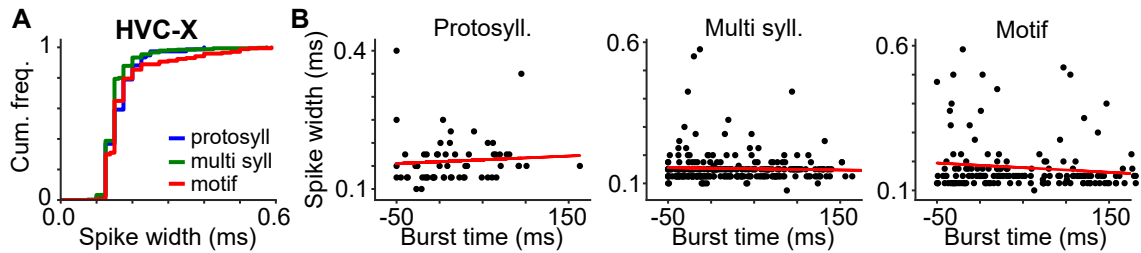


**Figure 4.11.** Spike width of HVC-X neurons does not change during vocal development. (A) Cumulative density functions for spike width at different stages of song learning. (B) Spike width of syllable locked neurons does not depend on syllable locking time at any stage of song learning

Overall, we observe that spike properties of HVC-X neurons during song learning demonstrate similar trends to spike properties of HVC-RA neurons. It is unclear if these observations reflect the possible progressive maturation of HVC-X neurons. One hypothesis is that HVC-RA neurons, known to send numerous connections to HVC-X, shape the spike pattern of HVC-X neurons during the song. Thus, the tightening of the spike pattern of HVC-RA neurons leads to the tightening of the spike pattern in HVC-X neurons.

#### 4.1.7 Spike patterns during and outside song bouts

To address this question, we compare spike patterns of HVC-X neurons during song bouts, when they are presumably driven by activity of HVC-RA neurons, with spike patterns outside song bouts, which should reflect the intrinsic properties of HVC-X. Following Okubo et al., we define a song bout as a continuous syllable sequence separated by silent gaps of more than 300 ms. Note, that calls and introductory notes are not considered to be syllables. For each HVC-X neuron we classify its bursts into two categories: during song bout; and outside song bout. A burst during song bout has all its spikes between 100 ms before song bout onset and 100 ms after song bout offset time. Bursts that do not occur during song bout were treated as bursts outside song bout. At all stages of vocal development, first interspike intervals of the bursts produced outside song bouts are larger than those of the bursts during the song (see Fig. 4.12). It suggests that spike patterns of HVC-X neurons are indeed affected by HVC activity.

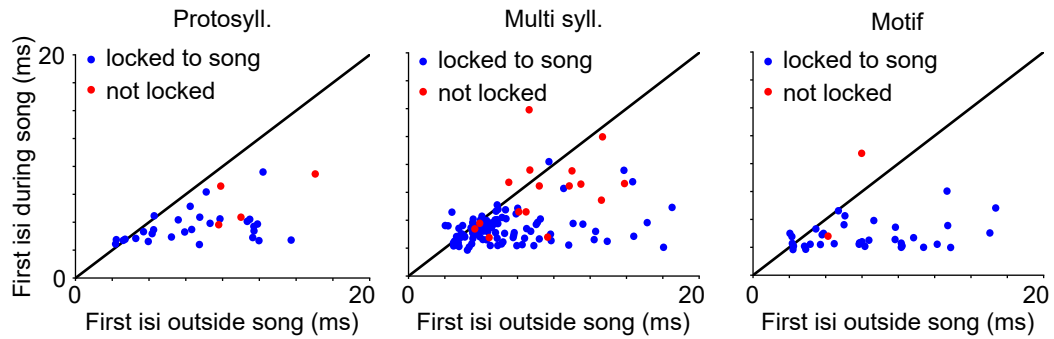


**Figure 4.12.** Comparison of first interspike intervals of the bursts of HVC-X neurons produced during and outside song bouts at protosyllable, multi syllable and motif stages. At all stages, bursts produced outside the song are less tight, suggesting that burst tightening of HVC-X neurons is a network driven phenomena.

### 4.1.8 Conclusions

To conclude, we interpret the less tightness of bursts of HVC-RA neurons as a reflection of immature intrinsic bursting mechanism. An alternative possibility is that the burst tightness is a network phenomenon. It is possible that neurons that burst earlier in the sequence are better connected and get stronger inputs, leading to tight bursts, whereas those that burst later are still in process of getting incorporated and hence are loosely connected. Another possible is that feedback inhibition controls the burst tightness [105]. There is some evidence in the data that supports the intrinsic mechanism of burst tightness. We found one HVC-RA neuron in the subsong stage that was not locked to vocalization but still showed tight bursts usually observed in the motif stage (see Fig. 4.13). Since the network is unlikely formed in this stage, the observation favors intrinsic mechanism for burst tightness. Due to limited number of HVC-RA neurons recorded in subsong stage and subsequent protosyllable stage, we could not gather more evidence. Future experiments with more data on HVC-RA neurons in early song learning stages, perhaps also including intracellular recordings *in vivo* and in slices, should be able to address whether burst tightness is intrinsically controlled.

## 4.2 Computational model for sequence formation

In this section we describe a computational model that explores the role of immature neurons in the sequence formation in HVC. Inspired by the results outlined in the previous section, we create a maturation model of HVC-RA neurons, according to which burst tightness is an intrinsic neuronal property that emerges through development. Immature

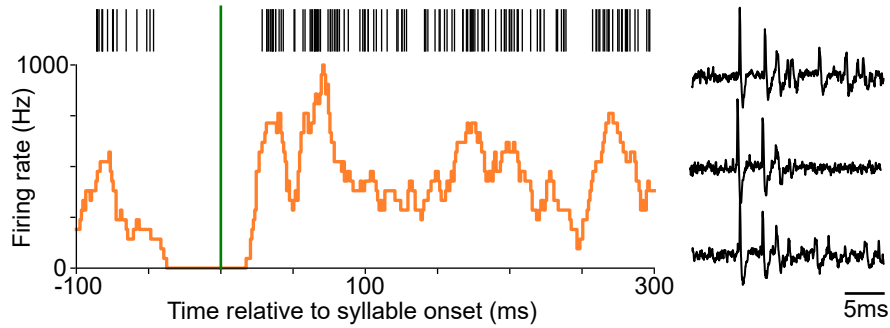


**Figure 4.13.** Example HVC-RA neuron recorded in the subsong stage showing tight burst without being locked to the song. (Left) Firing rate of the neuron aligned to syllable onset times does not show significant peak, meaning that the neuron is not locked to the syllables. (Right) Example membrane potential traces of the same neuron demonstrate tight bursting pattern

HVC-RA produce wide bursts, which gradually become tighter due to spontaneous activity and reliable spiking. In addition, immature HVC-RA neurons have a higher resting potential which makes them more spontaneously active.

We build upon the gradual sequence formation model [100, 101] and use similar synaptic plasticity rules to grow the network of connected HVC-RA neurons. Higher spontaneous activity of immature neurons makes them prime targets for recruitment and they are incorporated to the end of the growing feedforward sequence. After incorporation into the network, these neurons are more consistently active and mature fast, forming a new edge of growth that leads to recruitment of a new cohort of immature neurons. Thus, the network growth, organized in separate trials, progresses gradually by neuron-by-neuron recruitment. The network also assembles according to the birth order of neurons, with earlier born neurons having smaller burst times.

### 4.2.1 Neuronal spatial arrangement

We start by setting up spatial distributions of neurons. As in the previous chapter, we model two main populations of neurons: HVC-RA and HVC-I (interneurons). While real HVC contains around 20,000 HVC-RA and 5,500 interneurons, due to the limitation of computational power we could not include this many neurons in our model. Instead, we use 2000 HVC-RA and 550 HVC-I neurons.

Since number of neurons is small, distributing them in 3D space becomes problematic because a large portion of them will be at the edge. Later we set up connections between the neurons based on the distances between them, thus the edge neurons will receive

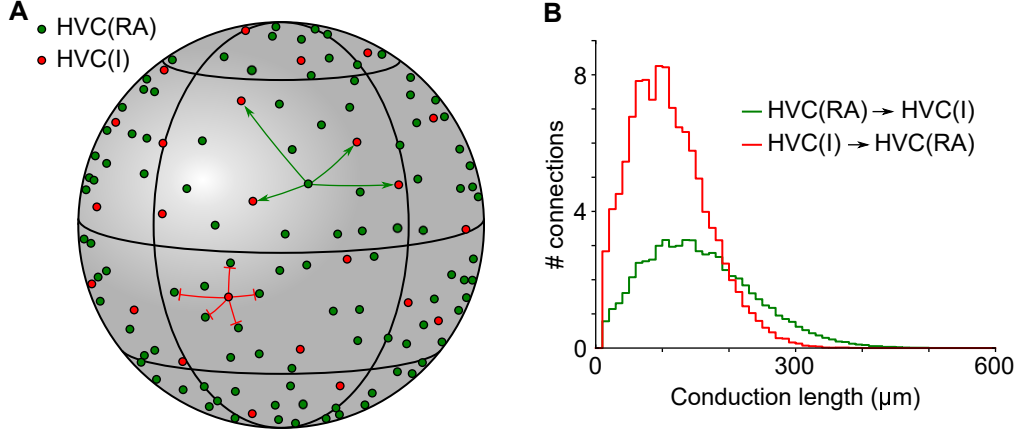


**Figure 4.14.** Schematic of a network arrangement and connectivity. (A) HVC-RA (dark green circles) and HVC-I (red circles) neurons are distributed over the surface of a sphere. HVC-I neurons form a lattice-like pattern, while HVC-RA neurons are distributed uniformly. Examples of connections from one HVC-RA neuron to HVC-I neurons and from one HVC-I to HVC-RA neurons are shown. (B) Distribution of axonal conduction lengths for connections between HVC-RA and HVC-I neurons.

less inhibition and will be preferentially recruited by the network growth algorithm. To avoid this boundary effect, we place neurons on a 2D sphere of radius  $260 \mu\text{m}$  (see Fig. 4.14A). Each neuron occupies a volume of a sphere with diameter  $10 \mu\text{m}$  and we do not allow overlaps between any neurons. HVC-I neurons are first placed evenly on the sphere using the Fibonacci lattice [106]. The distance between nearest neighbors on sphere is approximately  $\Delta r_{in} = 40 \mu\text{m}$ , which matches the average distance between HVC-I in real HVC ( $\Delta r_{in} = \sqrt[3]{V_{HVC}/N_I}$ , where  $V_{HVC} = 0.26 \text{ mm}^3$  is the volume of HVC and  $N_I = 5,500$  is the number of HVC-I neurons). To create randomness in the positions of HVC-I neurons, their latitude and longitude are shifted by a small amount randomly sampled between 0 and  $\Delta\theta$  and between 0 and  $\Delta\phi$  correspondingly, with  $\Delta\theta = 0.0006 \Delta r_{in}$  and  $\Delta\phi = 0.0006 \Delta r_{in}/\sin(\theta)$ . It corresponds to a random shift of a neuron between 0 and  $\sim 2 \mu\text{m}$  along the surface of the sphere. Next, HVC-RA neurons are placed randomly over the sphere surface, with the constraint that they do not overlap with other HVC-RA and HVC-I neurons.

## 4.2.2 Neuronal connectivity

We create connections between HVC-RA and HVC-I neurons probabilistically according to the Gaussian distributions based on the distance between the neurons on the sphere (see Fig. 4.14B). Specifically,  $p_{RA \rightarrow I} = \exp(-d^2/\sigma_{RA \rightarrow I}^2)$  and  $p_{I \rightarrow RA} = \exp(-d^2/\sigma_{I \rightarrow RA}^2)$ , where  $p_{RA \rightarrow I}$  is a probability for a given HVC-RA neuron to contact a given HVC-I

neuron,  $p_{I \rightarrow RA}$  is a probability for a given HVC-I neuron to contact a given HVC-RA neuron,  $d$  is a distance between given HVC-RA and HVC-I neurons on the sphere,  $\sigma_{RA \rightarrow I} = 130 \mu m$ , and  $\sigma_{I \rightarrow RA} = 90 \mu m$ . Only a single connection between a pair of neurons is allowed. Parameter  $\sigma_{RA \rightarrow I}$  is chosen to match the upper bound on the number of postsynaptic HVC-I partners for an HVC-RA neuron [50,89]. On average an HVC-RA neuron contacts 11.6% of HVC-I neurons, which corresponds to 65 HVC-I, with mean distance 155  $\mu m$ . HVC-I neurons has a smaller spatial connectivity scale to influence nearby HVC-RA neurons. A single HVC-I neuron contacts 5.8% of HVC-RA neurons, which corresponds to 115 HVC-RA neurons, with mean distance 110  $\mu m$ . The spatial synaptic distributions are similar to those observed in experiments [50] (also see Chapter 3). Initially, all HVC-RA neurons are immature and there are no connections between them.

We also create axonal time delays between all neurons by setting a conduction velocity to 100  $\mu m/ms$ , unless otherwise stated, and using distances between neurons on the sphere. This value of conduction velocity creates realistic axonal delays between neurons.

### 4.2.3 Neuron model

Dynamics of HVC-I neurons is simulated with Dormand-Prince 8th order numerical method and dynamics of HVC-RA neurons with AN3D1 3rd weak order method with time resolution 0.02 ms (see Chapter 2 for more details). For HVC-I neurons, we use the model identical to the one described in Chapter 2.

For HVC-RA neurons, we create a maturation model to account for the changes in burst tightness during development. We start with a model for mature neurons and take a 2-compartmental Hodgkin-Huxley neuron model with soma and dendrite described in Chapter 2. We hypothesize that dendrites of immature HVC-RA neurons are not fully developed and cannot support a strong calcium spike. To reflect 'weak' dendritic compartment of immature neurons, we set their calcium dendritic conductance to zero. Thus, immature neurons are not able to generate tight bursts (see Fig. 4.15B,D). In addition, we set both somatic and dendritic leak reversal potential for immature neurons 15 mV higher, since it is universally observed that resting membrane potential of immature neurons is elevated compared to those of mature neurons. This leads to increased excitability of immature neurons, i.e., smaller input could make them fire action potential (see Fig. 4.15A). To make a transition from immature neuron model to mature, we introduce a time-dependent maturation. Both the resting membrane potential and the calcium conductance exponentially approach their mature values with

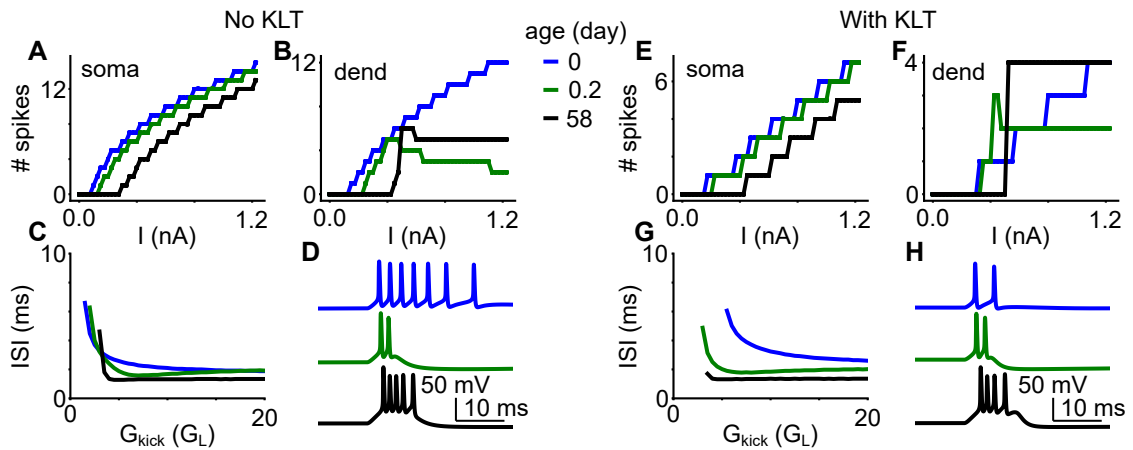


**Figure 4.15.** Comparison of maturation models with (A-D) and without (E-H) low-threshold potassium current (KLT) for HVC-RA neurons of different age. The model with KLT is selected as the most consistent with experimental observations. Neurons of age 0 days are called immature. Neurons of age 58 days are called mature. Immature neurons in both models have no dendritic calcium channels. Resting potential of immature neurons with KLT (without KLT) is 15 mV (25 mV) higher than for corresponding mature neurons. Both the resting potential and the dendritic calcium conductance approach mature values exponentially in age-dependent manner with time scale 50,000 s. Number of somatic spikes produced under external current pulse of 150 ms duration injected to soma (A,E) and dendrite (B,F). Model with KLT produces less somatic spikes and shows the same excitability of dendritic compartment for both immature and mature neuron models. (C,G) First interspike intervals of bursts elicited by an external excitatory conductance kick delivered to dendritic compartment. The difference in burst tightness between mature and immature models is more pronounced for the model with KLT (G). (D,H) Examples of membrane potential traces for neurons of different age produced by the same strength of excitatory conductance kick ( $G_{kick} = 15 G_L$ ). During maturation, bursts in model with KLT (H) become tighter and acquire more somatic spikes.

time constant 50,000 s. Due to maturation, newborn immature neurons gradually become less excitable (see Fig. 4.15A) and develop strong calcium burst (see Fig. 4.15B). The model, however, suffers from biasing immature neurons to produce considerably more somatic spikes compared to mature neurons under the same strength of input (see Fig. 4.15D). Burst tightness, measured by the first interspike interval in burst, also does not change significantly during development (see Fig. 4.15C).

These issues motivate us to modify the neuron model. We first reason that we need a stronger hyperpolarizing current to decrease the number of spikes produced by immature neurons. The simplest way to achieve that is to increase the strength of leak conductance. Thus, we systematically vary the leak conductance in somatic and dendritic compartments (see Fig. 4.16). Strong leak conductance is successful in reducing the number of somatic spikes produced by immature neurons (see Fig. 4.16A,B). However, it

also decreases the number of spikes produced in bursts of mature HVC-RA and require a much stronger input to elicit the burst (see Fig. 4.16F). Moreover, while larger leak conductance increases the first interspike intervals for immature neurons (see Fig. 4.16C), it affects mature neurons in the similar way (see Fig. 4.16G). Therefore, we conclude that adjusting the strength of leak conductance affects both mature and immature neuron models similarly, and is not able to produce the desired differences between them.

Delay-rectified potassium current is the last remaining hyperpolarizing current in the somatic compartment. However, this current is responsible for the action potential shape and changes in its strength affect the spike width. Since the spike width stays the same during development according to our results in the previous section, developmental changes in delay-rectified potassium current are inconsistent with experimental observations. Moreover, this current has a small sub-millisecond scale activation time and cannot significantly affect the size of interspike intervals.

Therefore, we incorporate an additional hyperpolarizing current with large activation time scale:  $I_{KLT} = G_{s,KLT} l (V_s - E_K)$  with conductance  $G_{s,KLT}$ , potassium reversal potential  $E_K = -90 \text{ mV}$  and gating variable  $l$ . Gating variable obeys the following dynamics:  $\tau_l dl/dt = l_\infty(V) - l$ , where  $\tau_l = 10 \text{ ms}$ ,  $l_\infty(V) = 1/(1 + \exp -(V + 40)/5)$ . Introduction of KLT current also allows us to use more elevated resting potential for immature neurons (25 mV higher than for mature neurons), which further increases their excitability. Similar current was used by Jin et al. [107] to achieve strong spike frequency adaptation. In our case, it serves a different role. Large conductance of KLT current decreases the number of somatic spikes produced in both immature and mature HVC-RA neuron models (see Fig. 4.17A,B,D,E,F,H). However, the input needed to produce a dendritic burst in mature neurons is not affected by this current (see Fig. 4.17F). Moreover, while larger KLT current increases the first interspike intervals in immature neurons (see Fig. 4.17C), it does not change the burst tightness of mature neurons (see Fig. 4.17G). This is because KLT current has a relatively large activation time scale of 10 ms, and is not able to affect first spikes of mature neurons driven by a strong calcium spike in dendritic compartment. It is, however, affecting the overall number of spikes produced in burst, since the burst duration is similar to the activation time scale. In contrast, immature neurons have a weak dendritic compartment, and KLT current is strong enough to influence both the first and the last spikes in the burst.

The response and spike properties of the final model with  $G_{KLT} = 3.5 \text{ mS/cm}^2$  are shown in Fig. 4.15E-H. Compared to the model without KLT, the number of produced somatic spikes (see Fig. 4.15A,B,D,E,F,H) is reduced and difference in burst tightness

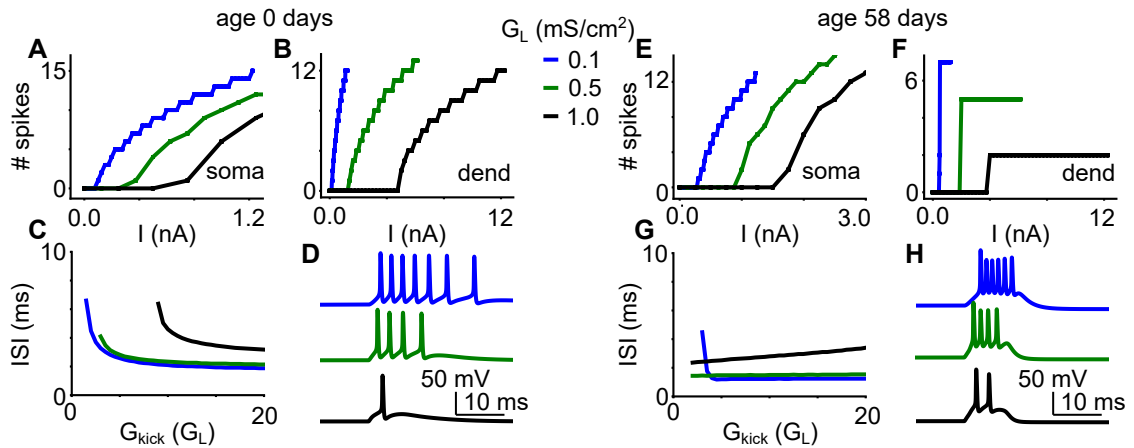


**Figure 4.16.** Maturation model with adjusted leak membrane conductance for immature (A-D, day 0) and mature (E-H, day 58) neuron models (no KLT conductance). Number of somatic spikes produced under external current pulse of 150 ms duration injected to soma (A,E) and dendrite (B,F). Excitability of dendritic and somatic compartments of both immature and mature neurons is decreased for large leak conductance. (C,G) First interspike intervals of bursts elicited by an external excitatory conductance kick delivered to dendritic compartment. Bursts of both immature and mature neuron models become less tight when leak conductance increases. (D,H) Examples of membrane potential traces for neurons of different age produced by the same strength of excitatory conductance kick ( $G_{kick} = 15 G_L$ ). Large leak conductance reduces the number of somatic spikes produced and spreads them out, creating bigger interspike intervals. Overall, adjusting the strength of leak conductance affects both mature and immature neuron models similarly, and is not able to produce the desired differences between them.

between immature and mature neuron models is more pronounced (see Fig. 4.15C,G).

Thus, incorporation of an additional KLT current makes neuron maturation model more consistent with experimental observations. KLT conductance has been observed in many neuron types and may also be present in HVC-RA neurons. Further experiments with intracellular recordings of HVC projection neurons are needed to test this hypothesis.

In the simulation, both mature and immature HVC-RA neurons receive white noise injections with amplitude 0.1 nA to soma compartment and amplitude 0.2 nA to dendrite. It results in immature HVC-RA neurons firing spontaneously at frequency  $\sim 0.6$  Hz. Spontaneous activity decreases with age, practically disappearing in mature neurons (see Fig. 4.18). Noise model for HVC-I neurons is identical to the one described in Chapter 2. HVC-I neuron spikes spontaneously with frequency  $\sim 10$  Hz.

#### 4.2.4 Maturation dynamics

As described in the previous section, maturation of HVC-RA neurons is modeled as a gradual increase of dendritic calcium conductance, and a gradual decrease in the somatic

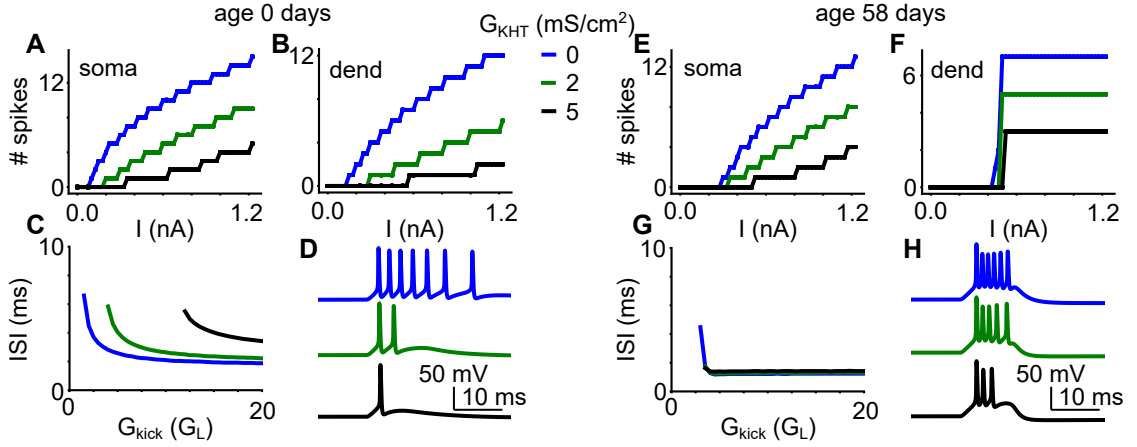


**Figure 4.17.** Maturation model with different strength of low-threshold potassium (KLT) current for immature (A-D, day 0) and mature (E-H, day 58) neuron models. Number of somatic spikes produced under external current pulse of 150 ms duration injected to soma (A,E) and dendrite (B,F). Excitability of dendritic compartment of mature neurons does not depend on the KLT conductance. (C,G) First interspike intervals of bursts elicited by an external excitatory conductance kick delivered to dendritic compartment. Bursts of immature neurons become less tight for strong KLT current, while burst tightness of mature neurons is not affected by the strength of KLT. (D,H) Examples of membrane potential traces for neurons of different age produced by the same strength of excitatory conductance kick ( $G_{kick} = 15G_L$ ). Large KLT conductance reduces the number of somatic spikes produced and spreads out the spikes of immature neurons, creating bigger interspike intervals. Thus, incorporation of an additional KLT current makes neuron maturation model more consistent with experimental observations.

and dendritic leak reversal potential (see Fig. 4.19A,B):

$$\tau_{mat} \frac{dG_{Ca}}{dt} = G_{mat} - G_{Ca},$$

$$\tau_{mat} \frac{dE_L}{dt} = E_{mat} - E_L,$$

where  $\tau_{mat}$  is the maturation time constant;  $G_{mat} = 55 \text{ mS/cm}^2$  is the mature value of calcium conductance; and  $E_{mat} = -80 \text{ mV}$  is the mature value of leak reversal potential. Values of  $G_{Ca}$  and  $E_L$  are updated at the end of each trial.

In addition to the age-dependent maturation with time constant  $\tau_{mat} = 50,000 \text{ s}$ , we incorporate activity-driven maturation (see Fig. 4.19C). The neuron is called reliably spiking if it spiked in more than half of the trials in the past 1,000 trials. Neurons become reliably spiking after recruitment into the network and their maturation progresses with a smaller time constant  $\tau_{mat} = 500 \text{ s}$ . This acceleration protects the grown network from spontaneous activation and hence from formation of loops. The activity-dependent

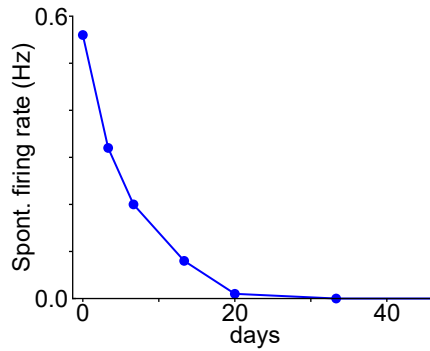


**Figure 4.18.** Spontaneous firing rate of HVC-RA neuron decreases with neuronal age due to gradual lowering of resting potential.

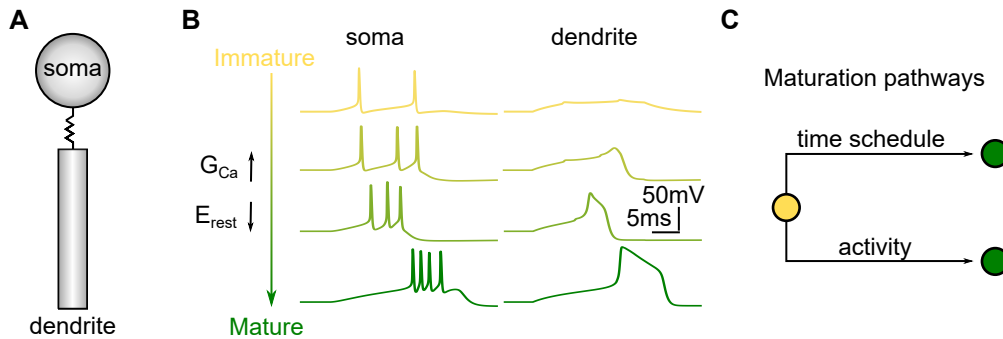


**Figure 4.19.** Computational model of HVC-RA neurons and the maturation process. (A) An HVC-RA neuron is modeled as two-compartmental Hodgkin-Huxley with soma and dendrite. (B) HVC-RA responses to the current injection to the dendrital compartment at different maturation stages. (C) Two pathways for neuronal maturation: scheduled maturation under spontaneous activity, and accelerated maturation driven by activity when neuron spikes reliably.

maturation dynamics is inspired by the observation in rodent hippocampus that adult-born neurons mature faster with enhanced activity and mature more slowly with reduced activity [108]. The exact value of the activity-driven maturation time scale is not important, as long as it is much smaller than the spontaneous one.

### 4.2.5 Neuronal turnover

Due to maturation dynamics, spontaneous activity of neurons gradually decreases with time. Therefore, the neurons that do not get incorporated into the network become silent and lose any opportunity to get recruited. Specifically, neuron is assigned as silent if it spiked in less than 80 trials in the past 4,000 trials. To model the neurogenesis in HVC, silent neurons are replaced at the end of each trial with immature neurons. New immature neurons are placed randomly on the surface of the sphere representing HVC,

avoiding overlaps with all HVC-RA and HVC-I neurons. Therefore, the neurogenesis in the model provides a continuous supply of immature neurons with high chances for recruitment, while removing silent "useless" neurons.

### 4.2.6 Synaptic plasticity rules

To grow a network of connected HVC-RA neurons, we use a combination of a Hebbian-like burst-timing dependent plasticity (BTDP) (Fig. 4.20A) and two additional plasticity rules for HVC-RA neurons - axon remodeling and potentiation decay, which are similar to those used in the previous models for growth of synaptic chain networks [100, 101].

To update weights between HVC-RA neurons, we use a BTDP rule based on burst onset timing between presynaptic and postsynaptic neurons (Fig. 4.20A). We define a "burst" as a continuous group of spikes with duration 30 ms or less. Burst onset time is defined as the first spike in a burst. Each time a neuron produces a new burst, all afferent synapses onto the neuron and all efferent synapses are updated. For a pair of a presynaptic neuron  $i$  with burst onset time  $t_i$  and a postsynaptic neuron  $j$  with burst onset time  $t_j$ , an additive LTP would occur for the synapse with weight  $G_{ij}$  if  $\Delta t = t_j - t_i > T_0$ :

$$G_{ij} \rightarrow G_{ij} + \begin{cases} A_P(\Delta t - T_0)/T_P, & \text{if } \Delta t < T_0 + T_P, \\ A_P \exp(-(\Delta t - T_0 - T_P)/\tau_P), & \text{if } \Delta t \geq T_0 + T_P. \end{cases}$$

If  $\Delta t \leq T_0$ , the synapse undergoes depression through multiplicative LTD:

$$G_{ij} \rightarrow G_{ij} - \begin{cases} A_D G_{ij}(T_0 - \Delta t)/T_D, & \text{if } \Delta t > T_0 - T_D, \\ A_D G_{ij} \exp((\Delta t - T_0 + T_D)/\tau_D), & \text{if } \Delta t \leq T_0 - T_D, \end{cases}$$

The following parameters are used in simulations unless specified:  $A_P = 0.25$  nS,  $A_D = 0.02$ ,  $T_0 = 2$  ms,  $T_P = 3$  ms,  $T_D = 3$  ms,  $\tau_P = 30$  ms,  $\tau_D = 30$  ms. All weights are clipped below  $G_{min} = 0$  nS and above  $G_{max} = 4$  nS.

This simple rule sidesteps the complex interaction of multiple spikes within the bursting pre- and post-synaptic neurons [109], and is guided by the observation that in cortical neurons, the timings of the first spikes in bursts are most important for determining the timing-dependent LTP and LTD [110]. In addition, we apply a small 2 ms shift of BTDP curve to the region of positive times, so that there is an LTD for synchronously bursting neurons. This prevents the emergence of connections between

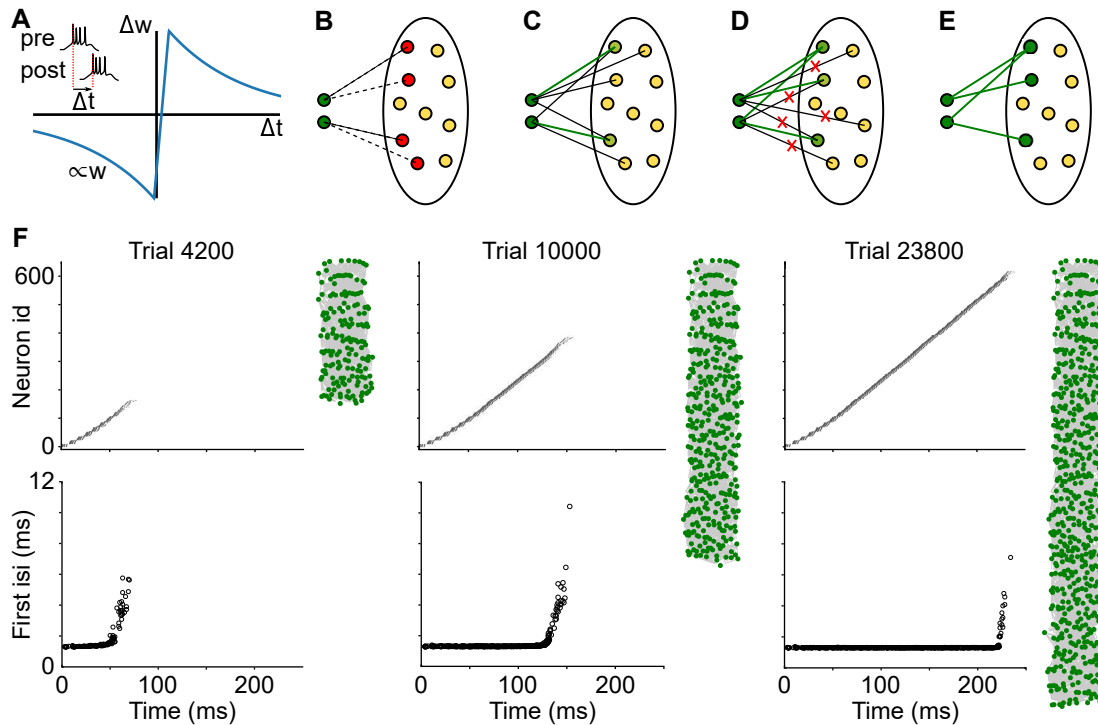


**Figure 4.20.** Mechanism of network growth. (A) Burst-timing dependent plasticity (BTDP) rule is based on the timing between burst onsets of HVC-RA neurons. (B-E) Schematic of recruitment mechanism. (B) Network growth begins with the starter neurons (dark green circles) activated each simulation trial and other HVC-RA neurons being immature (yellow circles). Silent connections (dashed lines) emerge from starter neurons to spontaneously active immature HVC-RA (red circles) according to the BTDP rule. (C) Some silent connections randomly become active (black lines), undergo further strengthening and become strong super connections (thick green lines). (D) When the starter neurons acquire certain number of strong super connections, other weak connections are pruned (red crosses). (E) The recruited neurons (dark green circles) spike reliably after the starter neurons and begin to recruit new neurons to the network. (F) Network growth is a gradual process in which immature HVC-RA neurons are added to the end of the sequence. Network topology (on the right), spike raster plots (top row) and first interspike intervals (bottom row) at different trials of the simulation.

neurons that fire synchronously. Such a shift was used to stabilize weight distributions in random networks of spiking neurons in another modeling study [111]. Whether these rules apply to synaptic plasticity for HVC-RA neurons remains to be seen. To date, there is no systematic study of synaptic plasticity in HVC, and further experiments are needed.

We distinguish three types of connections between HVC-RA neurons, depending on their strength. Silent synapses are weak, nonfunctional connections, with synaptic conductance smaller than a threshold value  $W_a$ . They correspond to the synapses containing only NMDA receptors [112] and do not elicit response in the postsynaptic

neuron. When synaptic strength exceeds  $W_a$ , the synapse becomes active and produces depolarization in the postsynaptic neuron. Strong connections with weight above  $W_s$  are considered as supersynaptic connections. The following parameters are used in simulations unless specified:  $W_a = 0.2$  nS,  $W_s = 1.0$  nS. Regardless of their state, all synapses participate in BTDP update rules.

All synapses experience a depression at the end of each trial, i.e., undergo a potentiation decay:  $G \rightarrow G - \delta$ , where  $\delta = 0.01$  nS. This depression is needed to prevent the emergence of too many active synapses that may lead to uncontrolled network growth. The role of potentiation decay in sequence formation was previously explored in great details by Miller and Jin [101].

The axon remodeling rule is similar to the one in [100]. When the number of efferent supersynaptic connections of a neuron reaches  $N_s = 10$ , the neuron is saturated and all other active efferent connections of the neuron are withdrawn. Withdrawn connections do not elicit effect on postsynaptic neurons and do not participate in BTDP updates. However, they still undergo potentiation decay. Withdrawn connections will be re-connected if the neuron loses one or more of its supersynapses. Limitations on the number of strong outputs prevents neurons from forming too many unspecific connections.

### 4.2.7 Network growth

We randomly select a set of 10 HVC-RA neurons as the training neurons, which form a seed for the network growth. The training neurons are made fully mature with adult values for the resting potential and calcium dendritic conductance. HVC-RA neurons that are not in the training set, called pool neurons, start as immature neurons with high resting potential and devoid of dendritic calcium channels.

The growth consists of separate simulation trials with duration of 500 ms in network dynamics. At each trial, the training neurons are stimulated with a synchronous kick of strong excitatory conductance 300 nS. Due to the elevated resting potential and noise fluctuations in membrane potential, immature pool neurons are spontaneously active during the trials. When pool neurons spike after training neurons, silent connections from training neurons to the pool neurons emerge according to BTDP rules (Fig. 4.20B). During repeating trials, silent synapses stochastically change their strength via LTP and LTD, and randomly become active (Fig. 4.20C). Depolarization of pool neurons provided by the active synapses from the training set biases these neurons to be more active during subsequent trials. Thus, a positive feedback emerges, since activity of pool neurons facilitates strengthening of synapses via LTP, eventually forming supersynaptic

connections. To enforce sparse output connections, we only allow each HVC-RA neuron to make a limited number of supersynaptic connections, which is set to 10 in the model. When a neuron acquires maximal number of supersynaptic outputs, the neuron undergoes axon remodeling where other weak outgoing connections are pruned and do not affect their postsynaptic targets anymore [100, 101] (Fig. 4.20D,E). Limitation on the number of strong outputs creates a competition between pool neurons for the convergent inputs from the training set. When training neurons form the allowed number of supersynaptic connections, their postsynaptic targets are spiking reliably each iteration. The training neurons do not subsequently recruit any more targets. The recruited neurons then act as a new seed for the network growth.

In the model, network grows gradually and neurons are added to the end of the sequence (Fig. 4.20F). Added neurons are initially immature and have less tight burst compared to the neurons already in the sequence. With time and reliable activation, the added neurons mature and develop a tight burst. Thus, we always have immature neurons at the end of the sequence. Sequence keeps growing until all HVC-RA neurons are recruited into the network or its length becomes close to the length of the simulation trial.

### 4.2.8 Axonal conduction velocity and network topology

In our model, the axonal conduction velocity controls the axonal time delays between neurons. With the conduction velocity set to  $100 \mu\text{m}/\text{ms}$ , which creates the realistic axonal time delays observed in HVC [87], the emerged network shows continuous dynamics and nearly uniform temporal distribution of burst onset times (Fig. 4.21A). Established connections between HVC-RA neurons (red curve Fig. 4.21B) are biased towards short delay connections, but are on average longer than the preset connections to HVC-I neurons. Jitter in burst onset times, estimated based on 200 test runs of the grown network, is in sub-millisecond range, reflecting the network precision (Fig. 4.21C). We also explore the network topology of the grown network using supersynaptic weights between neurons and Kamada-Kawai algorithm in Pajek software program for network analysis [113]. The plot of the network topology does not reveal any grouping structure (Fig. 4.21D). These are the characteristics of polychronous chain network proposed as the connectivity of HVC-RA neurons within HVC (see [87] and Chapter 3).

When we repeat the growth with a 10 times faster conduction velocity ( $1000 \mu\text{m}/\text{ms}$ ), the emerged network shows a strongly synchronous activity pattern (Fig. 4.21E). The distribution of axonal delays between HVC-RA neurons in the formed network is similar to

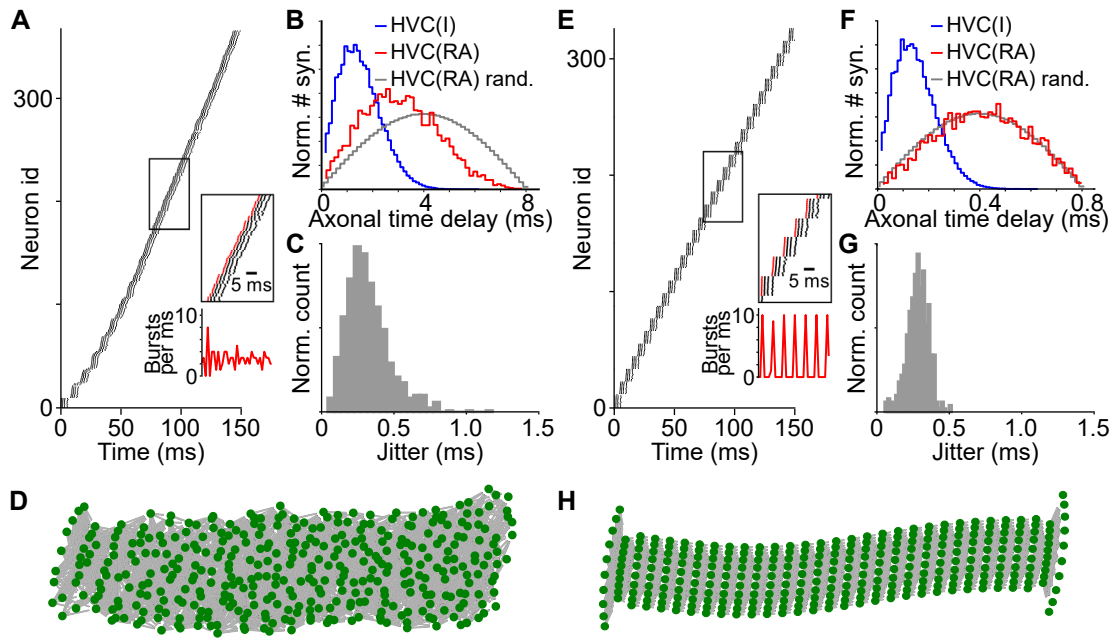


**Figure 4.21.** Example of two grown networks with different axonal conduction velocity. (A-D) Results for a network with conduction velocity  $100 \mu\text{m}/\text{ms}$ , which corresponds to the realistic axonal delays in HVC. (A) Raster plot of the first 150 ms of dynamics shows continuous coverage of burst onset times. (B) Axonal time delay distributions for efferent HVC-RA neuron connections to HVC-I neurons (blue), formed connections to other HVC-RA neurons (red), and random connections to HVC-RA neurons (grey). Emerged connections show decrease in the number of long delay connections compared to the random connections. (C) Jitter in burst onset times of a grown network. (D) Network topology based on the weights between HVC-RA neurons has no apparent groups of neurons (only neurons with burst onset times within first 150 ms are shown). (E-G) Results for a network with 10x faster conduction velocity  $1000 \mu\text{m}/\text{ms}$ , which leads to near zero axonal delays. (E) Network dynamics has prominent synchronous oscillatory activity. (F) No bias towards shorter delay connections is observed in the grown network. (G) Network precision is in sub-millisecond range. (H) Network topology reveals groups of neurons with similar input and output connections, i.e., synfire chain layers.

the delay distribution between randomly selected pairs of HVC-RA neurons (Fig. 4.21F). The network is also temporally precise with the jitter level similar to the polychronous chain network (Fig. 4.21G). Network topology is highly structured, showing groups of neurons with similar input and output connections. In other words, the grown network has a synfire chain topology with prominent oscillatory activity coming from the identical chain layers of neurons.

We systematically vary conduction velocity from 0.5 to 10 times of the value measured in HVC, and observe a sharp transition in burst density oscillations at 1.5, measured as a coefficient of variation in burst density (Fig. 4.22A). Networks with the velocity smaller than this value have a flat burst density, while networks with velocity exceeding

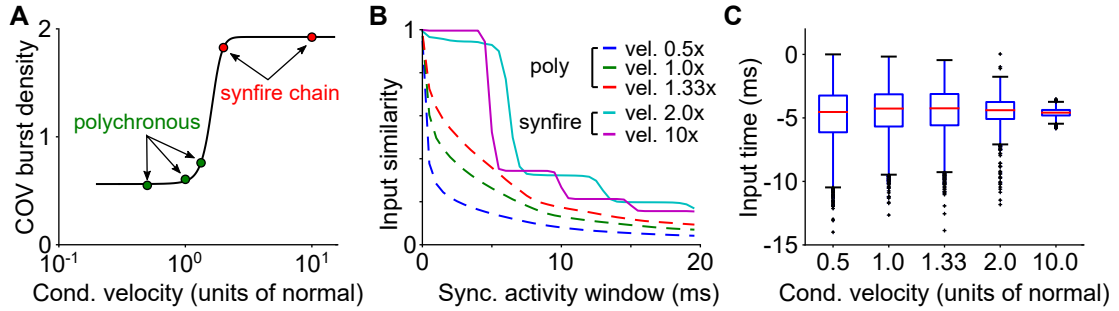


**Figure 4.22.** Conduction velocity shapes network topology. (A) Coefficient of variation of burst onset density shows transition from continuous to discrete activity pattern with change in axonal conduction velocity. (B) Similarity of inputs for neurons bursting within synchronous activity window has plateaus for synfire chain networks and is smooth for continuous networks. (C) Distributions of excitatory input times relative to burst onset time of postsynaptic neurons for different conduction velocities. All networks demonstrate nearly synchronous arrival of inputs.

this value show prominent oscillations.

We further compare the network structures using similarity of input connections for the neurons bursting synchronously in the time window of variable size (Fig. 4.22B). For a time window of size  $T_w$  and a neuron  $i$  that bursts at  $t_i$ , the synchronously spiking neurons have their burst onset times within a time interval  $(t_i - T_w/2, t_i + T_w/2)$ . The similarity of inputs to neuron  $i$  and a synchronously spiking neuron is computed as the fraction of the presynaptic neurons common to the two neurons among all presynaptic neurons to the two neurons (the Jaccard index). The mean Jaccard index of all synchronously spiking neurons at  $t_i$  represents the similarity of inputs at this time. The mean Jaccard index for all burst times is defined as the similarity of inputs for a given time window  $T_w$ .

Networks with prominent oscillations in burst density (vel. 2 and 10 times) show a stair-like decay in the similarity of inputs, which is expected for synfire chain topology with defined groups and all-to-all connections from neurons in one group to the next; whereas networks with weak activity oscillations (vel. 0.5, 1 and 1.33 times) have a smooth decreasing curve, which is expected for polychronous chain networks with no definable groups. All grown networks, regardless synfire chains or polychronous chains, possess a property of nearly synchronous excitatory inputs to the postsynaptic neurons (Fig. 4.22C).

To understand how conduction velocity influences the network topology, we examine the case of slow conduction velocity, for which the potential connections between neurons have a wide range of axonal delays. We monitor the burst onset latency of the recruited neurons relative to their presynaptic neurons (parents) (Fig. 4.23A). In the beginning of

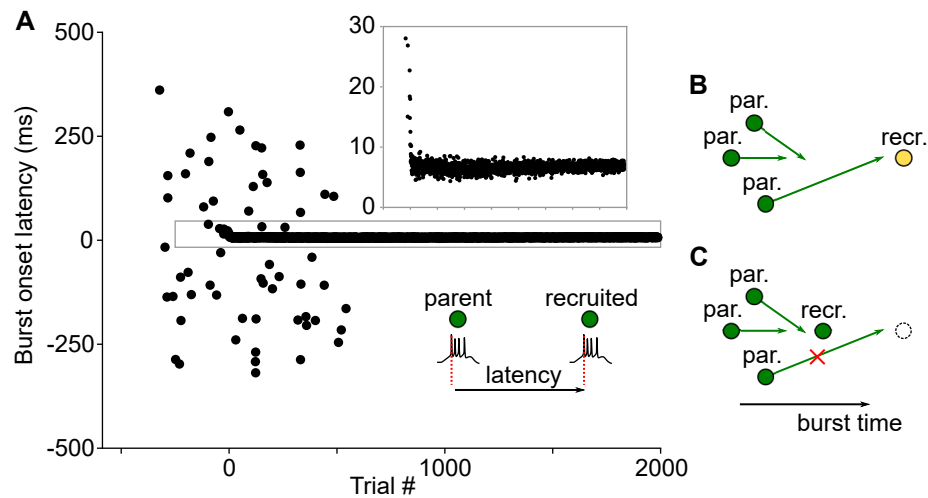


**Figure 4.23.** Decrease in burst onset latency of recruited neurons leads to pruning of long delay connections. (A) Burst onset latency between parent and recruited neurons decreases during recruitment. (B-C) Mechanism for pruning long delay connections. (B) A neuron being recruited initially spikes at a large latency, which allows long delay connections to emerge. (C) After recruitment, the neuron spikes at a shorter latency, which makes long delay connections to arrive late and be pruned via LTD.

recruitment, connections to the recruited neurons are still weak and these neurons have a large range of burst onset latency. This permitted connections with a large range of delays to target the recruited neurons via LTP (Fig. 4.23B). Subsequently, however, the burst onset latency is gradually decreasing due to strengthening of the connections from the parent neurons (Fig. 4.23A, inset). This results in pruning of some of the inputs with long axonal delays via LTD (Fig. 4.23C). Therefore, the grown network has a prominent bias towards forming short delay connections while keeping a few long delay connections, characteristic of the delay distribution for the polychronous chain topology. In contrast, when the conduction velocity is high, all possible connections have short delays, and there is no bias towards short distance connections. In this case, synfire chain topology emerges.

#### 4.2.9 The role of inhibition in network growth

Inhibition should play an important role in network growth since it impacts the spontaneous activity of immature neurons. Due to the randomness of the connections between HVC-RA neurons and HVC-I neurons, feedback inhibition to individual HVC-RA neurons is inhomogeneous in time. To see if this affects which neurons get recruited into the network, we track the inhibitory conductance of all HVC-RA neurons in the network.

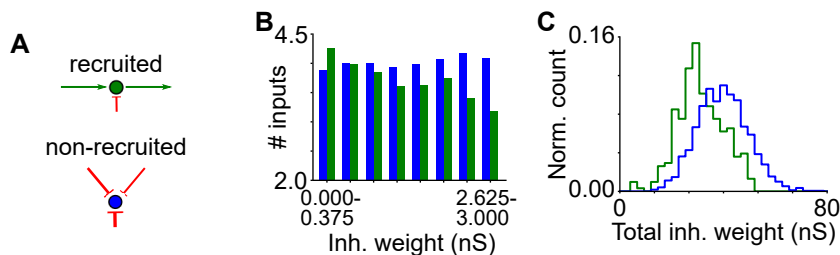


**Figure 4.24.** The role of inhibition in network growth. (A-C) Comparison of inhibitory weights onto recruited and non-recruited neurons. (A) Recruited neurons (green circles) receive strong excitation and weak inhibition. Non-recruited neurons (blue circles) receive strong inhibition. (B) Histogram of inhibitory weights shows stronger connections onto non-recruited (blue bars), compared to recruited (green bars) neurons. (C) Distribution of total inhibitory weights for non-recruited neurons (blue) is shifted towards stronger inhibition, compared to recruited neurons (green).

We consider a simulation with conduction velocity  $100 \mu\text{m}/\text{ms}$  (the value observed in HVC [87]) and switch off the replacement of silent non-recruited neurons to allow a direct comparison between recruited and non-recruited neurons. A neuron is designated as recruited if it spiked consistently during the testing trials of the grown network in more than 95 out of 100 trials. The time of its recruitment is estimated using its spike history during the growth. At each trial, the number of the neuron’s spikes averaged over a window of the past 25 trials is computed, and when the average first reaches 1, which signals the start of reliable spiking, the trial is defined as the trial at which the neuron is recruited.

The inhibition is tracked for 30,000 trials, by the end of which, the number of supersynaptic and active connections have reached stable values and the network growth stopped. We observe that in the grown network, individual inhibitory connections to non-recruited neurons are stronger compared to inhibition to recruited neurons (Fig. 4.24A-B). Total inhibitory input, computed as a sum of all inhibitory input conductance, is also significantly larger for non-recruited neurons ( $P < 10^{-42}$ , one-sided t-test, see Fig. 4.24C).

We then compare temporal dynamics of inhibitory conductance of recruited and non-recruited HVC-RA neurons during recruitment (Fig. 4.25A-D). We first wonder if there is any difference in inhibition received by recruited and non-recruited neurons in LTP window, i.e., time interval which is critical for the selection of postsynaptic targets. For a recruited neuron  $i$ , an LTP window is defined relative to the burst time of its presynaptic neuron  $j$ , during which the synaptic strength from neuron  $j$  to neuron  $i$  can be strengthened according to the BTDP synaptic plasticity rule. Specifically, the window is the time interval  $(t_j + d_{ji} + T_0, t_j + d_{ji} + T_0 + \tau_P)$ , where  $d_{ji}$  is the axonal

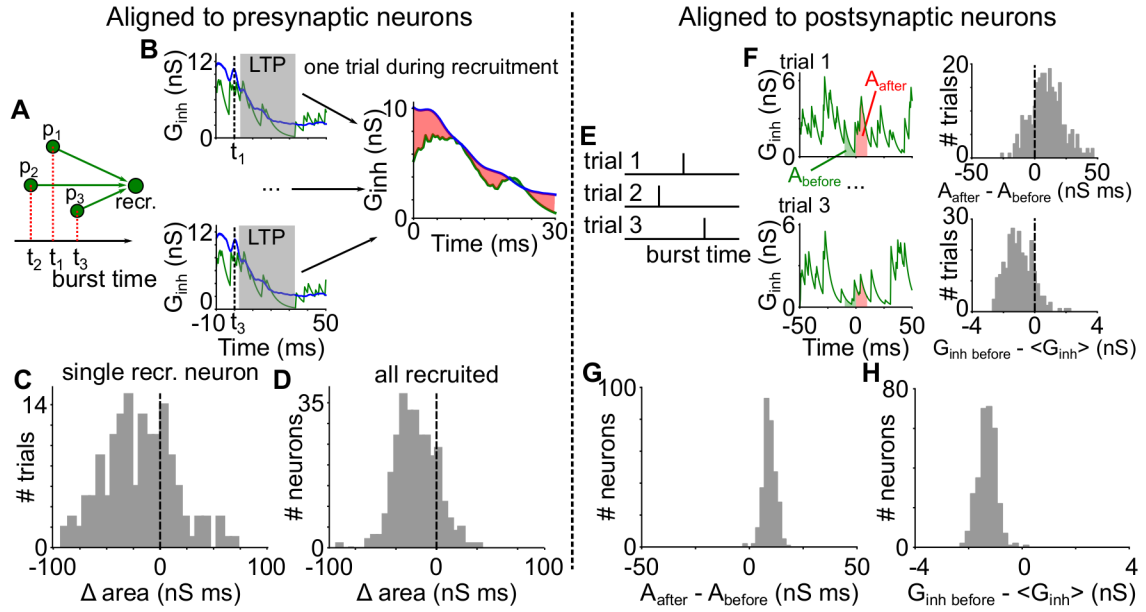


**Figure 4.25.** The role of inhibition in network growth (Continued). (A-D) Comparison of inhibitory conductance aligned to presynaptic neurons during recruitment. (A) Inhibitory conductance is aligned to the burst onset times of presynaptic parent neurons. (B) Inhibitory conductance in the LTP window is averaged across all parent neurons at each trial during recruitment and compared between recruited and non-recruited neurons using the area under the conductance curve. (C) Difference in the area under the conductance curve for a single recruited neuron. (D) Difference in the area under the conductance curve for all recruited neurons. (E-H) Comparison of inhibitory conductance aligned to postsynaptic neurons during recruitment. (E) Burst times of a neuron being recruited at different simulation trials. (F) Inhibitory conductance is aligned to the burst onset times of recruited neurons. Difference in inhibitory conductance after and before burst is calculated using area under the conductance curve. Inhibitory conductance before burst is also compared to the mean inhibitory conductance during the trial. (G) Difference in inhibitory conductance after and before burst for all recruited neurons. (H) Difference in inhibitory conductance before burst and mean inhibitory conductance for all recruited neurons.

delay;  $T_0 = 2$  ms is the time shift in BTDP synaptic plasticity rule; and  $\tau_P = 30$  ms is the time scale of the LTP part of BTDP. At each trial before the recruitment, a set of inhibitory conductance traces on neuron  $i$  is extracted in the LTP windows relative to all its presynaptic neurons (Fig. 4.25B). The average of this set represents an inhibitory conductance of the recruited neuron at trial  $T$  aligned to its presynaptic neurons. For comparison, an average inhibitory conductance of non-recruited neurons is extracted in the same time intervals, and is defined as the inhibitory conductance of non-recruited neurons. Difference in the area under conductance curves is computed numerically using a trapezoid method (Fig. 4.25B(right) and Fig. 4.25C). The median difference in the area computed for all trials before the recruitment represents the difference in the inhibitory

conductance between the recruited neuron and the non-recruited neurons Fig. 4.25D). Recruited neurons show significantly smaller inhibitory conductance ( $P < 10^{-46}$ , one-sided paired t-test) in LTP window. This observation shows that neurons that receive less inhibition from the parent neurons are preferentially recruited into the growing edge of the network.

We next wonder if there is any temporal inhibitory structure in traces aligned postsynaptically. For analysis of inhibition on a recruited neuron  $i$  relative to its burst onset times before the recruitment, only trials in which neuron  $i$  produced bursts are considered (Fig. 4.25E). For each such trial, the area under the inhibitory conductance curve is calculated for 10 ms before and 10 ms after the burst onset time (Fig. 4.25F). The median difference in area for all trials represents the difference in the inhibitory conductance before and after bursting of neuron  $i$ . Recruited neurons during the recruitment show an increase in inhibitory conductance right after the burst onset time ( $P < 10^{-176}$ , one-sided paired t-test, Fig. 4.25G). We attribute this observation to the self-inhibition of the neurons due to the prevalence of local connections between HVC-RA neurons and HVC-I neurons. By bursting, HVC-RA neuron activate a subset of nearby interneurons, which in turn provides a feedback inhibition.

We also compute the difference of the inhibitory conductance before burst relative to the average, defined as median of the differences between the mean inhibitory conductance 10 ms before the burst and the mean during the trial for all trials before the recruitment. We find that the inhibitory conductance on the recruited neurons right before the burst onset time is smaller than the mean computed over the simulation trials (Fig. 4.25H,  $P < 10^{-170}$ , one-sided paired t-test). This further supports that HVC-RA neurons require less inhibition on average to be recruited. Since initial excitatory inputs to HVC-RA neurons are weak, the recruitment favors HVC-RA neurons which receive less inhibition to ensure they can be activated by the parent neurons at the growing edge.

To investigate the inhibition after recruitment, similar procedure is applied to 100 test trials of the grown network. Alignment to presynaptic parent neurons (Fig. 4.26A) also shows significantly smaller inhibitory conductance for recruited neurons in LTP window ( $P < 10^{-30}$ , one-sided paired t-test). Postsynaptic alignment, however, does not show the effect of self-inhibition in the grown network. We attribute it to the high network driven activity of HVC-I neuron population (Fig. 4.26B). Finally, the inhibitory conductance before the burst is larger than the mean conductance for the trial ( $P < 10^{-113}$ , one-sided paired t-test). That again reflects the high network activity of HVC-I neurons and also demonstrates that activation of mature HVC-RA neurons relies on strong excitatory

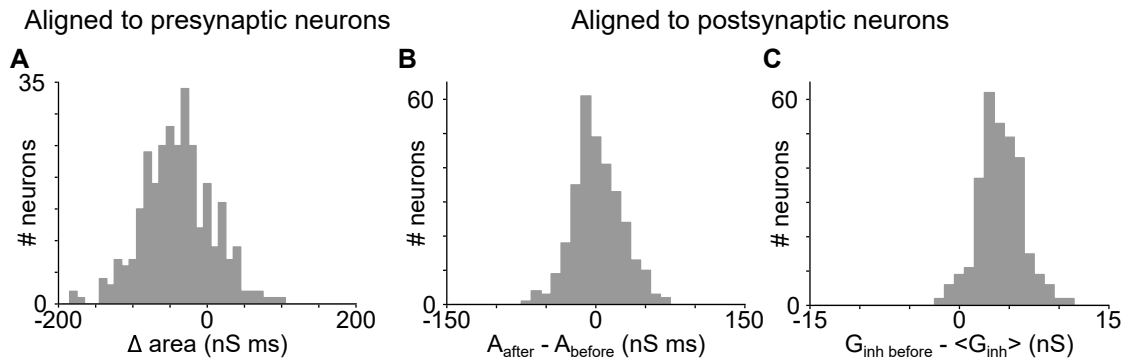


**Figure 4.26.** Comparison of inhibitory conductance for a grown network based on 100 test trials. (A) Difference in the area under the conductance curve in the LTP window for all recruited neurons aligned to presynaptic parents. (B-C) Analysis of inhibitory conductance of recruited neurons aligned postsynaptically. (B) Difference in inhibitory conductance after and before burst for all recruited neurons. (C) Difference in inhibitory conductance before burst and mean inhibitory conductance for all recruited neurons.

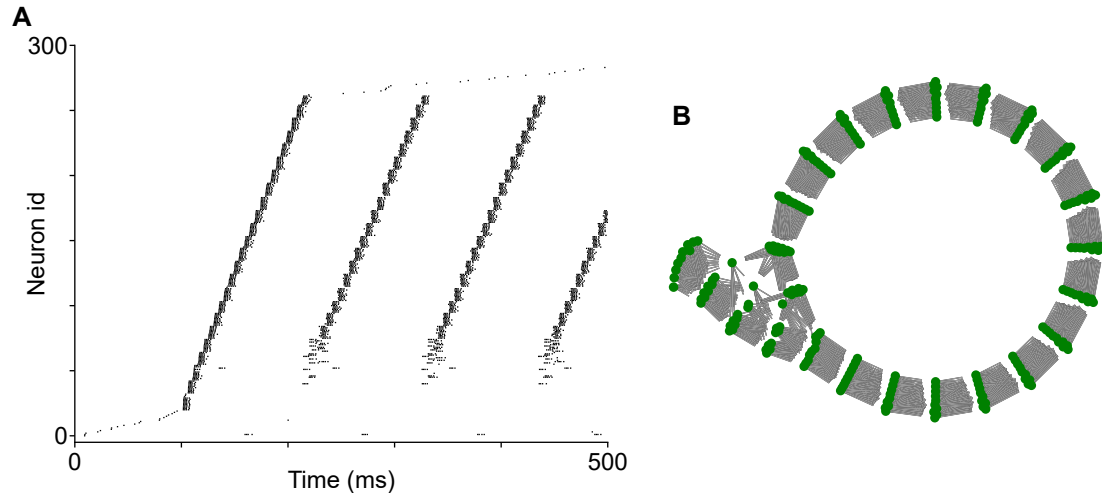


**Figure 4.27.** Loop formation in the network with noisy mature HVC-RA neurons. When we use a single population of mature spontaneously active HVC-RA neurons receiving a large white noise stimulus of amplitude 0.25 nA to soma and 0.5 nA to dendrite, loop sequences form. Here we use a fast conduction velocity 1000  $\mu\text{m}/\text{ms}$ , which leads to the emergence of a synfire chain. (A) Raster plot of network dynamics. (B) Network topology based on synaptic weights between neurons.

inputs, rather than on weak inhibition (Fig. 4.26C).

#### 4.2.10 Role of immature neurons

Inclusion of immature neurons has an important effect on the growth process of synaptic chain networks. In the model, spontaneous activity plays a critical role. The distinction

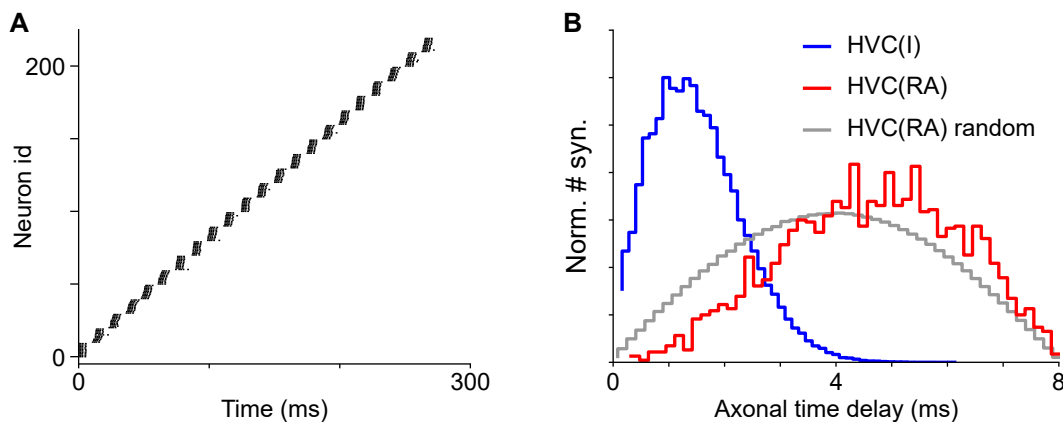


**Figure 4.28.** Prevalence of long delays in network with weak synaptic connections. When we use a small value  $G_{max} = 1.5$  nS for the maximal strength of connections between HVC-RA and a conduction velocity  $100 \mu\text{m}/\text{ms}$ , a synfire chain forms with many short delays pruned. This is expected, since weak synaptic input results in HVC-RA neurons having long integration times. Thus, inputs corresponding to connections with long delays (i.e., long delay inputs) do not arrive late and are strengthened via LTP part of BTDP, while short delay inputs arrive too early, are not strengthened as much, and lose competition to long delay inputs. (A) Raster plot of network dynamics. (B) Axonal time delay distributions for efferent HVC-RA connections.

between immature and mature neurons allows different levels of spontaneous activity in these two populations. Immature neurons are more spontaneously active due to higher intrinsic excitability, and they are the targets of recruitments by the neurons at the growth edge. In contrast, mature neurons in the network are not spontaneously active, hence are not targets of recruitments. This allows continued growth of the network, as long as there is a supply of immature neurons in the pool. This was not the case in the previous models, in which there was a single neuron population [100, 101, 107]. There, all neurons had similar level of spontaneous activity and consequently, the chain growth usually stopped by formation of loops after neurons already into the chain were recruited. We confirm that loops emerge in our model as well when using a single population of mature and spontaneously active HVC-RA neurons (see Fig. 4.27).

#### 4.2.11 Resilience to changes in model parameters

Our growth algorithm is robust with respect to the changes in the model parameter values. The use of different strength of inhibitory connections (varied between  $G_{ie} = 0.015$  mS/cm<sup>2</sup> and  $G_{ie} = 0.060$  mS/cm<sup>2</sup>), different number of efferent supersynaptic connections ( $N_s = 10$  and  $N_s = 20$ ), and different maximal strength of excitatory connections between HVC-RA neurons (between  $G_{max} = 1.5$  nS and  $G_{max} = 4$  nS)

leads to the emergence of precisely timed neural sequences. In certain cases, qualitative differences in the distribution of axonal conduction delays of the grown connections between HVC-RA neurons and changes in the network topology are observed. For instance, when small excitatory synaptic weight  $G_{max} = 1.5 nS$  is used with conduction velocity  $100 \mu\text{m}/\text{ms}$  (producing realistic axonal delays), a synfire chain, rather than a polychronous network, emerges (see Fig. 4.28A). The axonal delay distribution for formed connections between HVC-RA neurons shows bias toward long delay connections (see Fig. 4.28B), with many short delays pruned. This is expected, since weak synaptic input results in HVC-RA neurons having long integration times. Thus, inputs corresponding to connections with long delays (i.e., long delay inputs) do not arrive late and are strengthened via LTP part of BTDP, while short delay inputs arrive too early, are not strengthened as much, and lose competition to long delay inputs.

#### 4.2.12 Spatio-temporal activity pattern

According to the recent study [87], there is no structure in the spatio-temporal pattern of activity in HVC. In other words, it is random. Since the network growth in our model does not rely on any assumptions regarding the spatio-temporal activity pattern (except for the random choice of training neurons), its randomness is not guaranteed. To test the activity pattern in the model, we analyze results of the network with conduction velocity  $100 \mu\text{m}/\text{ms}$ . Snapshots of locations of the active neurons on the sphere, taken at different times of the network dynamics, reveal no apparent structure (see Fig. 4.29A). Latitude and longitude of the active neurons look random (see Fig. 4.29B,C). Finally, we test if distance between active neurons on the sphere is related to the difference in their burst times. In the case of spatially clustered activity propagating on the surface of the sphere, there will be a strong correlation between space and time because nearby neurons will have similar burst times. The grown network does not show any significant correlation between space and time (see Fig. 4.29D), suggesting that activity is not spatially clustered. Together these observations provide strong evidence that spatio-temporal activity pattern in the model is random, which is consistent with experimental data.

#### 4.2.13 Sequence splitting

In addition to sequence growth, extracellular recordings in juvenile zebra finches also revealed sequence splitting during the syllable development [102]. At the protosyllable stage, majority of the projection neurons fired in a single protosequence. When several

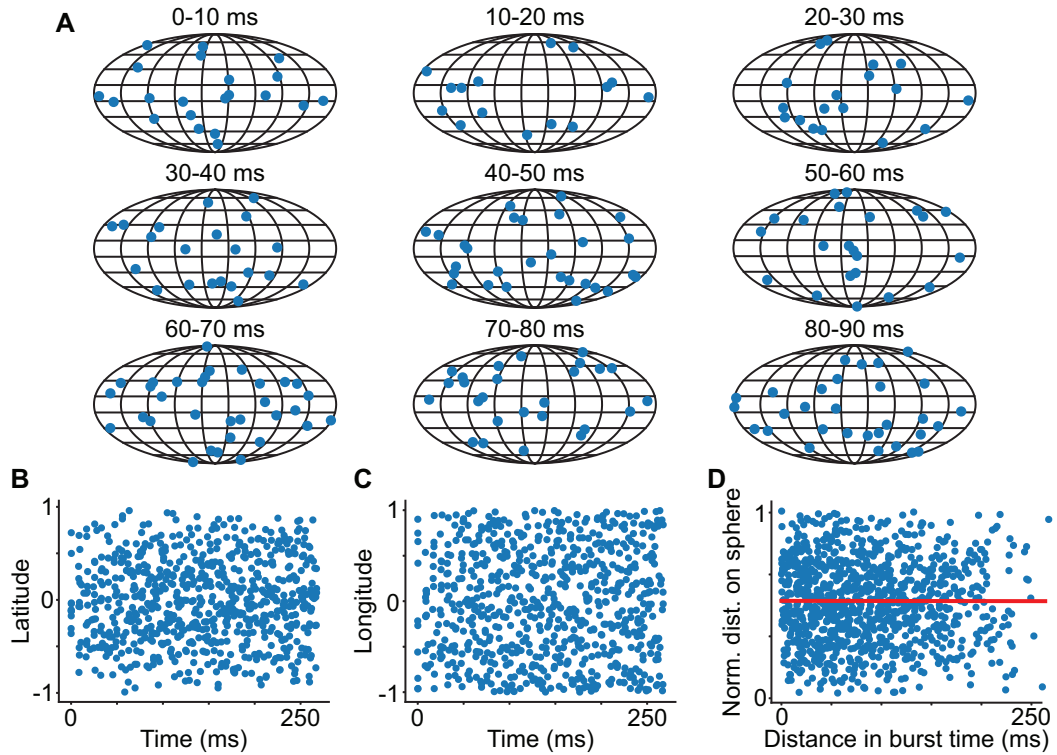


**Figure 4.29.** Spatio-temporal activity pattern of HVC-RA neurons in the polychronous network with conduction velocity  $100 \mu\text{m}/\text{ms}$  shows no structure. (A) Snapshots showing location of active neurons on 2d Mollweide projection of the sphere at different times of neural dynamics. Latitude (B) and longitude (C) of active neurons versus their burst time. (D) Spatial distance between active neurons on the sphere is uncorrelated with the temporal distance between their burst times (1,000 random neuronal pairs shown).

syllable types emerged from a common protosyllable, the corresponding protosequence split. While there were still neurons firing at all syllables with the same latencies relative to syllable onsets (“shared neurons”), more neurons fired specifically to a single syllable type. Gradually, the shared neurons disappeared. The authors proposed a model, according to which a protosequence grown from a common seed of synchronously activated neurons is split by dividing the seed into several groups activated at different times, and also by increasing local inhibition. In our study, the splitting does not happen during the network growth. We hypothesized that a combination of large set of training neurons and widely distributed axonal delays may lead to the sequence splitting. However, our simulation with 100 training neurons (10 times the original number) and conduction velocity  $100 \mu\text{m}/\text{ms}$  still leads to the emergence of a single sequence (see Fig. 4.30). Activation of seed neurons at different times and increase in inhibition may induce protosequence splitting in our model, but we haven’t explored these possibilities.

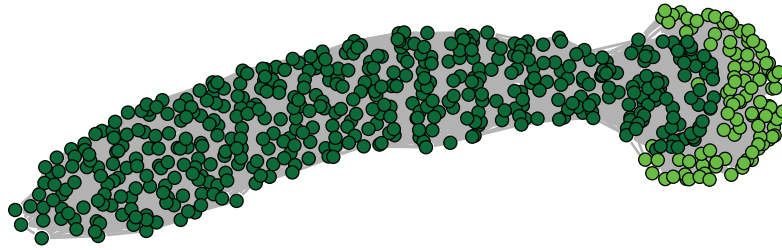


**Figure 4.30.** Network growth with large training set of 100 neurons and conduction velocity  $100 \mu\text{m}/\text{ms}$  does not result in sequence splitting. Network topology based on supersynaptic weights shows that all training neurons (shown as light green circles) converge on similar targets (dark green circles) and a single polychronous sequence emerges.

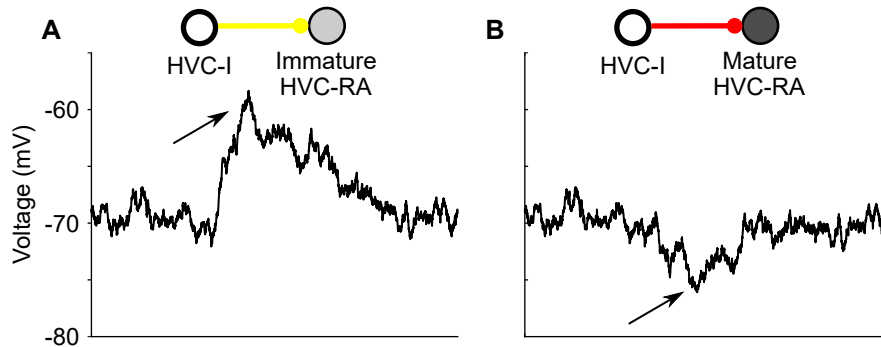


**Figure 4.31.** GABA response of immature (A) and mature (B) HVC-RA neurons. Immature HVC-RA is depolarized by inhibitory input, while mature HVC-RA shows hyperpolarizing response.

#### 4.2.14 Depolarizing GABA during development

Immature neurons in many neural circuits across multiple species go through a period of depolarizing inhibition before switching to hyperpolarizing inhibition, which is caused by an elevated GABA reversal potential on immature neurons. Thus, we wonder whether maturation of the GABA reversal potential affects the sequence growth mechanism.

To address this question, we modify the HVC-RA neuron model and the maturation model. We simplify both of them by getting rid of the developmental change in burst tightness and excitability. Specifically, we set low-threshold potassium conductance to zero and use adult values for calcium conductance in dendrite and rest potential. In other words, we use HVC-RA neuron model described in Chapter 2. To account for the developmental changes in inhibition, we set GABA reversal potential of immature neurons to  $-56 \text{ mV}$ . Therefore, membrane potential of immature neurons is depolarized upon receiving inhibitory input (see Fig. 4.31A). Mature neurons have GABA reversal potential of  $-80 \text{ mV}$  and inhibitory input elicits a hyperpolarizing response (see Fig. 4.31B). GABA

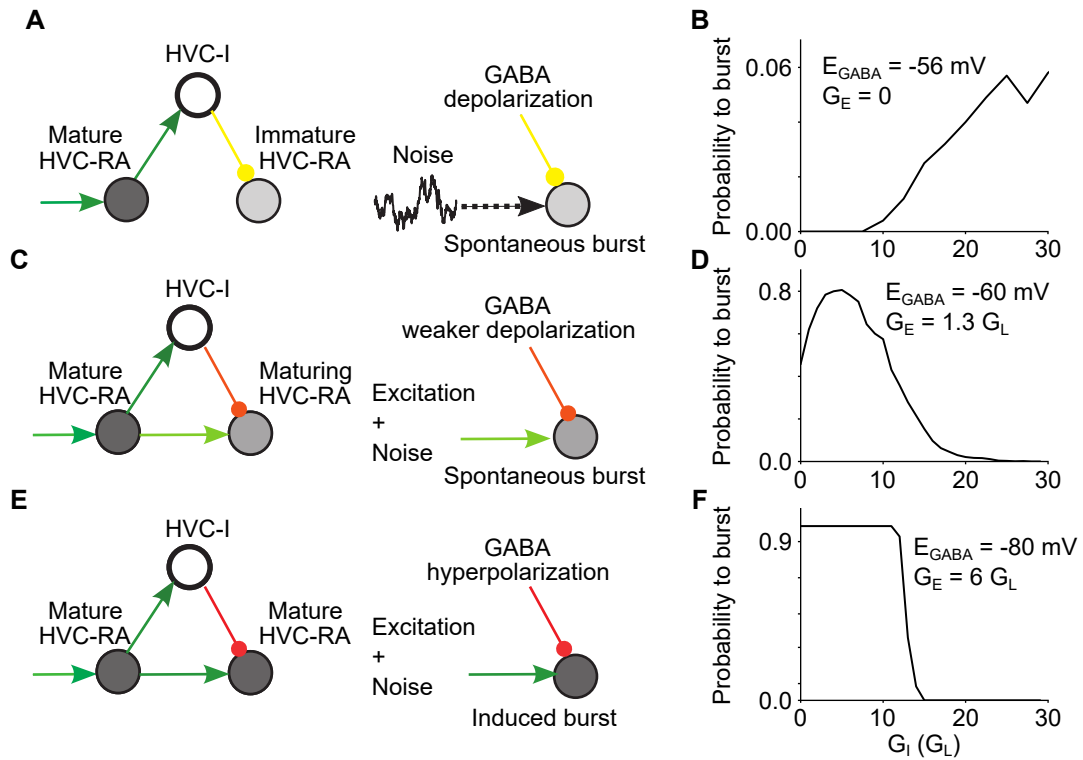


**Figure 4.32.** Recruitment is guided by inhibition. (A,C,E) Left: Development of HVC-RA  $\rightarrow$  HVC-I  $\rightarrow$  HVC-RA network motif that leads to recruitment of pool neurons into the network. Right: Inputs received by recruited HVC-RA at different stages of maturation. (B,D,F) Probability to produce a burst for an HVC-RA neuron receiving synchronous inhibitory and excitatory input at different maturation stages. (A) Immature HVC-RA neuron bursts spontaneously due to depolarizing GABA potential and noise. (B) Spontaneous activity increases with inhibition strength. (C) Excitatory connections develop from mature HVC-RA to spontaneously active pool neurons. These pool neurons are gradually maturing and receive weaker GABA depolarization. (D) Moderate inhibition increases probability to burst, while large inhibition produces a shunting effect. (E) Recruited neurons mature and receive strong excitatory input and hyperpolarizing inhibition. (F) Probability to burst decreases sharply with increase in inhibitory input.

potential is changing in age and activity dependent manner with the same time scales of 50,000 s and 500 s as in the original maturation model. We also increase the noise in both mature and immature HVC-RA neurons by setting white noise amplitude in soma to 0.15 nA and in dendrite to 0.35 nA. Additionally, we decrease the LTP constant in BTDP rule to 0.2 nS.

With depolarizing GABA effect on immature neurons, the network growth is guided by inhibition (see Fig. 4.32). Active mature HVC-RA neurons drive activity of interneurons, that in turn provide depolarizing inhibition to immature pool neurons (see Fig. 4.32A(Left)). This inhibition alone is not enough to make immature neurons spike.

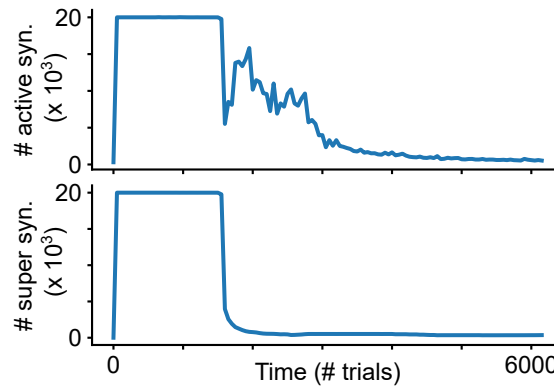


**Figure 4.33.** Large inhibition  $G_{ie} = 0.24 \text{ mS/cm}^2$  destroys the sequence. Numerous active (top) and super (bottom) connections, that emerge shortly after the start of the simulation, are pruned once the recruited neurons mature. This is caused by too strong hyperpolarizing inhibitory input to recruited neurons, which makes them silent.

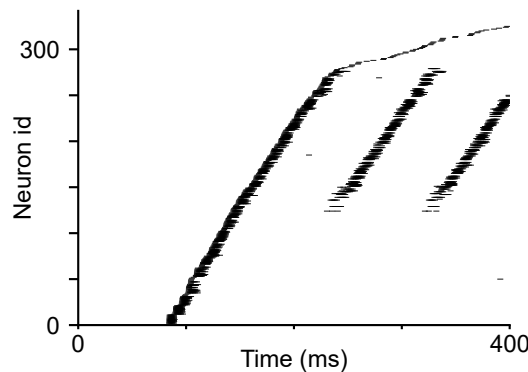


**Figure 4.34.** Moderate inhibition  $G_{ie} = 0.06 \text{ mS/cm}^2$  results in emergence of a loop. This happens due to immature neurons spiking spontaneously throughout the entire sequence, which leads to the emergence of recurrent connections. The mechanism is similar to the case of a single population of noisy mature neurons described previously (Fig. 4.27)

However, the combination of noise and depolarizing inhibition leads to spontaneous activity in immature neurons, and probability to spike increases with the strength of inhibitory input (see Fig. 4.32A(Right) and Fig. 4.32B). According to BTDP rules, connections emerge from mature HVC-RA neurons to spontaneously active pool neurons (see Fig. 4.32C(Left)). Due to maturation, these pool neurons have lower GABA reversal potential and their spontaneous activity depends on both inhibitory and excitatory inputs (Fig. 4.32C(Right) and Fig. 4.32D). Eventually, excitatory connections become strong and GABA exerts a hyperpolarizing effect on the recruited neurons (Fig. 4.32E). In mature state, the spiking of HVC-RA neurons relies completely on the excitatory input (Fig. 4.32F).

The sequence growth in this model depends on the strength of inhibition. We

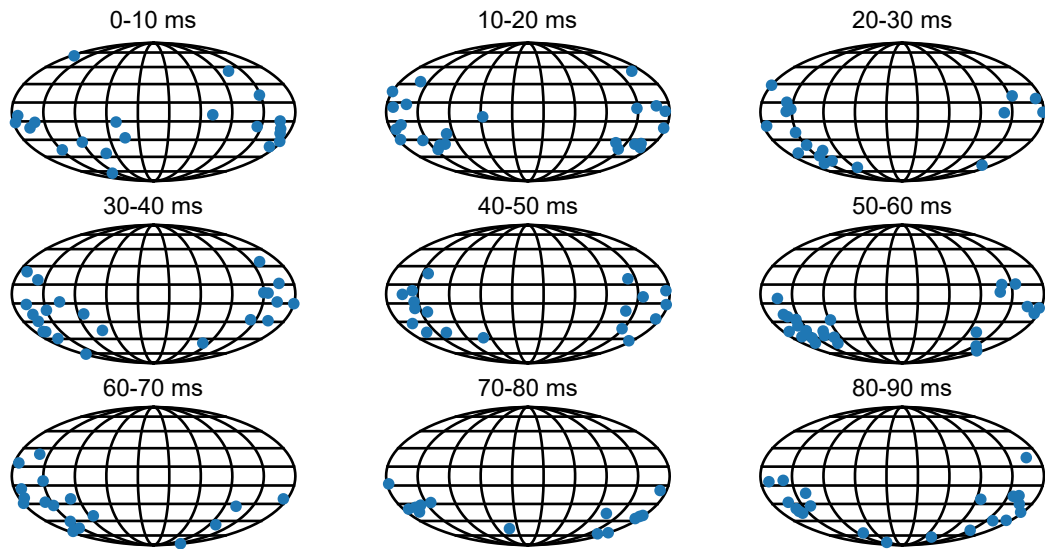


**Figure 4.35.** Spatio-temporal activity of HVC-RA neurons with depolarizing GABA reveals clustered activity patterns. Shown are snapshots with locations of active neurons on 2d Mollweide projection of the sphere at different times of neural dynamics.

systematically vary the strength of inhibitory connections to grow sequences in the network with fast axonal conduction velocity  $1000 \mu\text{m}/\text{ms}$ . Inhibition  $G_{ie} = 0.03 \text{ mS}/\text{cm}^2$  and smaller is not large enough to drive spontaneous activity of pool neurons and therefore no sequence emerges. Inhibition  $G_{ie} = 0.24 \text{ mS}/\text{cm}^2$  and larger is effective in recruiting initial cohort of HVC-RA neurons. However, upon maturing the recruited neurons receive too strong inhibition and are unable to spike. Therefore, large inhibition prevents sequence formation, since recruited neurons become silent and are replaced by new immature neurons (see Fig. 4.33).

Sequence growth with moderate inhibition also has significant issues. During the growth, HVC-RA neurons in the sequence drive activity of interneurons. Therefore, immature pool HVC-RA neurons are likely to spike throughout the entire sequence, not just at the end of it. It leads to the formation of a loop, similarly to the case of a single population of noisy mature neurons described previously (see Fig. 4.34 and Fig. 4.27). Therefore, in this model it is problematic to grow long sequences. Another problem is the short spatial range of formed connections between HVC-RA neurons. Since large inhibition increases probability of immature neurons to burst, it facilitates the emergence of clustered spatio-temporal activity pattern (see Fig. 4.35). This is inconsistent with experimental observations that spatio-temporal activity pattern in HVC is unstructured and random.

Therefore, we conclude that while the model with developmental change in inhibition

does result in sequence formation, it is less robust to the changes in model parameters and produces results incompatible with HVC. It may, however, be suitable as a model for development of other neural circuits, for instance, hippocampus.

#### **4.2.15 Conclusions**

In this section, we developed a detailed computational model for sequence formation in HVC. The model includes more biologically realistic features that lacked in previous models, including explicit modeling of HVC-I neurons, spatial distributions of HVC neurons, and realistic axonal delays in HVC [87]. We showed that immature neurons, which are more excitable hence have higher spontaneous activity rates compared to mature neurons, are preferentially recruited at the growth edge. The inclusion of the axonal delays leads to a long polychronous chain network, a structure favored by a recent analysis of HVC network and dynamics [87]. In contrast, neglecting axonal delays leads to synfire chains [67, 68], previously thought to be the topology of the HVC network [100, 101, 107]. Explicit modeling of HVC-I also predicts that the wiring process favors a path of less inhibition, such that neurons that are recruited receive less forward inhibition from the recruiting neurons, highlighting the importance of inhibition in HVC [90]. Our model also reproduces the observation that HVC-RA neurons connect to more distal HVC-RA neurons, unlike their tendency to connect to nearby HVC-I neurons [50].

# Bibliography

- [1] LASHLEY, K. S. (1951) *The problem of serial order in behavior*, vol. 21, Bobbs-Merrill.
- [2] CAPALDI, E. J., D. R. VERRY, and T. DAVIDSON (1980) “Memory, serial anticipation pattern learning, and transfer in rats,” *Animal Learning & Behavior*, **8**(4), pp. 575–585.
- [3] HULSE, S. H. (1980) “The case of the missing rule: Memory for reward vs. formal structure in serial-pattern learning by rats,” *Learning & Behavior*, **8**(4), pp. 689–690.
- [4] PAYNE, R. S. and S. MCVAY (1971) “Songs of humpback whales,” *Science*, **173**(3997), pp. 585–597.
- [5] WINN, H. E., P. J. PERKINS, and T. C. POULTER (1971) *Sounds of the humpback whale*, Narragansett Marine Laboratory.
- [6] HOLY, T. E. and Z. GUO (2005) “Ultrasonic songs of male mice,” *PLoS biology*, **3**(12), p. e386.
- [7] DAVIDSON, S. M. and G. S. WILKINSON (2004) “Function of male song in the greater white-lined bat, *Saccopteryx bilineata*,” *Animal Behaviour*, **67**(5), pp. 883–891.
- [8] CATCHPOLE, C. K. and P. J. SLATER (2003) *Bird song: biological themes and variations*, Cambridge university press.
- [9] BERWICK, R. C., K. OKANOYA, G. J. BECKERS, and J. J. BOLHUIS (2011) “Songs to syntax: the linguistics of birdsong,” *Trends in cognitive sciences*, **15**(3), pp. 113–121.
- [10] WILD, J. M. (1997) “Neural pathways for the control of birdsong production,” *Journal of neurobiology*, **33**(5), pp. 653–670.
- [11] FEE, M. S. and C. SCHARFF (2010) “The songbird as a model for the generation and learning of complex sequential behaviors,” *ILAR journal*, **51**(4), pp. 362–377.

- [12] VICARIO, D. S. and F. NOTTEBOHM (1988) “Organization of the zebra finch song control system: I. Representation of syringeal muscles in the hypoglossal nucleus,” *Journal of Comparative Neurology*, **271**(3), pp. 346–354.
- [13] WILD, J. M. and J. ARENDS (1987) “A respiratory-vocal pathway in the brainstem of the pigeon,” *Brain research*, **407**(1), pp. 191–194.
- [14] KARTEN, H. J. (1991) “Homology and evolutionary origins of the ‘neocortex’,” *Brain, behavior and evolution*, **38**(4-5), pp. 264–272.
- [15] NOTTEBOHM, F., J. A. PATON, and D. B. KELLEY (1982) “Connections of vocal control nuclei in the canary telencephalon,” *Journal of Comparative Neurology*, **207**(4), pp. 344–357.
- [16] NOTTEBOHM, F., T. M. STOKES, and C. M. LEONARD (1976) “Central control of song in the canary, *Serinus canarius*,” *Journal of Comparative Neurology*, **165**(4), pp. 457–486.
- [17] REINER, A., D. J. PERKEL, L. L. BRUCE, A. B. BUTLER, A. CSILLAG, W. KUENZEL, L. MEDINA, G. PAXINOS, T. SHIMIZU, G. STRIEDTER, ET AL. (2004) “Revised nomenclature for avian telencephalon and some related brainstem nuclei,” *Journal of Comparative Neurology*, **473**(3), pp. 377–414.
- [18] BOTTJER, S. W., E. A. MIESNER, and A. P. ARNOLD (1984) “Forebrain lesions disrupt development but not maintenance of song in passerine birds,” *Science*, **224**(4651), pp. 901–903.
- [19] SOHRABJI, F., E. J. NORDEEN, and K. W. NORDEEN (1990) “Selective impairment of song learning following lesions of a forebrain nucleus in the juvenile zebra finch,” *Behavioral and neural biology*, **53**(1), pp. 51–63.
- [20] SCHARFF, C. and F. NOTTEBOHM (1991) “A comparative study of the behavioral deficits following lesions of various parts of the zebra finch song system: implications for vocal learning,” *Journal of Neuroscience*, **11**(9), pp. 2896–2913.
- [21] ZANN, R. A. (1996) *The zebra finch: a synthesis of field and laboratory studies*, vol. 5, Oxford University Press.
- [22] DOUPE, A. J. and P. K. KUHL (1999) “Birdsong and human speech: common themes and mechanisms,” *Annual review of neuroscience*, **22**(1), pp. 567–631.
- [23] ARONOV, D., L. VEIT, J. H. GOLDBERG, and M. S. FEE (2011) “Two distinct modes of forebrain circuit dynamics underlie temporal patterning in the vocalizations of young songbirds,” *Journal of Neuroscience*, **31**(45), pp. 16353–16368.
- [24] VEIT, L., D. ARONOV, and M. S. FEE (2011) “Learning to breathe and sing: development of respiratory-vocal coordination in young songbirds,” *Journal of Neurophysiology*, **106**(4), pp. 1747–1765.

- [25] LIU, W.-C., T. J. GARDNER, and F. NOTTEBOHM (2004) “Juvenile zebra finches can use multiple strategies to learn the same song,” *Proceedings of the National Academy of Sciences*, **101**(52), pp. 18177–18182.
- [26] TCHERNICHOVSKI, O., P. P. MITRA, T. LINTS, and F. NOTTEBOHM (2001) “Dynamics of the vocal imitation process: how a zebra finch learns its song,” *Science*, **291**(5513), pp. 2564–2569.
- [27] TCHERNICHOVSKI, O. and P. MITRA (2002) “Towards quantification of vocal imitation in the zebra finch,” *Journal of Comparative Physiology A*, **188**(11-12), pp. 867–878.
- [28] ARNOLD, A. P. (1975) “The effects of castration on song development in zebra finches (*Poephila guttata*),” *Journal of Experimental Zoology*, **191**(2), pp. 261–277.
- [29] FEHÉR, O., H. WANG, S. SAAR, P. P. MITRA, and O. TCHERNICHOVSKI (2009) “De novo establishment of wild-type song culture in the zebra finch,” *Nature*, **459**(7246), p. 564.
- [30] ARONOV, D., A. S. ANDALMAN, and M. S. FEE (2008) “A specialized forebrain circuit for vocal babbling in the juvenile songbird,” *Science*, **320**(5876), pp. 630–634.
- [31] NORDEEN, K. W. and E. J. NORDEEN (1988) “Projection neurons within a vocal motor pathway are born during song learning in zebra finches,” *Nature*, **334**(6178), p. 149.
- [32] ALVAREZ-BUYLLA, A., M. THEELEN, and F. NOTTEBOHM (1988) “Birth of projection neurons in the higher vocal center of the canary forebrain before, during, and after song learning,” *Proceedings of the National Academy of Sciences*, **85**(22), pp. 8722–8726.
- [33] SCOTT, B. B. and C. LOIS (2007) “Developmental origin and identity of song system neurons born during vocal learning in songbirds,” *Journal of Comparative Neurology*, **502**(2), pp. 202–214.
- [34] KIRN, J. R. (2010) “The relationship of neurogenesis and growth of brain regions to song learning,” *Brain and language*, **115**(1), pp. 29–44.
- [35] BOTTJER, S. W., E. A. MIESNER, and A. P. ARNOLD (1986) “Changes in neuronal number, density and size account for increases in volume of song-control nuclei during song development in zebra finches,” *Neuroscience letters*, **67**(3), pp. 263–268.
- [36] WILBRECHT, L., A. CRIONAS, and F. NOTTEBOHM (2002) “Experience affects recruitment of new neurons but not adult neuron number,” *Journal of Neuroscience*, **22**(3), pp. 825–831.

- [37] WALTON, C., E. PARISER, and F. NOTTEBOHM (2012) “The zebra finch paradox: song is little changed, but number of neurons doubles,” *Journal of Neuroscience*, **32**(3), pp. 761–774.
- [38] BURD, G. D. and F. NOTTEBOHM (1985) “Ultrastructural characterization of synaptic terminals formed on newly generated neurons in a song control nucleus of the adult canary forebrain,” *Journal of Comparative Neurology*, **240**(2), pp. 143–152.
- [39] ALVAREZ-BUYLLA, A., F. NOTTEBOHM, ET AL. (1990) “Birth of projection neurons in adult avian brain may be related to perceptual or motor learning,” *Science*, **249**(4975), pp. 1444–1446.
- [40] WANG, Y. and Z.-H. QIN (2010) “Molecular and cellular mechanisms of excitotoxic neuronal death,” *Apoptosis*, **15**(11), pp. 1382–1402.
- [41] SUBERBIELLE, E., P. E. SANCHEZ, A. V. KRAVITZ, X. WANG, K. HO, K. EILERTSON, N. DEVIDZE, A. C. KREITZER, and L. MUCKE (2013) “Physiologic brain activity causes DNA double-strand breaks in neurons, with exacerbation by amyloid- $\beta$ ,” *Nature neuroscience*, **16**(5), p. 613.
- [42] THOMPSON, C. K., J. MEITZEN, K. REPLOGLE, J. DRNEVICH, K. L. LENT, A. M. WISSMAN, F. M. FARIN, T. K. BAMMLER, R. P. BEYER, D. F. CLAYTON, ET AL. (2012) “Seasonal changes in patterns of gene expression in avian song control brain regions,” *PloS one*, **7**(4), p. e35119.
- [43] ALVAREZ-BORDA, B. and F. NOTTEBOHM (2002) “Gonads and singing play separate, additive roles in new neuron recruitment in adult canary brain,” *Journal of Neuroscience*, **22**(19), pp. 8684–8690.
- [44] VELLEMA, M., A. VAN DER LINDEN, and M. GAHR (2010) “Area-specific migration and recruitment of new neurons in the adult songbird brain,” *Journal of Comparative Neurology*, **518**(9), pp. 1442–1459.
- [45] ALVAREZ-BUYLLA, A. and F. NOTTEBOHM (1988) “Migration of young neurons in adult avian brain,” *Nature*, **335**(6188), p. 353.
- [46] BARAMI, K., B. KIRSCHENBAUM, V. LEMMON, and S. A. GOLDMAN (1994) “N-cadherin and Ng-CAM/8D9 are involved serially in the migration of newly generated neurons into the adult songbird brain,” *Neuron*, **13**(3), pp. 567–582.
- [47] SCOTT, B. B., T. GARDNER, N. JI, M. S. FEE, and C. LOIS (2012) “Wandering neuronal migration in the postnatal vertebrate forebrain,” *Journal of Neuroscience*, **32**(4), pp. 1436–1446.
- [48] KIRN, J. R., Y. FISHMAN, K. SASPORTAS, A. ALVAREZ-BUYLLA, and F. NOTTEBOHM (1999) “Fate of new neurons in adult canary high vocal center during the

- first 30 days after their formation,” *Journal of Comparative Neurology*, **411**(3), pp. 487–494.
- [49] HAHNLOSER, R. H., A. A. KOZHEVNIKOV, and M. S. FEE (2002) “An ultra-sparse code underlies the generation of neural sequences in a songbird,” *Nature*, **419**(6902), p. 65.
- [50] KORNFELD, J., S. E. BENEZRA, R. T. NARAYANAN, F. SVARA, R. EGGER, M. OBERLAENDER, W. DENK, and M. A. LONG (2017) “EM connectomics reveals axonal target variation in a sequence-generating network,” *Elife*, **6**, p. e24364.
- [51] MOONEY, R. and J. F. PRATHER (2005) “The HVC microcircuit: the synaptic basis for interactions between song motor and vocal plasticity pathways,” *Journal of Neuroscience*, **25**(8), pp. 1952–1964.
- [52] SCHARFF, C., J. R. KIRN, M. GROSSMAN, J. D. MACKLIS, and F. NOTTEBOHM (2000) “Targeted neuronal death affects neuronal replacement and vocal behavior in adult songbirds,” *Neuron*, **25**(2), pp. 481–492.
- [53] ALBERT, C. Y. and D. MARGOLIASH (1996) “Temporal hierarchical control of singing in birds,” *Science*, **273**(5283), pp. 1871–1875.
- [54] LEONARDO, A. and M. S. FEE (2005) “Ensemble coding of vocal control in birdsong,” *Journal of Neuroscience*, **25**(3), pp. 652–661.
- [55] CHI, Z. and D. MARGOLIASH (2001) “Temporal precision and temporal drift in brain and behavior of zebra finch song,” *Neuron*, **32**(5), pp. 899–910.
- [56] VAN VREESWIJK, C. and H. SOMPOLINSKY (1996) “Chaos in neuronal networks with balanced excitatory and inhibitory activity,” *Science*, **274**(5293), pp. 1724–1726.
- [57] VREESWIJK, C. v. and H. SOMPOLINSKY (1998) “Chaotic balanced state in a model of cortical circuits,” *Neural computation*, **10**(6), pp. 1321–1371.
- [58] BRUNEL, N. (2000) “Dynamics of sparsely connected networks of excitatory and inhibitory spiking neurons,” *Journal of computational neuroscience*, **8**(3), pp. 183–208.
- [59] LAJE, R. and D. V. BUONOMANO (2013) “Robust timing and motor patterns by taming chaos in recurrent neural networks,” *Nature neuroscience*, **16**(7), p. 925.
- [60] RAJAN, K., C. D. HARVEY, and D. W. TANK (2016) “Recurrent network models of sequence generation and memory,” *Neuron*, **90**(1), pp. 128–142.
- [61] DEPASQUALE, B., C. J. CUEVA, K. RAJAN, L. ABBOTT, ET AL. (2018) “full-FORCE: A target-based method for training recurrent networks,” *PloS one*, **13**(2), p. e0191527.

- [62] HARDY, N. F. and D. V. BUONOMANO (2018) “Encoding time in feedforward trajectories of a recurrent neural network model,” *Neural computation*, **30**(2), pp. 378–396.
- [63] GOLDMAN, M. S. (2009) “Memory without feedback in a neural network,” *Neuron*, **61**(4), pp. 621–634.
- [64] JIN, D. Z. (2002) “Fast convergence of spike sequences to periodic patterns in recurrent networks,” *Physical review letters*, **89**(20), p. 208102.
- [65] VALLENTIN, D. and M. A. LONG (2015) “Motor origin of precise synaptic inputs onto forebrain neurons driving a skilled behavior,” *Journal of Neuroscience*, **35**(1), pp. 299–307.
- [66] LONG, M. A., D. Z. JIN, and M. S. FEE (2010) “Support for a synaptic chain model of neuronal sequence generation,” *Nature*, **468**(7322), p. 394.
- [67] ABELES, M. (1982), “Local cortical circuits: Studies of brain function,” .
- [68] ——— (1991) *Corticonics: Neural circuits of the cerebral cortex*, Cambridge University Press.
- [69] DIEMANN, M., M.-O. GEWALTIG, and A. AERTSEN (1999) “Stable propagation of synchronous spiking in cortical neural networks,” *Nature*, **402**(6761), p. 529.
- [70] JIN, D. Z. (2009) “Generating variable birdsong syllable sequences with branching chain networks in avian premotor nucleus HVC,” *Physical Review E*, **80**(5), p. 051902.
- [71] BIENENSTOCK, E. (1995) “A model of neocortex,” *Network: Computation in neural systems*, **6**(2), pp. 179–224.
- [72] IZHIKEVICH, E. M., J. A. GALLY, and G. M. EDELMAN (2004) “Spike-timing dynamics of neuronal groups,” *Cerebral cortex*, **14**(8), pp. 933–944.
- [73] IZHIKEVICH, E. M. (2006) “Polychronization: computation with spikes,” *Neural computation*, **18**(2), pp. 245–282.
- [74] MCCULLOCH, W. S. and W. PITTS (1943) “A logical calculus of the ideas immanent in nervous activity,” *The bulletin of mathematical biophysics*, **5**(4), pp. 115–133.
- [75] KNIGHT, B. W. (1972) “Dynamics of encoding in a population of neurons,” *The Journal of general physiology*, **59**(6), pp. 734–766.
- [76] KURAMOTO, Y. (1975) “Self-entrainment of a population of coupled non-linear oscillators,” in *International symposium on mathematical problems in theoretical physics*, Springer, pp. 420–422.

- [77] IZHIKEVICH, E. M. (2003) “Simple model of spiking neurons,” *IEEE Transactions on neural networks*, **14**(6), pp. 1569–1572.
- [78] HODGKIN, A. L. and A. F. HUXLEY (1952) “A quantitative description of membrane current and its application to conduction and excitation in nerve,” *The Journal of physiology*, **117**(4), pp. 500–544.
- [79] DUTAR, P., H. M. VU, and D. J. PERKEL (1998) “Multiple cell types distinguished by physiological, pharmacological, and anatomic properties in nucleus HVC of the adult zebra finch,” *Journal of Neurophysiology*, **80**(4), pp. 1828–1838.
- [80] KUBOTA, M. and I. TANIGUCHI (1998) “Electrophysiological characteristics of classes of neuron in the HVC of the zebra finch,” *Journal of neurophysiology*, **80**(2), pp. 914–923.
- [81] MOONEY, R. (2000) “Different subthreshold mechanisms underlie song selectivity in identified HVC neurons of the zebra finch,” *Journal of Neuroscience*, **20**(14), pp. 5420–5436.
- [82] ROTH, G. and U. DICKE (2005) “Evolution of the brain and intelligence,” *Trends in cognitive sciences*, **9**(5), pp. 250–257.
- [83] MANWANI, A. and C. KOCH (1999) “Detecting and estimating signals in noisy cable structures, I: Neuronal noise sources,” *Neural computation*, **11**(8), pp. 1797–1829.
- [84] BUTCHER, J. C. (2016) *Numerical methods for ordinary differential equations*, John Wiley & Sons.
- [85] DEBRABANT, K. (2010) “Runge-Kutta methods for third order weak approximation of SDEs with multidimensional additive noise,” *BIT Numerical Mathematics*, **50**(3), pp. 541–558.
- [86] PICARDO, M. A., J. MEREL, K. A. KATLOWITZ, D. VALLENTIN, D. E. OKOBI, S. E. BENEZRA, R. C. CLARY, E. A. PNEVMATIKAKIS, L. PANINSKI, and M. A. LONG (2016) “Population-level representation of a temporal sequence underlying song production in the zebra finch,” *Neuron*, **90**(4), pp. 866–876.
- [87] EGGER, R., Y. TUPIKOV, K. A. KATLOWITZ, S. E. BENEZRA, M. A. PICARDO, F. MOLL, J. KORNFELD, D. Z. JIN, and M. A. LONG “Local axonal conduction delays underlie precise timing of a neural sequence,” Unpublished.
- [88] SCOTTO-LOMASSESE, S., C. ROCHEFORT, A. NSHDEJAN, and C. SCHARFF (2007) “HVC interneurons are not renewed in adult male zebra finches,” *European Journal of Neuroscience*, **25**(6), pp. 1663–1668.

- [89] BENEZRA, S. E., R. T. NARAYANAN, R. EGGER, M. OBERLAENDER, and M. A. LONG (2018) “Morphological characterization of HVC projection neurons in the zebra finch (*Taeniopygia guttata*),” *Journal of Comparative Neurology*, **526**(10), pp. 1673–1689.
- [90] KOSCHE, G., D. VALLENTIN, and M. A. LONG (2015) “Interplay of inhibition and excitation shapes a premotor neural sequence,” *Journal of Neuroscience*, **35**(3), pp. 1217–1227.
- [91] DEUCHARS, J., D. C. WEST, and A. M. THOMSON (1994) “Relationships between morphology and physiology of pyramid-pyramid single axon connections in rat neocortex in vitro.” *The Journal of physiology*, **478**(3), pp. 423–435.
- [92] MARKRAM, H., J. LÜBKE, M. FROTSCHER, A. ROTH, and B. SAKMANN (1997) “Physiology and anatomy of synaptic connections between thick tufted pyramidal neurones in the developing rat neocortex.” *The Journal of physiology*, **500**(2), pp. 409–440.
- [93] FELDMEYER, D., V. EGGER, J. LÜBKE, and B. SAKMANN (1999) “Reliable synaptic connections between pairs of excitatory layer 4 neurones within a single ‘barrel’ of developing rat somatosensory cortex,” *The Journal of physiology*, **521**(1), pp. 169–190.
- [94] GAL, E., M. LONDON, A. GLOBERSON, S. RAMASWAMY, M. W. REIMANN, E. MULLER, H. MARKRAM, and I. SEGEV (2017) “Rich cell-type-specific network topology in neocortical microcircuitry,” *Nature neuroscience*, **20**(7), p. 1004.
- [95] DANISH, H. H., D. ARONOV, and M. S. FEE (2017) “Rhythmic syllable-related activity in a songbird motor thalamic nucleus necessary for learned vocalizations,” *PloS one*, **12**(6), p. e0169568.
- [96] BAYER, S. A., J. ALTMAN, ET AL. (1991) *Neocortical development*, vol. 1, Raven Press New York.
- [97] SHEN, Q., Y. WANG, J. T. DIMOS, C. A. FASANO, T. N. PHOENIX, I. R. LEMISCHKA, N. B. IVANOVA, S. STIFANI, E. E. MORRISEY, and S. TEMPLE (2006) “The timing of cortical neurogenesis is encoded within lineages of individual progenitor cells,” *Nature neuroscience*, **9**(6), p. 743.
- [98] DEGUCHI, Y., F. DONATO, I. GALIMBERTI, E. CABUY, and P. CARONI (2011) “Temporally matched subpopulations of selectively interconnected principal neurons in the hippocampus,” *Nature neuroscience*, **14**(4), p. 495.
- [99] HIRATA, T. and L. IWAI (2018) “Timing matters: A strategy for neurons to make diverse connections,” *Neuroscience research*.

- [100] JUN, J. K. and D. Z. JIN (2007) “Development of neural circuitry for precise temporal sequences through spontaneous activity, axon remodeling, and synaptic plasticity,” *PloS one*, **2**(8), p. e723.
- [101] MILLER, A. and D. Z. JIN (2013) “Potentiation decay of synapses and length distributions of synfire chains self-organized in recurrent neural networks,” *Physical Review E*, **88**(6), p. 062716.
- [102] OKUBO, T. S., E. L. MACKEVICIUS, H. L. PAYNE, G. F. LYNCH, and M. S. FEE (2015) “Growth and splitting of neural sequences in songbird vocal development,” *Nature*, **528**(7582), p. 352.
- [103] WILBRECHT, L. and J. R. KIRN (2004) “Neuron addition and loss in the song system: regulation and function,” *Annals of the New York Academy of Sciences*, **1016**(1), pp. 659–683.
- [104] OKUBO, T. S., E. L. MACKEVICIUS, H. L. PAYNE, G. F. LYNCH, and M. S. FEE ((2016)), “Single-unit extracellular recordings of projection neurons in the premotor cortical area HVC of juvenile male zebra finches during singing,” CRCNS.org, <http://dx.doi.org/10.6080/K01N7Z2Z>.
- [105] GIBB, L., T. Q. GENTNER, and H. D. ABARBANEL (2009) “Inhibition and recurrent excitation in a computational model of sparse bursting in song nucleus HVC,” *Journal of neurophysiology*, **102**(3), pp. 1748–1762.
- [106] GONZÁLEZ, Á. (2010) “Measurement of areas on a sphere using Fibonacci and latitude–longitude lattices,” *Mathematical Geosciences*, **42**(1), p. 49.
- [107] JIN, D. Z., F. M. RAMAZANOĞLU, and H. S. SEUNG (2007) “Intrinsic bursting enhances the robustness of a neural network model of sequence generation by avian brain area HVC,” *Journal of computational neuroscience*, **23**(3), p. 283.
- [108] PIATTI, V. C., M. G. DAVIES-SALA, M. S. ESPÓSITO, L. A. MONGIAT, M. F. TRINCHERO, and A. F. SCHINDER (2011) “The timing for neuronal maturation in the adult hippocampus is modulated by local network activity,” *Journal of Neuroscience*, **31**(21), pp. 7715–7728.
- [109] CAPORALE, N. and Y. DAN (2008) “Spike timing–dependent plasticity: a Hebbian learning rule,” *Annu. Rev. Neurosci.*, **31**, pp. 25–46.
- [110] FROEMKE, R. C. and Y. DAN (2002) “Spike-timing-dependent synaptic modification induced by natural spike trains,” *Nature*, **416**(6879), p. 433.
- [111] BABADI, B. and L. F. ABBOTT (2010) “Intrinsic stability of temporally shifted spike-timing dependent plasticity,” *PLoS computational biology*, **6**(11), p. e1000961.

- [112] KERCHNER, G. A. and R. A. NICOLL (2008) “Silent synapses and the emergence of a postsynaptic mechanism for LTP,” *Nature Reviews Neuroscience*, **9**(11), p. 813.
- [113] BATAGELJ, V. and A. MRVAR (2004) “Pajek—analysis and visualization of large networks,” in *Graph drawing software*, Springer, pp. 77–103.

# Vita

## Yevhen Tupikov

### Education

<b>Ph.D. in Physics</b> The Pennsylvania State University, University Park, PA	2014 - 2019
<b>M.S. in Physics</b> Moscow Institute of Physics and Technology, Moscow, Russia	2012 - 2014
<b>B.S. in Physics</b> Moscow Institute of Physics and Technology, Moscow, Russia	2008 - 2012

### Awards

**The Pennsylvania State University, University Park, PA**

Verne M. Willaman Distinguished Graduate Fellowship  
David H. Rank Memorial Physics Award  
W. Donald Miller Graduate Fellowship  
David C. Duncan Graduate Fellowship

### Publications

L. Jing, **Y. Tupikov**, K. Watanabe, T. Taniguchi, and J. Zhu, Effective Landau Level Diagram of Bilayer Graphene, Physical review letters 120, no. 4 (2018): 047701.

A. Yu. Kuntsevich, **Y. V. Tupikov**, V. M. Pudalov, and I. S. Burmistrov, Strongly correlated two- dimensional plasma explored from entropy measurements, Nat. Commun. 6, 7298 (2015)

**Y. Tupikov**, A.Y. Kuntsevich, V.M. Pudalov. et al., Temperature derivative of the chemical potential and its magneto-oscillations in a two-dimensional system, Jetp Lett. (2015) 101: 125